ISSN: 2161-4717 Volume 9, Number 1, March 2019

Scientific Research Publishing

International Journal of Astronomy and Astrophysics

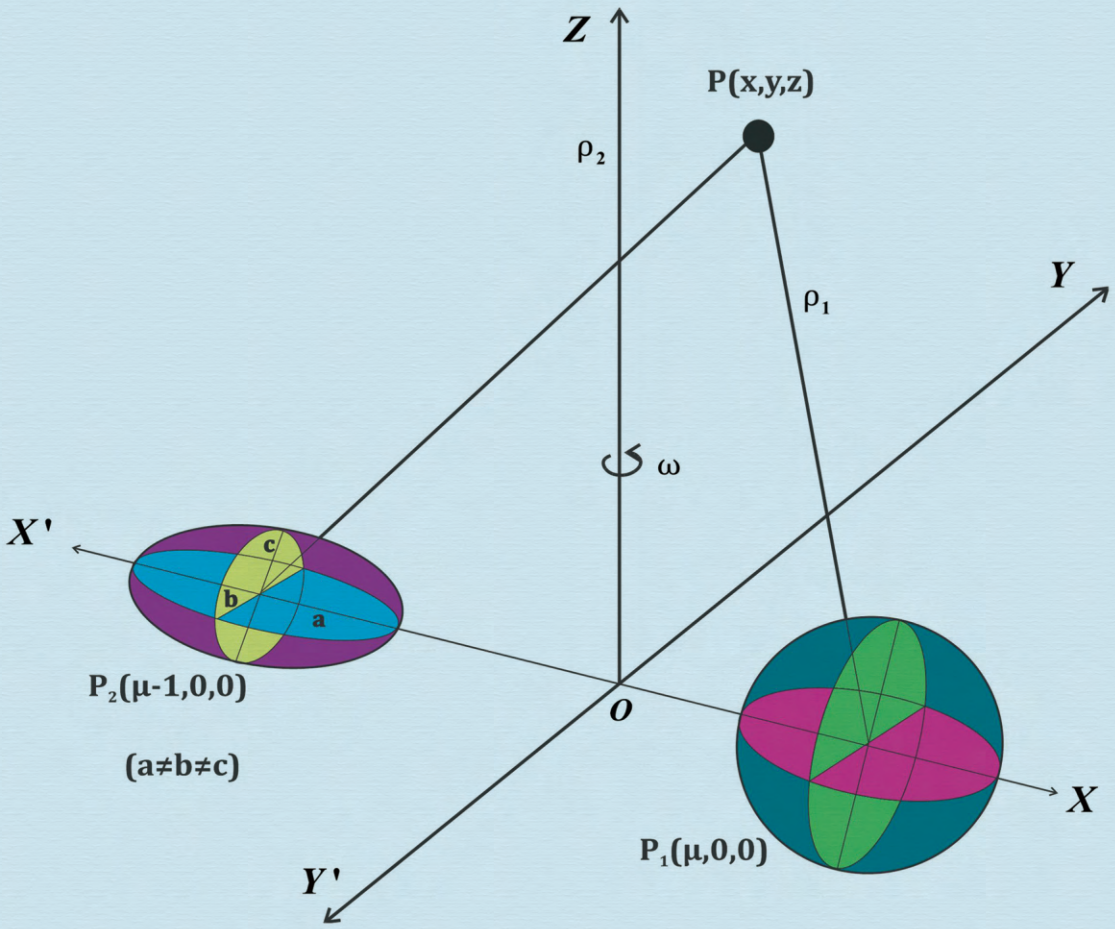

ISSN: 2161-4717

www.scirp.org/journal/ijaa

Journal Editorial Board

ISSN 2161-4717 (Print) ISSN 2161-4725 (Online)
http://www.scirp.org/journal/ijaa

Editor-in-Chief

Editorial Board

Scientific Research Publishing

International Journal of Astronomy and Astrophysics, 2019, 9, 1-70
http://www.scirp.org/journal/ijaa
ISSN Online: 2161-4725
ISSN Print: 2161-4717

Table of Contents

Volume 9 Number 1 March 2019

The figure on the front cover is from the article published in International Journal of Astronomy and Astrophysics, 2019, Vol. 9, No. 1, pp. 21-38 by M. R. Hassan, Sweta Kumari, R. R. Thapa, and Md. Aminul Hassan.

International Journal of Astronomy and Astrophysics (IJAA)
Journal Information

SUBSCRIPTIONS

The *International Journal of Astronomy and Astrophysics* (Online at Scientific Research Publishing, www.SciRP.org) is published quarterly by Scientific Research Publishing, Inc., USA.

Subscription rates:
Print: $79 per issue.
To subscribe, please contact Journals Subscriptions Department, E-mail: sub@scirp.org

SERVICES

Advertisements
Advertisement Sales Department, E-mail: service@scirp.org

Reprints (minimum quantity 100 copies)
Reprints Co-ordinator, Scientific Research Publishing, Inc., USA.
E-mail: sub@scirp.org

COPYRIGHT

PRODUCTION INFORMATION

For manuscripts that have been accepted for publication, please contact:
E-mail: ijaa@scirp.org

International Journal of Astronomy and Astrophysics, 2019, 9, 1-11
http://www.scirp.org/journal/ijaa
ISSN Online: 2161-4725
ISSN Print: 2161-4717

Extended Hubble Diagram on the Basis of Gamma Ray Bursts Including the High Redshift Range of z = 0.0331 - 8.1

Laszlo A. Marosi

Ludwigshafen am Rhein, Germany
Email: LaszloMarosi@aol.com

How to cite this paper: Marosi, L.A. (2019) Extended Hubble Diagram on the Basis of Gamma Ray Bursts Including the High Redshift Range of z = 0.0331 - 8.1. *International Journal of Astronomy and Astrophysics*, **9**, 1-11.
https://doi.org/10.4236/ijaa.2019.91001

Received: November 17, 2018
Accepted: January 21, 2019
Published: January 24, 2019

Abstract

It is generally accepted that the history of the expansion of the universe can be exactly described by the concordance model, which makes specific predictions about the shape of the Hubble diagram. The redshift-magnitude Hubble diagram in the redshift range z = 0.0104 - 1 seems to confirm this expectation, and it is believed that this conformity is also valid in the high redshift range. However, this belief is not undisputed. Recent work in the high redshift range of up to z = 8.1 has shown that the shape of the Hubble diagram deviates considerably from the predictions made by the Lambda cold dark matter model. These analyses, however, were based on mixed SN1a and gamma ray burst data, and some astronomers argue that this may have biased the results. In this paper, 109 cosmology-independent, calibrated gamma ray burst z/μ data points are used to calculate the Hubble diagram in the range z = 0.034 to z = 8.1. The outcome of this analysis confirms prior results: contrary to expectations, the shape of the Hubble diagram turns out to be exponential, and this is difficult to explain within the framework of the standard model. The cosmological implications of this unexpected result are discussed.

Keywords

Redshift, Gamma Ray Bursts, Hubble Diagram, Exponential Slope, Hubble's Law, ΛCDM Model

1. Introduction

The basic premise of Big Bang cosmology is that the universe is expanding. Important evidence for this expansion is that it follows from general relativity (GR) [1], which has been successfully tested both in the solar system and on the cosmic scale.

Besides GR, the Hubble constant (H_0) [2] is probably the most fundamental cosmological parameter. It is considered to be the most convincing evidence for universal expansion, and the universe expands with a velocity determined by the Hubble constant.

At the same time, however, we have to keep in mind that neither GR nor Hubble's constant is a real proof for expansion. GR when applied to the universe as a whole represents only a theoretical framework and allows the construction of numerous basically different cosmological models such as Einstein's static universe [1], the Einstein-deSitter model [3] and the dynamic, expanding or contracting, universe of Friedmann [4], for example. All these models are mathematically correct and none of them is preferred by GR. The presently prevailing inflationary ΛCDM model seems to confirm expansion and provides an excellent fit to most cosmological observations. However the price is high. The model rests on a large number of hypotheses, dark matter, dark energy, inflation, for example, which can either not be proved experimentally, or though theoretically provable, could not be proven, yet. Recently, a number of papers appeared in peer reviewed journals proposing new models without DM or DE or both [5] [6] [7] and without inflation [8].

And even the interpretation of Hubble's constant as recession velocity is hypothetical. Hubble never measured velocity; the expansion of the universe cannot be measured experimentally. The Hubble Law is a RS/distance relation, and the Hubble recession law is in reality a working hypothesis.

The question must be asked: how sure can we be that the universe really expands with velocity of the Hubble constant? Different tests based on observational data have been proposed to provide evidence for the expansion hypothesis. A critical review of these tests shows that convincing evidence for the universal expansion is still lacking [9] [10]. The static universe model fits the observational data better than expansion models [10] [11] [12].

A promising tool to confirm expansion is the Hubble diagram test. We expect that in the high RS range it should be possible to check more precisely whether the Hubble diagram follows the linear H_0D/c (expanding models) or the exponential $z+1=e^{H_0*t}$ (tired light) relation, an effect that is perceptible only slightly in the $z < 1$ region. The Hubble diagram (HD), calculated on the basis of a SN1a supernovae redshift (RS, z)/magnitude (μ) data, gives an excellent fit to the predictions of the concordance model [13] [14] [15]. However, a hint of uncertainty remains. The fit of the Lambda cold dark matter model (ΛCDM) to the SN1a z/μ data applies only within the narrow range of $z = 0$ - 1. One reason for this is experimental difficulties; at RSs > ~1.3, the optical light emitted by supernovae becomes increasingly dimmed with distance, probably due to gray dust extinction, and accurate observations become difficult. However, cosmologists are not concerned with this RS limitation and consider the RS range of $z >$ ~1 - 8 to be uninteresting. At higher RSs, the universe is matter-dominated, and the lambda term in the high RS region does not affect the universal expansion. It is

assumed that the HD at high RS would merely confirm the concordance cosmology [16]. In recent years, a number of papers appearing in peer-reviewed journals have drawn the conclusion that the shape of the HD is exponential over the entire RS range of 0.0104 - 8.1, in clear contrast to the specific predictions of the ΛCDM model [17] [18] [19]. These analyses were performed with mixed SN1a und gamma ray burst (GRB) data, and some astronomers argue that this may have biased the results.

The best way to confirm or disprove the exponential shape of the HD is to use exclusively GRB data to calculate the HD over the whole RS range of $z = 0.034$ - 8.1. In previous papers, several attempts have been made to utilize GRB data to calculate the HD [16] [20] [21] [22] [23] with varying degrees of success. The limited number of data points and the large scatter of the data do not allow for safe conclusions. However, thanks to Swift (The Neil Gehrels Swift Observatory, NASA), the main features of GRBs have become better known in recent years. On the basis of more accurate observations of GRBs, the expectation has arisen that these objects could prove to be suitable distance indicators. Many hundreds of bursts have been observed in the range $0.034 < z \leq 8$, which opens up the possibility of measuring the expansion history back to the formation of the first stars. It is expected that the maximum clearly observable RS could approach 10 or even larger. This could place significant constraints on the different models of universal expansion.

The aim of the present work is to perform an improved HD test based on a larger number of calibrated GRB RS/μ data points. The reliability of these data was verified using statistical tests before the analysis was carried out.

2. Experimental

A total of 109 calibrated, cosmology independent GRB z/μ data points collected by Wei [24] from the 557 Union2 compilations were used as the starting data set. From these 109 data points, three low RS data points 050416A ($\mu = 41.44 \pm 1.2$), 080319B ($\mu = 43.07 \pm 1.24$), 061121 ($\mu = 46.18 \pm 1.01$), ($\overline{\mu} = \pm 0.41$; average error in μ for 50 low RS GRB data points) and three high RS data points 040912 ($\mu = 43.27 \pm 2.06$), 09120 ($\mu = 47.58 \pm 1.96$), and 080913 ($\mu = 50.45 \pm 1.74$), ($\overline{\mu} = \pm 1.55$; average error in μ for 59 high RS GRB data points) were excluded from the following refinement process due to their unusually large error bars, which indicate observational difficulties in terms of magnitude determination.

For the remaining 103 data points, best fit curves were calculated, which are more accurate than those used in any previous work, using the empirical potential function

$$\mu = a * z^b, \tag{1}$$

with $a = 44.1097$ and $b = 0.05988$, which was determined in earlier publications for SN1a gold set and for GRB data to be the best mathematical approximation for describing the slope of the z/μ diagram [25] [26] [27].

2.1. Elimination of Outliers

In view of the experimental difficulties in determining the z/μ data, it is likely that large data sets taken from different observations and from different sources will contain outliers. If these outliers are not removed from the refinement procedure, they will dominate the fit and bias the results.

2.2. Identification of Outliers: The Grubbs Test

The well-known Grubbs test [28] was used for the identification of erroneous luminosity indicators. The Grubbs test is used to detect outliers in a data set of N values that are nearly normally distributed. Assuming a normal distribution of the sample, as confirmed by the very low skew in Table 1, the test is performed by computing x_0, which is defined as:

$$X_0 \geq \frac{G_G * \mathrm{STABW} + x_{\mathrm{Mean}}}{\sqrt{\frac{N}{N-1}}} \tag{2}$$

where:

x_0 is the suspected outlier;

x_{Mean} is the absolute value of the mean of the N data points;

N is the number of data points;

STABW is the standard deviation of N values; and

G_G is the Grubbs number. G_G can be found in statistical tables for different levels of confidence and numbers of data points. For 103 data points, for example, G is 1.956 at 95% confidence level.

If the x_0 calculated from (μ_{measured} - $\mu_{\mathrm{calculated}}$) is found to be greater than the numerical value of the right-hand side of Equation (1), the data point in question must be discarded; on the basis of the reduced data set, new a and b coefficients, the mean and the new STABW must be calculated, and so on.

2.3. Preparation of the Hubble Diagram

The Hubble diagram is a linear plot of the measured distance (usually Mpc) versus the measured RS, which is often represented on the less sensitive logarithmic μ/RS scale.

Since the differences between the measured and the calculated trend lines become more pronounced on the linear scale, a plot of the photon flight time (t) versus RS was used for representation of the HD. The photon flight time was calculated from

$$t = \frac{D}{c} = \frac{10^{(\mu+5)/5}}{(z+1)*3*10^{10}} * 3.085 * 10^{18} \tag{3}$$

Table 1. Fit results from the starting data set. Descriptive statistics z/μ.

Raw data	Valid cases	a	b	R^2	STABW μ_{obs} - μ_{calc}	Skew μ_{obs} - μ_{calc}
109	103	44.049	0.0595	0.9066	0.7384	0.4221

In Equation (2), t represents the flight time of the photons (in sec) from the co-moving radial distance D to the observer, which is proportional to D (Mpc) as used in the Hubble law.

2.4. Hubble Diagram Representation

The Hubble diagram as originally presented by Hubble [2] is a distance (Mpc)/velocity (v) representation where $v = cz$. Recently it becomes increasingly common to use the logarithmic z/μ diagram as presented in **Figure 1** and **Figure 2** instead of the linear distance/redshift scale.

The presentation $t/(z + 1)$ as used in this paper is essentially equivalent to Hubble's depiction, with Mpc $= t \times c$ (abscissa) and $z = v/c$ (ordinate) and the two diagrams differ only in the scale of the axes. The advantage of the $t/(z + 1)$ representation is, as can be seen in **Figure 3** and **Figure 4**, is that the slope of the best fit line can be fitted exactly with the exponential function $z+1=e^{H_0*t}$.

2.5. Luminosity Distances

Luminosity distances were calculated using the cosmological calculator described by Wright [29].

2.6. Excel and Excel Solver

Excel and Excel Solver were used for the data fitting, refinement, analysis and data presentation.

3. Results

The results of the fit procedure based on 103 raw data points are shown in **Figure 1** and **Table 1**.

As can be seen from **Figure 1**, the data are affected by considerable scatter, resulting in large variability of the data and a relatively poor goodness of fit indicator of $R^2 = 0.9066$.

A representative result of the iterative refinement process is shown in **Figure 2** and **Figure 3**. The corresponding descriptive statistics are summarized in **Tables 2-7**.

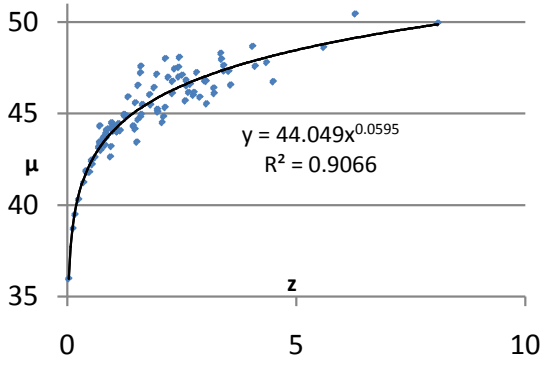

Figure 1. Best fit curve for the initial 103 GRB data points.

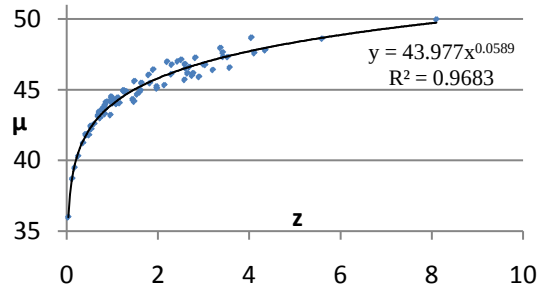

Figure 2. Best fit curve based on 84 statistically verified GRB z/μ data points.

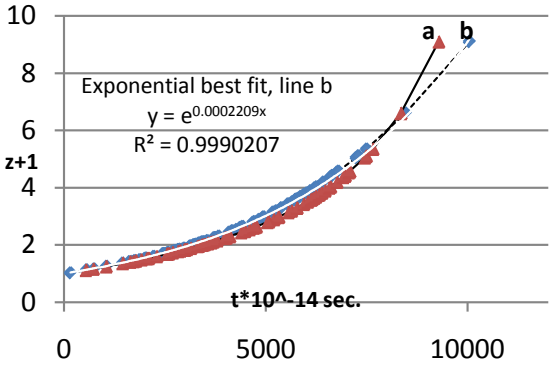

Figure 3. Representative Hubble diagram based on 84 statistically verified GRB z/μ data points.

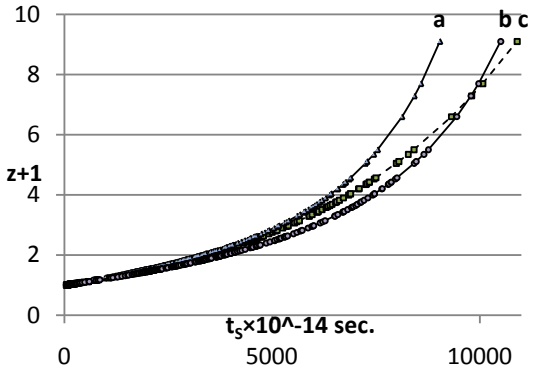

Figure 4. Redshift of type I a supernovae as a function of $t = D_C/c$. Squares (dashed line): t/z data inferred from the potential best-fit curve of the observed z/μ diagram. Triangles: t/z relationship derived from the ΛCDM model with $H_0 = 72.6$ km·s^{-1}·Mpc^{-1}, Circles: t/z relationship derived from the ΛCDM model with $H_0 = 62.5$ km·s^{-1}·Mpc^{-1} (data are taken from [26]).

Table 2. Results of regression with $\mu = a \times z^b$. Descriptive statistics z/μ; one iteration.

Valid cases	a	b	R^2	Variance (μ_{obs} - μ_{calc})	$\Sigma\chi^2$ (μ_{obs} - μ_{calc})
90	43.999	0.0592	0.9557	0.2538	0.4920
Mean (μ_{obs} - μ_{calc})	**Std. Deviation** (μ_{obs} - μ_{calc})	**Error in Std. D.**	**Skew** (μ_{obs} - μ_{calc})	**F-Test** μ_{obs}/μ_{calc}	P
0.00073	0.5038	0.0531	0.0733	0.8281	1

Table 3. Results of regression. Descriptive statistics $t/z+1$; one iteration.

Valid cases	H_0		R^2	Variance (z_{obs} - z_{calc})	$\Sigma\chi^2$ (z_{obs} - z_{calc})
90	0.0002147 (2.147×10^{-18} s^{-1})		0.99942	0.0032 (z_{obs} - z_{calc})	0.099
Mean (z_{obs} - z_{calc})	**Std. Deviation** (z_{obs} - z_{calc})	**Error in Std. D.**	**Skew** (z_{obs} - z_{calc})	**F-Test** z_{obs}/z_{calc}	***P***
0.0374	0.0569	0.006	1.028	0.7575	1

Table 4. Results of regression with $\mu = a \times z^b$. Descriptive statistics z/μ; two iterations.

Valid cases	*a*	*b*	R^2	Variance (μ_{obs} - μ_{calc})	$\Sigma\chi^2$ (μ_{obs} - μ_{calc})
84	43.977	0.0589	0.9683	0.181	0.3287
Mean (μ_{obs} - μ_{calc})	**Std. Deviation** (μ_{obs} - μ_{calc})	**Error in Std. D.**	**Skew** (μ_{obs} - μ_{calc})	**F-Test** μ_{obs}/μ_{calc}	***P***
0.00158	0.4254	0.0464	−0.01075	0.8867	1

Table 5. Results of regression with $t/z+1$. Descriptive statistics; two iterations.

Valid cases	H_0		R^2	Variance (z_{obs} - z_{calc})	$\Sigma\chi^2$ (z_{obs} - z_{calc})
84	0.0002209 (2.209×10^{-18} s^{-1})		0.9990	0.0018	0.04279
Mean (z_{obs} - z_{calc})	**Std. Deviation** (z_{obs} - z_{calc})	**Error in Std. D.**	**Skew** (z_{obs} - z_{calc})	**F-Test** (z_{obs}:z_{calc})	***P***
0.00035	0.4255	0.0046	1.1519	0.8536	1

Table 6. Results of regression with $\mu = a \times z^b$. Descriptive statistics z/μ; three iteration.

Valid cases	*a*	*b*	R^2	Variance μ_{obs}:μ_{calc}	$\Sigma\chi^2$ μ_{obs}:μ_{calc}
80	43.976	0.0589	0.9732	0.1489	0.2593
Mean (μ_{obs} - μ_{calc})	**Std. Deviation** (μ_{obs} - μ_{calc})	**Error in Std. D.**	**Skew** (μ_{obs} - μ_{calc})	**F-Test** M_{obs}:μ_{calc}	***P***
0.001927	0.3859	0.0043	−0.174	0.9074	1

Table 7. Results of regression with $t/z+1$. Descriptive statistics; three iteration.

Valid cases	H		R^2	Variance (z_{obs} - z_{calc})	$\Sigma\chi^2$ (z_{obs} - z_{calc})
80	0.0002208 ($2.208 \times 10^{-18} s^{-1}$)		0.999	0.00176	0.03997
Mean (z_{obs} - z_{calc})	**Std. Dviation** (z_{obs} - z_{calc})	**Error in Std. D.**	**Skew** (z_{obs} - z_{calc})	**F-Test** z_{obs}:z_{calc}	***P***
0.0007	0.042	0.0047	1.449	0.8549	1

(a) HD calculated on the basis of the currently most accurate LJA z/μ data with best fit parameters H_0 = 70 km·s^{-1}·Mpc^{-1}, Ω_m = 0.295, w = −1.104 [25]; (b)

measured best fit line. The results of the two iteration steps are shown in Table 5:

As can be seen from Figure 3, the shape of the HD is exponential or (more critically) very close to exponential, whilst the ΛCDM model shows systematic deviations from the exponential best fit curve ($\Sigma\chi^2$ best fit, line $b = 0.04279$; $\Sigma\chi^2$ ΛCDM model, line $a = 0.3671$).

This result is in perfect agreement with earlier findings [18] that ΛCDM models show poor agreement with observation (Figure 4).

The HD diagram on basis of the ΛCDM model with $H_0 = 62.5$ km·s^{-1}·Mpc^{-1} (line b in Figure 3) deviates below the trendline of the best-fit curve for $z + 1 < 6.5$ to the bottom, and above it for $z + 1 > 6.3$. These deviations are of a non-statistical nature and thus the model does not reflect the observed exponential slope.

For $H_0 = 72.6$ km·s^{-1}·Mpc^{-1} (line a in Figure 4) the ΛCDM model departs considerably from the observed exponential function (line c), and in the range $z > \sim 2$, a sharp increase is shown in the slope. A $\Sigma\chi^2$ test shows a statistical significance between the observed t/μ and the calculated ΛCDM data of $P = 0.053$, and fails to describe the observed z/μ data completely.

Tables 2-7 show that after only two iteration steps, the further removal of outliers does not result in a substantial improvement in terms of either shape or goodness of fit indicators.

4. Discussion

The results presented here show that the Hubble diagram $t/(z + 1)$ calculated on the basis of GRB z/μ data follows a strictly exponential slope in the range $0.0331 < z < 8.1$, in excellent agreement with observation. The exponential slope of the Hubble diagram provides a clear indication of an energy decrease in the emitted spectral lines with a constant rate. At RSs > ~2, the ΛCDM model does not fit the data well (dashed line in Figure 3). This unexpected result leads to a logical contradiction between theory and observation, which cannot be solved within the frame of the concordance model. We consider it certain that the universe (spacetime) expands, and the expanding space causes a RS in the photons that is proportional to the extent of expansion. The shape of the HD should follow the explicit predictions of the concordance model, which cannot be exponential.

The question arises of how to interpret these contradictory results in light of the expansion hypothesis. If we exclude the static universe model, the most radical answer explaining this disagreement would be that something is wrong with the basic assumptions of the underlying cosmological model. The results presented here require that the HD is completely determined by an energy decay process that is as yet unknown, which most cosmologists are not ready to accept, since this would require the most important evidence for universal expansion to be discarded.

It is not the aim of this paper to identify a specific new energy decay mechan-

ism (although some promising alternatives have been proposed in the recent literature [26] [27] [30] [31] to explain these contradictory results); however, it should be pointed out that the disagreement between the predictions of the concordance model and the strictly exponential slope of the HD is a real problem that requires an explanation. In view of this, the HD test may prove to be the most important cross check in determining the expansion history of the universe and the physical meaning of H_0. Increasingly accurate high-RS GRB z/μ data may turn out to be the key to this important cosmological issue. There is hope this could be done in the near future.

"We are now at an interesting juncture in cosmology. With new methods and technology, the accuracy in measurement of the Hubble constant (from high RS GRB data) has vastly improved, but a recent tension has arisen that is signaling as-yet unrecognized uncertainties. The key pillar of the standard cosmological model becomes shaky" [32] [33].

Conflicts of Interest

The author declares no conflicts of interest regarding the publication of this paper.

References

[1] Einstein, A. (1917) Kosmologische Betrachtungen zur allgemeinen Relativitätstheorie, Sitzungsberichte der Königlich Preußischen Akademie der Wissenschaften (Berlin), S. 142-152. [Cosmological Observations about the General Theory of Relativity, Proceedings of the Royal Prussian Academy of Sciences, Vol. 142-152.]

[2] Hubble, E.P. (1929) A Relation between Distance and Radial Velocity among Extra-Galactic Nebulae. *Proceedings of the National Academy of Sciences of the United States of America*, **15**, 167-173. https://doi.org/10.1073/pnas.15.3.168

[3] Einstein, A. and deSitter, W. (1932) On the Relation between the Expansion and the Mean Density of the Universe. *Proceedings of the National Academy of Sciences of the United States of America*, **18**, 213-214. https://doi.org/10.1073/pnas.18.3.213

[4] Friedmann, A. (1922) Über die Krümmung des Raumes. *Zeitschrift für Physik*, **10**, 377-386. https://doi.org/10.1007/BF01332580

[5] Moffat, J.W. and Toth, V.T. (2012) Modified Gravity: Cosmology without Dark Matter or Einstein's Cosmological Constant. arXiv:0710.0364v7[astro-ph]

[6] Mitra, A. (2011) An Astrophysical Peek into Einstein's Static Universe, No Dark Energy. *International Journal of Astronomy and Astrophysics*, **1**, 183-199. https://doi.org/10.4236/ijaa.2011.14024

[7] Mitra, A. (2013) Energy of Einstein's Static Universe and Its Interpretation for the ΛCDM Cosmology. *International Journal of Cosmology and Astroparticle Physics*, No. 3, Article ID: 007.

[8] Mitra, A. (2014) Why the Big Bang Model Does Not Allow Inflationary and Cyclic Cosmologies though Mathematically One Can Obtain Any Model with Favorable Assumptions. *New Astronomy,* **30**, 46-50. https://doi.org/10.1016/j.newast.2013.12.002

[9] Lòpez-Correditora, M. (2017) Tests and Problems of the Standard Model in Cosmology. *Foundations of Physics*, **47**, 711-768.

https://doi.org/10.1007/s10701-017-0073-8

[10] Lerner, E.J. (2018) Observation Contradict Galaxy Size and Surface Brightness Predictions That Are Based on the Expanding Universe Hypothesis. *MNRAS*, **477**, 3185-3196. https://doi.org/10.1093/mnras/sty728

[11] Lòpez-Correddiora, M. (2018) Problems with the Dark Matter and Dark Energy Hypothesis, and Alternative Ideas. arXiv: 1808.09823

[12] Crawford, D.A. (2011) Observational Evidence Favors a Static Universe. *The Journal of Cosmology*, **13**, 3875-3946.

[13] Perlmutter, S., *et al.* (1999) Measurements of Ω and Λ from 42 High-Redshift Supernovae. *The Astrophysical Journal*, **517**, 565-586. https://doi.org/10.1086/307221

[14] Riess, A., *et al.* (1998) Observational Evidence from Supernovae for an Accelerating Universe and a Cosmological Constant. *Astronomical Journal*, **116**, 1009-1038. https://doi.org/10.1086/300499

[15] Schmidt, B.P., *et al.* (1994) The Expanding Photosphere Method Applied to SN 1992am AT CZ = 14600 km/s. *Astronomical Journal*, **107**, 1444-1452. https://doi.org/10.1086/116957

[16] Schäfer, B.E. (2006) The Hubble Diagram to Redshift > 6 from 69 Gamma-Ray Bursts. arXiv:astro-ph/0612285

[17] Marosi, L.A. (2013) Hubble Diagram Test of Expanding and Static Cosmological Models: The Case for a Slowly Expanding Universe. *Advances of Astronomy*, **2013**, Article ID: 917104. https://doi.org/10.1155/2013/917104

[18] Marosi, L.A. (2014) Hubble Diagram Test of 280 Supernovae Redshift Data. *Journal of Modern Physics*, **5**, 29-33. https://doi.org/10.4236/jmp.2014.51005

[19] Marosi, L.A. (2016) Modelling and Analysis of the Hubble Diagram of 280 Supernovae and Gamma Ray Bursts Redshifts with Analytical and Empirical Redshift/Magnitude Data. *International Journal of Astronomy and Astrophysics*, **6**, 272-275. https://doi.org/10.4236/ijaa.2016.63022

[20] Izzo, L., Capozziello, S., Covone, G. and Capaccioli, M. (2009) Extending the Hubble Diagram by Gamma Ray Bursts. *Astronomy and Astrophysics*, **508**, 63-67. https://doi.org/10.1051/0004-6361/200912769

[21] Demianski, M., Piedipalumbo, E. and Rubano, C. (2011) The Gamma-Ray Bursts Hubble Diagram in Quintessential Cosmological Models. *Monthly Notices of the Royal Astronomical Society*, **411**, 1213-1222. https://doi.org/10.1111/j.1365-2966.2010.17751.x

[22] Cardone, V.F., Capozziello, S. and Dainotti, M.G. (2009) An Updated Gamma Ray Bursts Hubble Diagram. arXiv: 0901.3194v2

[23] Liu, J. and Wei, H. (2015) Cosmological Models and Gamma-Ray Bursts Calibrated by Using Padé Method. *General Relativity and Gravitation*, **47**, 141. https://doi.org/10.1007/s10714-015-1986-1

[24] Wei, H. (2010) Observational Constraints on Cosmological Models with the Updated Long Gamma Ray Bursts. *Journal of Cosmology and Astroparticle Physics*, **2010**, 14. https://doi.org/10.1088/1475-7516/2010/08/020

[25] Betoule, M., *et al.* (2014) Improved Cosmological Constraints from a Joint Analysis of the SDSS-II and SNLS Supernova Samples. *Astronomy & Astrophysics*, **568**, Article No. A22. arXiv:1401.4064 https://doi.org/10.1051/0004-6361/201423413

[26] Marosi, L.A. (2017) Is the Velocity Interpretation of the Redshift of Spectral Lines in Accordance with Astronomical Data? *International Journal of Astronomy and*

Astrophysics, **7**, 248-254. https://doi.org/10.4236/ijaa.2017.74021

[27] Lineweaver, C.H. and Barbosa, B. (1998) Cosmic Microwave Background: Implications for Hubble Constant and the Spectral Parameters *n* and *Q* in Cold Dark Matter Critical Density Universes. *Astronomy & Astrophysics*, **329**, 799-808.

[28] Grubbs, E. (1950) Sample Criteria for Testing Outlying Observations. *The Annals of Mathematical Statistics*, **21**, 27-58. https://doi.org/10.1214/aoms/1177729885

[29] Wright, E.I. (2006) A Cosmology Calculator for the World Wide Web. *Publications of the Astronomical Society of the Pacific*, **118**, 1711-1715. https://doi.org/10.1086/510102

[30] Blanchard, A., Douspis, M., Rowan-Robinson, M. and Sarkar, S. (2003) An Alternative to the Cosmological "Concordance Model". *Astronomy & Astrophysics*, **412**, 35-44. https://doi.org/10.1051/0004-6361:20031425

[31] Marosi, L.A. (2017) Non Velocity Interpretation of the Cosmic Redshift—Cosmological Implications. http://gsjournal.net/Science-Journals/ResearchPapers-Cosmology/Download/6954

[32] Friedmann, W.L. (2017) Cosmology at a Crossroads: Tension with the Hubble Constant. *Nature Astronomy*, **1**, 0169. arXiv: 1706.02739

[33] Nielsen, J.T., Guffanti, A. and Sarkar, S. (2016) Marginal Evidence for Cosmic Acceleration from Type Ia Supernovae. *Scientific Reports*, **6**, Article No. 35596. https://doi.org/10.1038/srep35596

International Journal of Astronomy and Astrophysics, 2019, 9, 12-20
http://www.scirp.org/journal/ijaa
ISSN Online: 2161-4725
ISSN Print: 2161-4717

Early Solar System Solar Wind Implantation of ^{7}Be into Calcium-Alumimum Rich Inclusions in Primitive Meteortites

Glynn E. Bricker

Department of Physics, Purdue University Northwest, Westville, USA
Email: gbricker@pnw.edu

How to cite this paper: Bricker, G.E. (2019) Early Solar System Solar Wind Implantation of ^{7}Be into Calcium-Alumimum Rich Inclusions in Primitive Meteortites. *International Journal of Astronomy and Astrophysics*, **9**, 12-20.
https://doi.org/10.4236/ijaa.2019.91002

Received: November 27, 2018
Accepted: January 21, 2019
Published: January 24, 2019

Abstract

The one time presence of short-lived radionuclides (SLRs) in Calcium-Aluminum Rich inclusions (CAIs) in primitive meteorites has been detected. The solar wind implantation model (SWIM) is one possible model that attempts to explain the catalogue of SLRs found in primitive meteorites. In the SWIM, solar energetic particle (SEP) nuclear interactions with gas in the proto-solar atmosphere of young stellar objects (YSOs) give rise to daughter nuclei, including SLRs. These daughter nuclei then may become entrained in the solar wind via magnetic field lines. Subsequently, the nuclei, including SLRs, may be implanted into CAI precursors that have fallen from the main accretion flow which had been destined for the proto-star. This mode of implanting SLRs in the solar system is viable, and is exemplified by the impregnation of the lunar surface with solar wind particles, including SLRs. X-ray luminosities have been measured to be 100,000 times more energetic in YSOs, including T-Tauri stars, than present-day solar luminosities. The SWIM scales the production rate of SLRs to nascent SEP activity in T-Tauri stars. Here, we model the implantation of ^{7}Be into CAIs in the SWIM, utilizing the enhanced SEP fluxes and the rate of refractory mass inflowing at the X-region, 0.06 AU from the proto-Sun. Taking into account the radioactive decay of ^{7}Be and spectral flare variations, the ^{7}Be/^{9}Be initial isotopic ratio is found to range from 1×10^{-5} to 5×10^{-5}.

Keywords

Radio-Nuclide, ^{7}Be, Early Solar System, Solar Wind, CAI, Solar Wind Implantation Model, X-Wind

1. Introduction

Studies report evidence for the one-time presence of SLRs, through decay prod-

uct systematics, including ^{10}Be, ^{26}Al, ^{36}Cl, ^{41}Ca, and ^{53}Mn, in CAIs in primitive carbonaceous meteorites at the nascence of the solar system [1]. The possible origins of these SLRs are widely varied and include stellar sources (AGB Stars, Wolf-Rayet stars, nova, and super nova) and energetic particle interaction, from either SEPs, or galactic cosmic rays (GCRs). Bricker & Caffee [2] [3] proposed the solar wind implantation model (SWIM) for the incorporation of ^{10}Be and ^{36}Cl into CAIs early in primitive meteorites.

In the SWIM, the SLRs come into existence via SEP nuclear reactions in the proto-solar atmosphere of the young Sun, characterized by X-ray emissions orders of magnitude greater than main sequence stars. Studies of the Orion Nebulae indicate that pre-main sequence (PMS) stars exhibit X-ray luminosity, and hence SEP fluxes on the order of ~10^5 over contemporary SEP flux levels [4]. The irradiation produced SLRs are then trapped by magnetic field lines, and these solar wind SLRs eventually impregnate CAI precursors. This mode of production of SLRs, entrainment of SLRs in the solar wind, and implantation of SLR into solar system material is seen in the implantation of solar wind particles, e.g. ^{10}Be [5] [6] and ^{14}C [6] [7], on the Moon.

^{10}Be is produced via SEP spallation reactions, with oxygen serving as the chief target particle in the SWIM. Similar to ^{10}Be, ^{7}Be, half-life of 53 days [8], is also primarily produced through SEP nuclear reactions with oxygen as the primary target particle, and ^{7}Be has also recently been detected in stellar photospheres [9] In addition, the one-time presence of ^{7}Be has been measured in CAIs in primitive meteorites (through the study of Li, the decay product of ^{7}Be, systematics) [10] [11]. Owing to the 53 day half-life, local irradiation is the only possible operation pathway for ^{7}Be production. As such, the large difference in half-lives between ^{7}Be and ^{10}Be is of interest in terms of chronological processes associated with early solar system and CAI formation and evolution.

In this work, we consider the possible incorporation of ^{7}Be into CAIs in primitive carbonaceous meteorites in the SWIM. **Table 1** below characterizes beryllium isotopes found in CAIs.

2. Solar Wind Implantation Mode

2.1. Synopsis

In the SWIM, SLRs are produced in the solar nebula via SEP nuclear reactions on gaseous target material in the solar atmosphere ~4.6 Gyr, during the formation

Table 1. Beryllium isotopes found in CAIs.

Nuclide	Half-life	Initial Isotopic Ratio	Radionuclide (g^{-1})
^{7}Be	53 days [8]	1.2×10^{-3} [10] 6.1×10^{-3} [11]	1.0×10^{13} 5.3×10^{13}
^{10}Be	1.36×10^{6} yr [12]	9.5×10^{-4} [13]	6.4×10^{12}

Note: Radionuclide content in g^{-1} calculated from initial isotopic ratio and ^{9}Be content in ppb. The ^{9}Be content in CAIs is estimated 100 ppb [14] [15].

of the solar system. These newly produced nuclei are incorporated in the solar wind. The SLRs flow along magnetic field lines in the solar wind, and this particle flow intersects with materials which have fallen out of the main accretion flow, which was headed to hot-spots on the Sun. At the intersection of outflowing SLRs, and inflowing fallen CAI precursor material, the SLRs may become impregnated into the inflowing materials. The fundamental geometry for the implantation process described above and transportation of implanted CAIs to the asteroid zone can be gleaned from the X-wind model of Shu *et al.* [16] [17] [18]. **Figure 1** below illustrates of the basic magnetic field geometry, ^{7}Be production via SEP flaring activity, and subsequent implantation into CAI-precursor material from the main funnel flow onto the proto-Sun.

2.2. Refractory Mass Inflow Rate

The effective refractory mass inflow rate, *S*, *i.e.* the refractory mass that falls from the main funnel flow which was accreting onto the star at the X-region, is calculated from equation (1):

$$S = \dot{M}_D \cdot X_r \cdot F \tag{1}$$

where $\dot{M}_D$ is disk mass accretion rate, X_r is the cosmic mass fraction, and F is the fraction of material that enters the X-region from the main funnel flow [19]. For $\dot{M}_D$, we adopt 1×10^{-7} solar masses year^{-1}. Disk mass accretion rates range from ~10^{-7} to ~10^{-10} solar masses year^{-1} for T Tauri stars from 1 - 3 Myr [20], whereas embedded class 0 and class I PMS stars have mass accretion rates of ~10^{-5} to ~10^{-6} solar masses year^{-1} [21]. Here we adopt for $\dot{M}_D$, a rate 1×10^{-7} solar masses year^{-1}, corresponding to class II or III PMS stars. From Lee *et al.* [19] we utilize a cosmic mass fraction, X_r, and fraction of refractory material fraction F, of 4×10^{-3} and 0.01, respectively, in our model. X_r represents the fraction of refractory content in the inflowing material, and F represents the fraction of inflowing mass that does not accrete onto the proto-sun. The choice 0.01

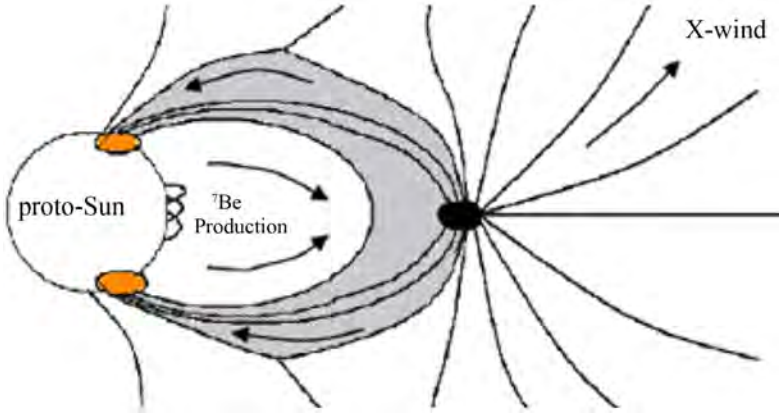

Figure 1. SWIM magnetic field geometry for SLRs production via SEP nuclear reactions. The gray area represents the main accretion flow onto "hot spots" on the PMS star. SLRs produced close to the proto-solar surface are incorporated into CAI precursor material which has fallen from the accretion flow (figure after Shu *et al.* [17]).

maximizes F, and corresponds to all the mass which comprises the planets falling from the accretion flow. $F = 0.01$ is the preferred value of Lee *et al.* [19] in their model. (See Lee *et al.* [19] for a detailed discussion of X_r and F) Employing Equation (1) and the parameters detailed above, we find the rate at which this refractory material reaches the x-region, called here the refractory mass inflow rate, S, is 2.5×10^{14} g s^{-1}. In consideration of the extreme values of, S, S could be two orders of magnitude greater if the accretion rates of $\sim 10^{-5}$ to $\sim 10^{-6}$ solar masses $year^{-1}$, or S could also be four orders of magnitude less if the mass accretion rate was $\sim 10^{-8}$ to 10^{-10} solar masses $year^{-1}$ and $F \sim 0.0001$.

2.3. Effective Ancient Production Rate

The effective ancient ^{7}Be outflow rate, P in units of s^{-1}, is given by:

$$P = p \cdot f \tag{2}$$

where p is the ancient production rate and f is the fraction of the solar wind ^{7}Be that enters the CAI-forming region; $f = 0.1$. (See Bricker & Caffee [2] [3] for a discussion of factor f). The ^{7}Be production rate is calculated assuming that SEPs are characterized by a power law relationship:

$$\frac{dF}{dE} = kE^{-r} \tag{3}$$

where r ranges from 2.5 to 4. For impulsive flares, *i.e.* $r = 4$, we use ^{3}He/H = 0.1 and ^{3}He/H = 0.3, and for gradual flares, *i.e.* $r = 2.5$, we use ^{3}He/H = 0. For all spectral indices, we assume α/H = 0.1. Contemporary SEP flux rates at the Sun-Earth distance of 1 AU are ~100 protons $cm^{-2} \cdot s^{-1}$ for $E > 10$ MeV [22]. We assume an increase in ancient particle fluxes over the current particle flux of ~4 $\times 10^5$ [2] [4], yielding an energetic particle flux rate of 3.7×10^{12} protons $cm^{-2} \cdot s^{-1}$ for $E > 10$ MeV at the surface of the proto-Sun.

The production rates for cosmogenic nuclides can be calculated via:

$$p = \sum_i N_i \int \sigma_{ij} \frac{dF(E)}{dE_j} dE \tag{4}$$

where i represents the target elements for the production of the considered nuclide, N_i is the abundance of the target element ($g \cdot g^{-1}$), j indicates the energetic particles that cause the reaction, $\sigma_{ij}(E)$ is the cross section for the production of the nuclide from the interaction of particle j with energy E from target i for the considered reaction (cm^2), and $\frac{dF(E)}{dE_j} dE$ is the differential energetic particle flux of particle j at energy E ($cm^{-2} \cdot s^{-1}$) [22]. We assume gaseous oxygen target particles of solar composition [23].

The cross-section we use to calculate ^{7}Be production from protons and ^{4}He pathways is from Sisterson *et al.* [24], and the cross-section we use for production from ^{3}He is from Gounelle *et al.* [25]. The Sisterson *et al.* [24] cross-section is experimental obtained, and the Gounelle *et al.* [25] cross-section is a combination of experimental data, fragmentation and Hauser-Feshbach codes. The un-

certainty associated with model codes are at best a factor of two. Taking into account both target abundance and nuclear cross-sections, the reaction with oxygen as the target is the primary production pathway. Any other nuclear reaction would add little to the overall ^{7}Be production rate. Table 2 shows the nuclear reactions considered in the calculations.

3. Results

The content of ^{7}Be found in refractory material, in atoms g^{-1}, predicted by SWIM is given by:

$$N^{7\mathrm{Be}} = \frac{P}{S} = \frac{p \cdot f}{\dot{M}_D \cdot X_r \cdot F} \tag{5}$$

where P is given atoms s^{-1} and S is given in g·s^{-1}.

Using the refractory mass inflow rate, S, of 2.5×10^{14} g·s^{-1} from Equation (1), and calculations of P, the effective ancient ^{7}Be outflow rate, from Equation (2) & Equation (4), we determine the content of ^{7}Be in CAIs in atoms g^{-1} using Equation (5), and find the associated isotopic ratio for different flare parameters given in Table 3. Figure 2 depicts the ^{7}Be isotopic ratio predicted by the SWIM from SEPs.

4. Discussion

Similar to ^{10}Be, the primary target for SEP production of ^{7}Be is oxygen. As such, the SEP origin of ^{7}Be and ^{10}Be are uniquely intertwined. The estimated ^{7}Be/^{10}Be production ratio from MeV SEPs in the early solar system is estimated to be ~70 [14]. Using the production rate from Equation (4) and the production rate for ^{10}Be from Bricker & Caffee [2] from SEP interaction with oxygen targets, we obtain a production ratio of ~50, which is similar to Leya [14]. It would then be expected that the original ratio of ^{7}Be/^{9}Be found in CAIs would be ~50 times greater than the ^{10}Be/^{9}Be ratio, assuming the simple SWIM mechanism described above. Using 9.5×10^{-4} [13] as the canonical ^{10}Be/^{9}Be ratio, the ^{7}Be/^{9}Be ratio would scale to 4.8×10^{-2}. We find this ratio is reproducible within a factor of ~5, the uncertainty associated with SWIM, for spectral indices $r > 3.2$. The SWIM can account for the scaled up ^{7}Be/^{9}Be ratio. Figure 3 below details the ratio of ^{7}Be/^{9}Be from SWIM to 4.8×10^{-2}.

Experimentally obtained measurements for the original ^{7}Be/^{9}Be ratio in CAIs are limited and a matter of considerable debate. Limited experimentally determined values for the ratio range from about 1.2×10^{-3} [11] to 6.1×10^{-3} [10]. The experimentally obtained ratios are at least a factor of 10 less than SWIM

Table 2. Nuclear reactions considered in this paper.

^{16}O(p, x)^{7}Be
^{16}O(^{3}He, x)^{7}Be
^{16}O(^{4}He, x)^{7}Be

Table 3. Predicted ^{7}Be content in CAIs.

Flare Parameter	atoms g^{-1} (in CAIs)	Isotopic Ratio
$p = 2.7$, ^{3}He/H = 0	1.1×10^{16}	1.6
$p = 4$, ^{3}He/H = 0.1	3.8×10^{14}	5.7×10^{-2}
$p = 4$, ^{3}He/H = 0.3	1.1×10^{15}	1.6×10^{-1}

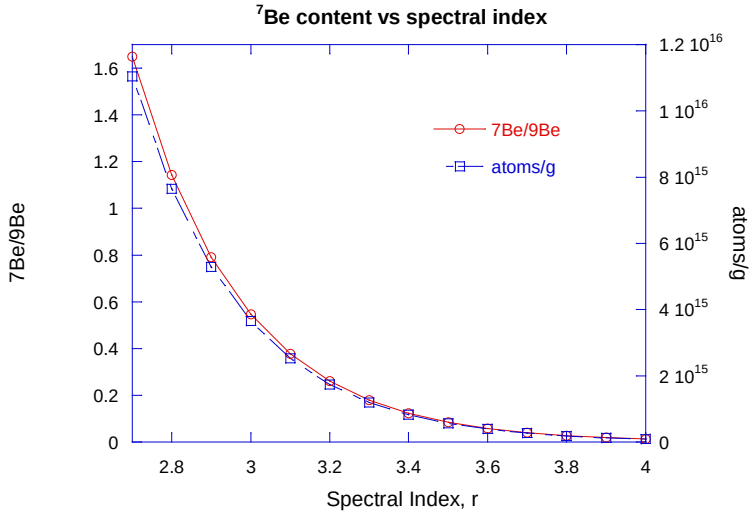

Figure 2. Predicted ^{7}Be content in CAIs from energetic protons as a function of solar flare parameter.

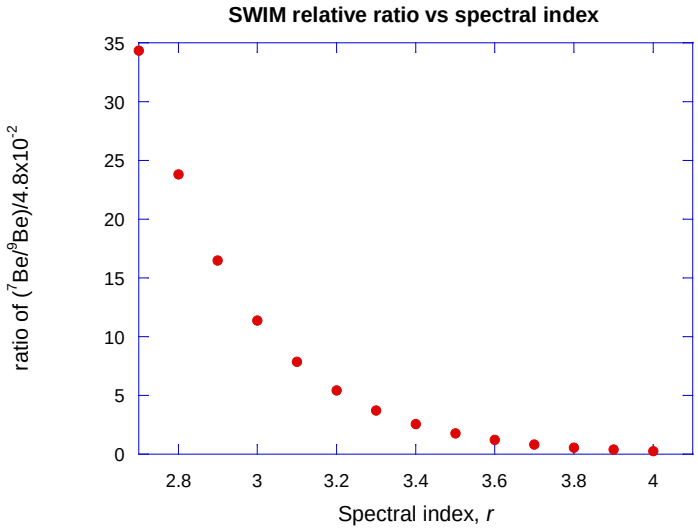

Figure 3. Ratio of ^{7}Be/^{9}Be found from SWIM.A ratio of one indicates exact match, a ratio greater than one indicates overproduction, and a ratio less than one indicates underproduction.

calculations, and also a factor of at least 10 less than the scaled up ^{7}Be/^{9}Be found from scaling the canonical ^{10}Be/^{9}Be ratio to ^{7}Be and ^{10}Be production rates. **Figure 4** depicts the ratio of SWIM obtained ratio to the canonical ^{7}Be/^{9}Be ratio.

Clearly, some other mechanism is needed to explain the overproduction of the

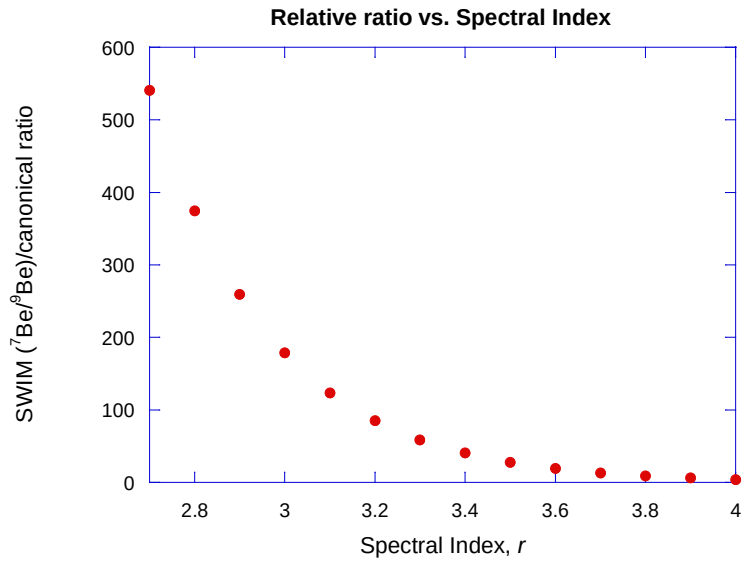

Figure 4. Ratio of SWIM ^{9}Be/^{10}Be ratio to canonical ^{7}Be/^{9}Be ratio. A factor greater than one indicates overproduction relative to canonical.

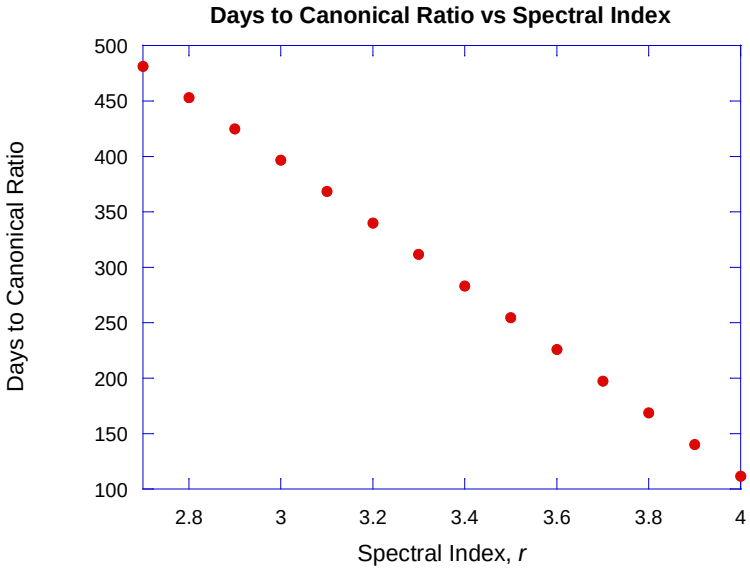

Figure 5. Days to canonical ratio vs. spectral index.

^{7}Be/^{9}Be ratio, both in terms of SWIM calculations and the scaling of the ^{10}Be/^{9}Be to relative ^{7}Be and ^{10}Be production rates.

An assumption of SWIM is that radionuclides are produced via SEP interaction and then immediately incorporated into CAI precursor materials. With a half-life of 53 days, it is possible that some temporal evolution occurs before ^{7}Be becomes implanted. Figure 5 shows days to canonical ratio for spectral index.

Figure 5 shows that with a delay on the order of ~100 days from the time of production of ^{7}Be to implantation in to CAI precursor materials, the canonical ratio is replicated. Taking into account the time from production of the radio-

nuclide to implantation into CAI precursors, *i.e.*, two half-lives of ^{7}Be, explains the deficit in ^{7}Be/^{10}Be measured ratio in comparison to the ^{7}Be/^{10}Be production ratio. It is possible and likely for nuclei to have some finite residence time in the photosphere. Calculations of this residence time have not been performed and are beyond the scope of this paper. Our *ad hoc* choice of two half-lives of residence time for ^{7}Be was to explain the ^{7}Be/^{10}Be measured ratio in comparison to the ^{7}Be/^{10}Be production ratio.

Conflicts of Interest

The author declares no conflicts of interest regarding the publication of this paper.

References

[1] Gounelle, M., Chaussidon, M. and Montmerle, T. (2007) Irradiation in the Early Solar System and the Origin of Short-Lived Radionuclides. *Comptes Rendus Geoscience*, **339**, 885-894. https://doi.org/10.1016/j.crte.2007.09.016

[2] Bricker, G.E. and Caffee, M.W. (2010) Solar Wind Implantation Model for ^{10}Be in CAIs. *Astrophysical Journal*, **725**, 443-449. https://doi.org/10.1088/0004-637X/725/1/443

[3] Bricker, G.E. and Caffee, M.W. (2013) Incorporation of ^{36}Cl in Calcium-Aluminum-Rich Inclusions in the Solar Wind Implantation Model. *Advances in Astronomy*, **2013**, Article ID: 487606. https://doi.org/10.1155/2013/487606

[4] Feigelson, E.D., Garmire, G.P. and Pravdo, S.H. (2002) Magnetic Flaring in the Pre-Main-Sequence Sun and Implications for the Early Solar System. *Astrophysical Journal*, **572**, 335-349. https://doi.org/10.1086/340340

[5] Nishiizumi, K. and Caffee, M.W. (2001) Beryllium-10 from the Sun. *Science*, **294**, 352-354. https://doi.org/10.1126/science.1062545

[6] Bricker, G.E. (2013) Calculation of ^{10}Be and ^{14}C in the Solar Atmosphere: Implication for Solar Flare Spectral Index. *International Journal of Astronomy and Astrophysics*, **3**, 17-20. https://doi.org/10.4236/ijaa.2013.32A003

[7] Jull, A.J.T., Lal, D., McHargue, L.R., Burr, G.S. and Donahue, D.J. (2000) Cosmogenic and Implanted Radionuclides Studied by Selective Etching of Lunar Soils. *Nuclear Instruments & Methods in Physics Research Section B*, **172**, 867-872. https://doi.org/10.1016/S0168-583X(00)00232-9

[8] Jaeger, M., Wilmes, S., Kölle, V., Staudt, G. and Mohr, P. (1996) Precision Measurement of the Half-Life of ^{7}Be. *Physical Review*, **C54**, 423-424. https://doi.org/10.1103/PhysRevC.54.423

[9] Mandzhavidz, N., Ramaty, R. and Kozlovsky, B. (1997) Solar Atmospheric and Solar Flare Accelerated Helium Abundances from Gamma-Ray Spectroscopy. *Astrophysical Journal*, **489**, L99-L102. https://doi.org/10.1086/310965

[10] Chaussidon, M., Robert, F. and McKeegan, K. (2006) Li and B Isotopic Variations in an Allende CAI: Evidence for the *In Situ* Decay of Short-Lived 10Be and for the Possible Presence of the Short-Lived Nuclide ^{7}Be in the Early Solar System. *Geochimica et Cosmochimiva Acta*, **70**, 224-225. https://doi.org/10.1016/j.gca.2005.08.016

[11] Mishra, R. and Marhas, K. (2018) Fossil Record of ^{7}Be and ^{10}Be in a Cai: Implications for the Origin and Early Evolution of Our Solar System. 81*st Annual Meeting*

of the Meteoritical Society, Moscow, 22-27 July 2018, Article ID: 6125.

[12] Nishiizumi, K., Imamura, M., Caffee, M., Southon, J., Finkel, R. and McAnich, J. (2007) Absolute Calibration of ^{10}Be AMS Standards. *Nuclear Instruments and Methods in Physics Research B: Beam Interactions with Materials and Atoms*, **258**, 403-413. https://doi.org/10.1016/j.nimb.2007.01.297

[13] McKeegan, K., Chaussidon, M. and Robert, F. (2000) Incorporation of Short-Lived ^{10}Be in a Calcium-Aluminum-Rich Inclusion from the Allende Meteorite. *Science*, **289**, 1334-1337. https://doi.org/10.1126/science.289.5483.1334

[14] Leya, I., Wieler, R. and Halliday, A.N. (2003) The Predictable Collateral Consequences of Nucleosynthesis by Spallation Reactions in the Early Solar System. *Astrophysical Journal*, **594**, 605-616. https://doi.org/10.1086/376795

[15] Duprat, J. and Tatischeff, V. (2008) On Non-Thermal Nucleosynthesis of Short-Lived Radionuclei in the Early Solar System. *New Astronomy Reviews*, **52**, 463-466. https://doi.org/10.1016/j.newar.2008.06.016

[16] Shu, F.H., Shang, H. and Lee, T. (1996) Toward an Astrophysical Theory of Chondrites. *Science*, **271**, 1545-1552. https://doi.org/10.1126/science.271.5255.1545

[17] Shu, F.H., Shang, H., Glassgold, A.E. and Lee, T. (1997) X-Rays and Fluctuating X-Winds from Protostars. *Science*, **277**, 1475-1479. https://doi.org/10.1126/science.277.5331.1475

[18] Shu, F.H., Shang, H., Glassgold, A.E. and Lee, T. (2001) The Origin of Chondrules and Refractory Inclusions in Chondritic Meteorites. *Astrophysical Journal*, **548**, 1029-1050. https://doi.org/10.1086/319018

[19] Shu, F.H., Shang, H., Glassgold, A.E. and Rehm, K.E. (1998) Protostellar Cosmic Rays and Extinct Radioactivities in Meteorites. *Astrophysical Journal*, **506**, 898-912. https://doi.org/10.1086/306284

[20] Calvet, N., Briceno, B., Hernandez, J., Hoyer, S., Hartmann, L., Sicila, Megeath, S.T. and D'Alessio, P. (2005) Disk Evolution in the Orion OB1 Association. *Astronomical Journal*, **129**, 935-946. https://doi.org/10.1086/426910

[21] Ward-Thompson, D. (1996) The Formation and Evolution of Low Mass Protostars. *Astrophysics & Space Science*, **239**, 151-170. https://doi.org/10.1007/BF00653775

[22] Reedy, R.C. and Marti, K. (1991) Solar-Cosmic-Ray Fluxes during the Last 10 Million Years. In: Sonnet, C.P., Giampapa, M.S. and Mathews, M.S., Eds., *The Sun in Time*, University of Arizona Press, Tucson, 260-287.

[23] Lodders, K. (2003) Solar System Abundances and Condensation Temperatures of the Elements. *The Astrophysical Journal*, **591**, 1220-1247. https://doi.org/10.1086/375492

[24] Sisterson, J., *et al.* (1997) Measurement of Proton Production Cross Sections of ^{10}Be and ^{26}Al from Elements Found in Lunar Rocks. *Nuclear Instruments and Methods in Physics Research Section B: Beam Interactions with Materials and Atoms*, **123**, 324-329. https://doi.org/10.1016/S0168-583X(96)00409-0

[25] Gounelle, M., Shu, F.H., Shang, H., Glassgold, A.E., Rehm, K.E. and Lee, T. (2006) The Irradiation Origin of Beryllium Radioisotopes and Other Short-Lived Radionuclides. *The Astrophysical Journal*, **640**, 1163-1189. https://doi.org/10.1086/500309

International Journal of Astronomy and Astrophysics, 2019, 9, 21-38
http://www.scirp.org/journal/ijaa
ISSN Online: 2161-4725
ISSN Print: 2161-4717

Libration Points in the R3BP with a Triaxial Rigid Body as the Smaller Primary and a Variable Mass Infinitesimal Body

M. R. Hassan[1], Sweta Kumari[2], R. R. Thapa[3], Md. Aminul Hassan[4]

[1]Department of Mathematics, S. M. College, T. M. Bhagalpur University, Bhagalpur, India
[2]T. M. Bhagalpur University, Bhagalpur, India
[3]Department of Mathematics, P. G. Campus, Tribhuvan University, Biratnagar, Nepal
[4]GTE, Bangalore, India
Email: hassansmc@gmail.com, mahassan012@gmail.com

How to cite this paper: Hassan, M.R., Kumari, S., Thapa, R.R. and Hassan, Md.A. (2019) Libration Points in the R3BP with a Triaxial Rigid Body as the Smaller Primary and a Variable Mass Infinitesimal Body. *International Journal of Astronomy and Astrophysics*, **9**, 21-38.
https://doi.org/10.4236/ijaa.2019.91003

Received: November 8, 2018
Accepted: March 2, 2019
Published: March 5, 2019

Abstract

The paper deals with the existence of the coplanar libration points in the restricted three-body problem when the smaller primary is a triaxial rigid body and the infinitesimal body is of variable mass. Following small parameter method, the coordinates of collinear libration points are established whereas the coordinates of triangular libration points are established by classical method. It is found that the mass reduction factor has small effect but triaxiality parameters of the smaller primary have great effects on the coordinates of the libration points.

Keywords

Restricted Three-Body Problem, Jean's Law, Space-Time Transformation, Triaxiality, Mass Reduction Factors, Libration Points

1. Introduction

Restricted three-body problem with variable mass has an important role in celestial mechanics. The phenomenon of isotropic radiation or absorption in stars was studied by the leading scientists to formulate the restricted three-body problem with variable mass. The two body problem with variable mass was studied by Jeans [1] regarding the evaluation of binary system. Meshcherskii [2] assumed that the mass is ejected isotropically from the two body system at very high velocities and is lost to the system. He examined the change in orbits, the variation in angular momentum and the energy of the system. Shrivastava and

Ishwar [3] derived the equations of motion of the circular restricted three-body problem with variable mass with the assumption that the mass of the infinitesimal body varies with respect to time. Singh and Ishwar [4] showed the effect of perturbation due to oblateness on the existence and stability of the triangular libration points in the restricted three-body problem.

Das *et al.* [5] developed the equations of motion of elliptic restricted three-body problem with variable mass. Lukyanov [6] discussed the stability of libration points in the restricted three-body problem with variable mass. He has found that for any set of parameters, all the libration points in the problem (Collinear, Triangular) are stable with respect to the conditions considered by the Meshcherskii's space-time transformation. El Shaboury [7] had established the equations of motion of elliptic restricted three-body problem (ER3BP) with variable mass with two triaxial rigid primaries. He has applied the Jeans law, Nechvili's transformation and space-time transformation given by Meshcherskii in a special case.

Singh *et al.* [8] have discussed the non-linear stability of libration points in the restricted three-body problem with variable mass. They have found that in non-linear sense, collinear points are unstable for all mass ratios and the triangular points are stable in the range of linear stability except for three mass ratios depending upon the mass variation parameter β governed by Jean's law. Hassan *et al.* [9] studied the existence of libration points with variable mass in the R3BP when the smaller primary is an oblate spheroid. They found that Jacobi constant $C=1, C=2$ shows no effect in the position of libration points, but for $C=3$, slight shifting of libration points is found due to oblateness only not due to the mass reduction factor α.

In present work, we have established coordinates of five libration points $L_i\left(i=1,2,3,4,5\right)$ in the R3BP with variable mass when smaller primary is a triaxial rigid body by small parameter method [10] and the method used by Hassan *et al.* [9].

2. Equations of Motion

Let the two primaries of non-dimensional masses μ and $1-\mu$ be moving on the circular orbits about their centre of mass. In **Figure 1**, we consider a bary-centric coordinate system $\left(O, XYZ\right)$ rotating relative to the inertial frame with angular velocity ω. The line joining the centers of P_1 and P_2 of the primaries is considered as the *x*-axis and a line lying on the plane of motion and perpendicular to the *x*-axis and through the centre of mass; as the *y*-axis and a line through the centre of mass and perpendicular to the plane of motion as the *z*-axis. Let $\left(\mu,0,0\right)$ and $\left(\mu-1,0,0\right)$ respectively be the coordinates of P_1 and P_2 and $\left(x,y,z\right)$ be the coordinates of the infinitesimal body of variable mass *m* at *P*.

The equation of motion of the infinitesimal body of variable mass *m* can be written as

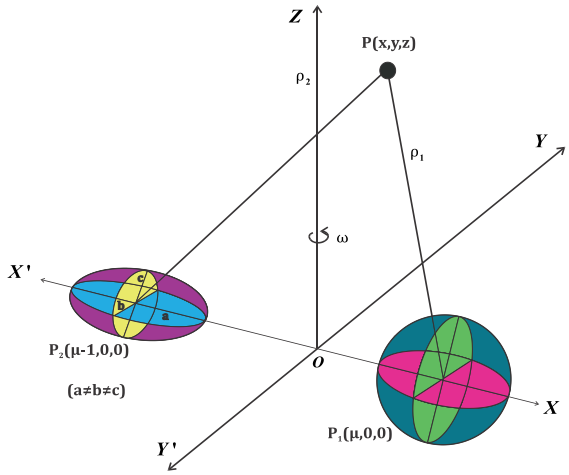

Figure 1. Configuration of R3BP when smaller primary is triaxial.

$$\begin{aligned}&\frac{\mathrm{d}}{\mathrm{d}t}\left(m\frac{\mathrm{d}\boldsymbol{r}}{\mathrm{d}t}\right)\\&=-Gm\left[\frac{1-\mu}{\rho_1^3}\boldsymbol{\rho}_1+\frac{\mu}{\rho_2^3}\boldsymbol{\rho}_2+\frac{3\mu(2\sigma_1-\sigma_2)}{2\rho_2^5}\boldsymbol{\rho}_2+\frac{3\mu}{\rho_2^5}\left\{(\sigma_1-\sigma_2)y\hat{j}+\sigma_1 z\hat{k}\right\}\right.\\&\left.-\frac{15\mu}{2\rho_2^7}\left\{(\sigma_1-\sigma_2)y^2+\sigma_1 z^2\right\}\boldsymbol{\rho}_2\right],\end{aligned}\tag{1}$$

the differential operators are given by the relations

$$\begin{aligned}&\frac{\mathrm{d}}{\mathrm{d}t}=\frac{\partial}{\partial t}+\boldsymbol{\omega}\times\quad\text{and}\quad\frac{\mathrm{d}\boldsymbol{r}}{\mathrm{d}t}=\frac{\partial\boldsymbol{r}}{\partial t}+\boldsymbol{\omega}\times\boldsymbol{r}\\&\boldsymbol{r}=x\hat{i}+y\hat{j}+z\hat{k},\quad\boldsymbol{\rho}_1=(x-\mu)\hat{i}+y\hat{j}+z\hat{k},\quad\boldsymbol{\rho}_2=(x-\mu+1)\hat{i}+y\hat{j}+z\hat{k},\\&\omega^2=1+\frac{3}{2}(2\sigma_1-\sigma_2),\quad\sigma_1=\frac{a^2-c^2}{5R^2},\quad\sigma_2=\frac{b^2-c^2}{5R^2},\end{aligned}\tag{2}$$

where a,b,c are the semi-axes of the triaxial rigid body, R is the dimensional distance between the centre of the primaries. Thus using Equation (2) in (1), we get

$$\begin{aligned}&m\ddot{\boldsymbol{r}}+\dot{m}\left(\dot{\boldsymbol{r}}+\boldsymbol{\omega}\times\boldsymbol{r}\right)+2m\boldsymbol{\omega}\times\boldsymbol{r}-\omega^2 m\left(x\hat{i}+y\hat{j}\right)\\&=-Gm\left[\frac{1-\mu}{\rho_1^3}\boldsymbol{\rho}_1+\frac{\mu}{\rho_2^3}\boldsymbol{\rho}_2+\frac{3\mu(2\sigma_1-\sigma_2)}{2\rho_2^5}\boldsymbol{\rho}_2-\frac{15\mu}{2\rho_2^7}\left\{(\sigma_1-\sigma_2)y^2+\sigma_1 z^2\right\}\boldsymbol{\rho}_2\right.\\&\left.+\frac{3\mu}{\rho_2^5}\left\{(\sigma_1-\sigma_2)y\hat{j}+\sigma_1 z\hat{k}\right\}\right].\\&\Rightarrow\left\{m\ddot{x}+\dot{m}(x-\omega\dot{y})-2m\omega\dot{y}-m\omega^2 x\right\}\hat{i}\\&\quad+\left\{m\ddot{y}+\dot{m}(y+\omega\dot{x})+2m\omega\dot{x}-m\omega^2 y\right\}\hat{j}+(m\ddot{z}+\dot{m}\dot{z})\hat{k}\\&\quad=Gm\left[-\frac{1-\mu}{\rho_1^3}\boldsymbol{\rho}_1-\frac{\mu}{\rho_2^3}\boldsymbol{\rho}_2-\frac{3\mu}{2\rho_2^5}(2\sigma_1-\sigma_2)\boldsymbol{\rho}_2-\frac{3\mu}{\rho_2^5}\left\{(\sigma_1-\sigma_2)y\hat{j}+\sigma_1 z\hat{k}\right\}\right.\\&\quad\left.+\frac{15\mu}{2\rho_2^7}\left\{(\sigma_1-\sigma_2)y^2+\sigma_1 z^2\right\}\boldsymbol{\rho}_2\right].\end{aligned}\tag{3}$$

Choosing units of mass and distance in such way that $G=1$ and $R=1$, then the equations of motion of the infinitesimal body in cartesian form can be

written as:

$$\begin{aligned}
&\ddot{x}+\frac{\dot{m}}{m}\left(\dot{x}-\omega y\right)+2\omega\dot{x}=-\frac{1}{m}\frac{\partial U}{\partial x},\\
&\ddot{y}+\frac{\dot{m}}{m}\left(\dot{y}+\omega x\right)-2\omega\dot{y}=-\frac{1}{m}\frac{\partial U}{\partial y},\\
&\ddot{z}+\frac{\dot{m}}{m}\dot{z}=\frac{1}{m}\frac{\partial U}{\partial z},
\end{aligned}\tag{4}$$

where

$$U=-\frac{m\omega^2}{2}\left(x^2+y^2\right)-m\left[\frac{1-\mu}{\rho_1}+\frac{\mu}{\rho_2}-\frac{\mu\left(2\sigma_1-\sigma_2\right)}{2\rho_2^3}-\frac{3\mu\left\{\left(\sigma_1-\sigma_2\right)y^2+\sigma_1 z^2\right\}}{2\rho_2^5}\right],\tag{5}$$

$$\begin{aligned}
-\frac{1}{m}\frac{\partial U}{\partial x}&=\omega^2 x-\frac{(1-\mu)(x-\mu)}{\rho_1^{\,3}}-\frac{\mu(x-\mu-1)}{\rho_2^3}-\frac{3\mu(2\sigma_1-\sigma_2)(x-\mu-1)}{2\rho_2^5}\\
&\quad+\frac{15\mu(\sigma_1-\sigma_2)(x-\mu-1)y^2}{2\rho_2^7}+\frac{15\mu\sigma_1(x-\mu-1)z^2}{2\rho_2^7},
\end{aligned}$$

$$-\frac{1}{m}\frac{\partial U}{\partial y}=\omega^2 y-\frac{(1-\mu)y}{\rho_1^{\,3}}-\frac{\mu y}{\rho_2^3}-\frac{3\mu(2\sigma_1-\sigma_2)y}{2\rho_2^5}+\frac{15\mu(\sigma_1-\sigma_2)y^3}{2\rho_2^7}+\frac{15\mu\sigma_1 yz^2}{2\rho_2^7}\tag{6}$$

and

$$-\frac{1}{m}\frac{\partial U}{\partial z}=-\frac{(1-\mu)z}{\rho_1^{\,3}}-\frac{\mu z}{\rho_2^3}+\frac{3\mu(2\sigma_1-\sigma_2)z}{2\rho_2^5}+\frac{15\mu(\sigma_1-\sigma_2)y^2 z}{2\rho_2^7}+\frac{15\mu\sigma_1 z^3}{2\rho_2^7}.$$

By Jeans law, the variation of mass of the infinitesimal body is given by

$$\frac{\mathrm{d}m}{\mathrm{d}t}=-\alpha m^n \quad i.e.,\ \frac{\dot{m}}{m}=-\alpha m^{n-1},\tag{7}$$

where α is a constant and the value of exponent $n\in[0.4,4.4]$ for the stars of the main sequence (from Observational facts).

Let us introduce Meshcherskii's space time transformations [2] as:

$$\begin{aligned}
&x=\xi\gamma^{-q},\quad y=\eta\gamma^{-q},\quad \zeta=z\gamma^{-q},\quad \mathrm{d}t=\gamma^{-k}\mathrm{d}\tau,\\
&\rho_1=r_1\gamma^{-q},\quad \rho_2=r_2\gamma^{-q}\qquad \text{where } \gamma=\frac{m}{m_0}<1,
\end{aligned}\tag{8}$$

m_0 is the mass of the infinitesimal body when $t=0$ and τ is the pseudo time.

From Equation (7) and Equation (8), we get

$$\frac{\mathrm{d}\gamma}{\mathrm{d}t}=-\beta\gamma^{n-1},\tag{9}$$

where $\beta=\alpha m_0^{n-1}=\text{constant}$.

Differentiating x,y,z with respect to t twice and using fourth equation of (8), we get

$$\begin{aligned}
\dot{x}&=\xi'\gamma^{k-q}+\beta q\xi\gamma^{n-q-1},\\
\dot{y}&=\eta'\gamma^{k-q}+\beta q\eta\gamma^{n-q-1},\\
\dot{z}&=\zeta'\gamma^{k-q}+\beta q\zeta\gamma^{n-q-1},\\
\ddot{x}&=\xi''\gamma^{2k-q}+\beta\xi'(2q-k)\gamma^{n+k-q-1}-\beta^2 q\xi(n-q-1)\gamma^{2n-q-2},\\
\ddot{y}&=\eta''\gamma^{2k-q}+\beta\eta'(2q-k)\gamma^{n+k-q-1}-\beta^2 q\eta(n-q-1)\gamma^{2n-q-2},\\
\ddot{z}&=\zeta''\gamma^{2k-q}+\beta\zeta'(2q-k)\gamma^{n+k-q-1}-\beta^2 q\zeta(n-q-1)\gamma^{2n-q-2},
\end{aligned}\tag{10}$$

where dot $(\bullet)$ represents differentiation with respect to real time t and prime $(')$ represents the differentiation with respect to pseudotime τ.

Also,

$$\frac{\dot{m}}{m} = -\alpha m^{n-1} = -\alpha\left(m_0\gamma\right)^{n-1} = -\alpha m_0^{n-1}\gamma^{n-1} \quad \text{i.e.,} \quad \frac{\dot{m}}{m} = -\beta\gamma^{n-1}.$$

Replacing the values of Equation (10) in Equation (4) to obtain

$$\begin{aligned}
&\xi'' + (2q-k-1)\beta\xi'\gamma^{n-k-1} - 2\omega\eta'\gamma^{-k} - (n-q)\beta^2 q\xi\gamma^{2(n-k-1)} \\
&-(2q-1)\beta\omega\eta\gamma^{n-q-1} = -\frac{\gamma^{2q-2k-1}}{m_0}\frac{\partial U}{\partial\xi}, \\
&\eta'' + (2q-k-1)\beta\eta'\gamma^{n-k-1} + 2\omega\xi'\gamma^{-k} - (n-q)\beta^2 q\eta\gamma^{2(n-k-1)} \\
&+(2q-1)\beta\omega\xi\gamma^{n-q-1} = -\frac{\gamma^{2q-2k-1}}{m_0}\frac{\partial U}{\partial\eta}, \\
&\zeta'' + (2q-k-1)\beta\zeta'\gamma^{n-k-1} - (n-q)\beta^2 q\zeta\gamma^{2(n-k-1)} = -\frac{\gamma^{2q-2k-1}}{m_0}\frac{\partial U}{\partial\zeta},
\end{aligned} \tag{11}$$

where

$$\begin{aligned}
U = -m_0\Bigg[&\frac{1}{2}\left(\xi^2+\eta^2\right)\omega^2\gamma^{1-2q} + \frac{1-\mu}{r_1}\gamma^{q+1} + \frac{\mu}{r_2}\gamma^{q+1} + \frac{\mu(2\sigma_1-\sigma_2)}{2r_2^3}\gamma^{3q+1} \\
&-\frac{3\mu(\sigma_1-\sigma_2)\eta^2\gamma^{3q+1}}{2r_2^5} - \frac{3\mu\sigma_1\zeta^2\gamma^{7q+1}}{2r_2^5}\Bigg].
\end{aligned}$$

As the mass of the infinitesimal body is variable, so only the variational factors but not the non-variational factors should be taken into consideration in the equations of motion of the infinitesimal body. Thus to avoid the non-variational factors, we have

$$\begin{aligned}
&n-k-1=0, \quad 2q-k-1=0, \quad n=1\in[0.4,4.4], \\
&\text{i.e, } k=0, q=\frac{1}{2}, \quad n=1 \text{ and } \beta=\alpha.
\end{aligned} \tag{12}$$

Thus the Equations (11) reduced to

$$\begin{aligned}
\text{i.e, } \xi'' - 2\omega\eta' &= -\frac{1}{m_0}\frac{\partial U}{\partial\xi} + \frac{\alpha^2}{4}\xi, \\
\eta'' - 2\omega\xi' &= -\frac{1}{m_0}\frac{\partial U}{\partial\eta} + \frac{\alpha^2}{4}\eta, \\
\zeta'' &= -\frac{1}{m_0}\frac{\partial U}{\partial\zeta} + \frac{\alpha^2}{4}\zeta,
\end{aligned} \tag{13}$$

where

$$\begin{aligned}
U = -m_0\Bigg[&\frac{1}{2}\left(\xi^2+\eta^2\right)\omega^2 + \frac{(1-\mu)}{r_1}\gamma^{\frac{3}{2}} + \frac{\mu}{r_2}\gamma^{\frac{3}{2}} + \frac{\mu(2\sigma_1-\sigma_2)}{2r_2^3}\gamma^{\frac{5}{2}} \\
&-\frac{3\mu}{2\rho_2^5}\gamma^{\frac{7}{2}}\left\{(\sigma_1-\sigma_2)\eta^2\gamma^{-1} + \sigma_1\zeta^2\gamma\right\}\Bigg],
\end{aligned} \tag{14}$$

$$
\begin{aligned}
-\frac{1}{m_0}\frac{\partial U}{\partial \xi} &= \omega^2\xi - \frac{(1-\mu)\left(\xi-\mu\sqrt{\gamma}\right)}{r_1^3}\gamma^{\frac{3}{2}} - \frac{\mu\left(\xi-\mu\sqrt{\gamma}+\sqrt{\gamma}\right)}{r_2^3}\gamma^{\frac{3}{2}} \\
&\quad + \frac{3\mu(2\sigma_1-\sigma_2)\left(\xi-\mu\sqrt{\gamma}+\sqrt{\gamma}\right)}{2r_2^5}\gamma^{\frac{5}{2}} \\
&\quad + \frac{15\mu\left(\xi+\sqrt{\gamma}-\mu\sqrt{\gamma}\right)}{2r_2^7}\gamma^{\frac{7}{2}}\left\{(\sigma_1-\sigma_2)\eta^2\gamma^{-1}+\sigma_1\zeta^2\gamma\right\}, \\
-\frac{1}{m_0}\frac{\partial U}{\partial \eta} &= \omega^2\eta - \frac{(1-\mu)\eta}{r_1^3}\gamma^{\frac{3}{2}} - \frac{\mu\eta}{r_2^3}\gamma^{\frac{3}{2}} + \frac{3\mu(2\sigma_1-\sigma_2)\eta}{2r_2^5}\gamma^{\frac{5}{2}} \\
&\quad + \frac{15\mu\eta}{2r_2^7}\gamma^{\frac{7}{2}}\left\{(\sigma_1-\sigma_2)\eta^2\gamma^{-1}+\sigma_1\zeta^2\gamma\right\}, \\
-\frac{1}{m_0}\frac{\partial U}{\partial \zeta} &= -\frac{(1-\mu)\zeta}{r_1^3}\gamma^{\frac{3}{2}} - \frac{\mu\zeta}{r_2^3}\gamma^{\frac{3}{2}} + \frac{3\mu(2\sigma_1-\sigma_2)\zeta}{2r_2^5}\gamma^{\frac{5}{2}} \\
&\quad + \frac{15\mu\zeta}{2r_2^7}\gamma^{\frac{7}{2}}\left\{(\sigma_1-\sigma_2)\eta^2\gamma^{-1}+\sigma_1\zeta^2\gamma\right\}.
\end{aligned} \tag{15}
$$

The Jacobi integral in Meshcherskii's space is

$$
\begin{aligned}
&\xi'^2+\eta'^2+\zeta'^2 \\
&= 2\left[\frac{\omega^2}{2}\left(\xi^2+\eta^2\right)+\frac{1-\mu}{r_1}\gamma^{\frac{3}{2}}+\frac{\mu}{r_2}\gamma^{\frac{3}{2}}+\frac{\mu(2\sigma_1-\sigma_2)}{2r_2^3}\gamma^{\frac{5}{2}}\left\{(\sigma_1-\sigma_2)\eta^2\gamma^{-1}+\sigma_1\zeta^2\gamma\right\}\right] \\
&\quad + \frac{\alpha^2}{4}\left(\xi^2+\eta^2+\zeta^2\right)+C,
\end{aligned} \tag{16}
$$

whereas the Jacobi integral in the rotating frame (O, XYZ) is

$$\dot{x}^2+\dot{y}^2+\dot{z}^2 = 2\Omega(x,y,z,\alpha,\omega,\sigma_1,\sigma_2)+C,$$

where

$$
\begin{aligned}
\Omega &= \frac{\omega^2}{2}\left(x^2+y^2\right)+\frac{1-\mu}{\rho_1}+\frac{\mu}{\rho_2}+\frac{\mu(2\sigma_1-\sigma_2)}{2\rho_2^3}\left\{(\sigma_1-\sigma_2)y^2+\sigma_1 z^2\right\} \\
&\quad + \frac{\alpha^2}{4}\left(x^2+y^2+z^2\right).
\end{aligned}
$$

3. Libration Points

Since in the vicinity of the libration points (Lagrangian points), no translatory motion exists, only vibrational motion exists, hence velocity and acceleration components must vanish at these points *i.e.*, $\xi' = \eta' = \zeta' = \xi'' = \eta'' = \zeta'' = 0$.

Thus from Equations (15), we have

$$
\begin{aligned}
&\left(\frac{\alpha^2}{4}+\omega^2\right)\xi - \frac{(1-\mu)\left(\xi-\mu\sqrt{\gamma}\right)}{r_1^3}\gamma^{\frac{3}{2}} - \frac{\mu\left(\xi-\mu\sqrt{\gamma}+\sqrt{\gamma}\right)}{r_2^3}\gamma^{\frac{3}{2}} \\
&- \frac{3\mu(2\sigma_1-\sigma_2)\left(\xi-\mu\sqrt{\gamma}+\sqrt{\gamma}\right)}{2r_2^5}\gamma^{\frac{5}{2}} \\
&+ \frac{15\mu}{2r_2^7}\gamma^{\frac{7}{2}}\left(\xi-\mu\sqrt{\gamma}+\sqrt{\gamma}\right)\left\{\left((\sigma_1-\sigma_2)\eta^2\gamma^{-1}+\sigma_1\zeta^2\gamma^{-1}\right)\right\} = 0,
\end{aligned}
$$

$$\left(\frac{\alpha^2}{4}+\omega^2\right)\eta-\frac{(1-\mu)\eta}{r_1^3}\gamma^{\frac{3}{2}}-\frac{\mu\eta}{r_2^3}\gamma^{\frac{3}{2}}+\frac{3\mu(2\sigma_1-\sigma_2)}{2r_2^5}\eta\gamma^{\frac{5}{2}}$$
$$+\frac{15\mu\eta}{2r_2^7}\gamma^{\frac{5}{2}}\left\{(\sigma_1-\sigma_2)\eta^2\gamma^{-1}+\sigma_1\zeta^2\gamma^{-1}\right\}=0$$
$$\&\ \left(\frac{\alpha^2}{4}\right)\zeta-\frac{(1-\mu)\zeta}{r_1^3}\gamma^{\frac{3}{2}}-\frac{\mu\zeta}{r_2^3}\gamma^{\frac{3}{2}}+\frac{3\mu(2\sigma_1-\sigma_2)}{2r_2^5}\zeta\gamma^{\frac{5}{2}}$$
$$+\frac{15\mu\zeta}{2r_2^7}\gamma^{\frac{7}{2}}\left\{(\sigma_1-\sigma_2)\eta^2\gamma^{-1}+\sigma_1\zeta^2\gamma^{-1}\right\}=0.$$

For solving the above equations in the rotating frame $(0, XYZ)$, we apply the inverse transformation $\xi=\sqrt{\gamma}x, \eta=\sqrt{\gamma}y, \zeta=\sqrt{\gamma}z$ in the above equations to get

$$\left(\frac{\alpha^2}{4}+\omega^2\right)x-\frac{(1-\mu)(x-\mu)}{\rho_1^3}-\frac{\mu(x-\mu+1)}{\rho_2^3}+\frac{3\mu(2\sigma_1-\sigma_2)(x-\mu+1)}{2\rho_2^5}$$
$$+\frac{15\mu(x-\mu+1)}{2\rho_2^7}\left\{(\sigma_1-\sigma_2)y^2+\sigma_1z^2\right\}=0,$$
$$\left(\frac{\alpha^2}{4}+\omega^2\right)y-\frac{(1-\mu)y}{\rho_1^3}-\frac{\mu y}{\rho_2^3}+\frac{3\mu(2\sigma_1-\sigma_2)y}{2\rho_2^5}+\frac{15\mu y}{2\rho_2^7}\left\{(\sigma_1-\sigma_2)y^2+\sigma_1z^2\right\}=0, \quad (17)$$
$$\left(\frac{\alpha^2}{4}\right)z-\frac{(1-\mu)z}{\rho_1^3}-\frac{\mu z}{\rho_2^3}+\frac{3\mu(2\sigma_1-\sigma_2)z}{2\rho_2^5}+\frac{15\mu z}{2\rho_2^7}\left\{(\sigma_1-\sigma_2)y^2+\sigma_1z^2\right\}=0.$$

4. Collinear Libration Points

As we know that all the three collinear libration points lie on the *x*-axis (the line joining the centre of the first and second primary) so $y=0, z=0$ and hence from Equation (2)

$$\rho_1^2=(x-\mu)^2,\ \rho_2^2=(x-\mu+1)^2 \ \Rightarrow \rho_1=|x-\mu|, \rho_2=|x-\mu+1|.$$

Thus from Equations (17), we have

$$\left(\frac{\alpha^2}{4}+\omega^2\right)x-\frac{(1-\mu)(x-\mu)}{|x-\mu|^3}-\frac{\mu(x-\mu+1)}{|x-\mu+1|^3}+\frac{3\mu(2\sigma_1-\sigma_2)(x-\mu+1)}{2|x-\mu+1|^5}=0. \quad (18)$$

Let $L_1(\xi_1,0,0)$ be the first collinear libration point lying to the left of the second primary $P_2(\mu-1,0,0)$ *i.e.*, $\xi_1<\mu-1$ then $\xi_1<\mu$

$$\Rightarrow \xi_1-\mu+1<0 \text{ and } \xi_1-\mu<0,$$
$$\Rightarrow |\xi_1-\mu+1|=-(x-\mu+1) \text{ and } |\xi_1-\mu|=-(\xi_1-\mu).$$

Thus from Equation (18),

$$\left(\frac{\alpha^2}{4}+\omega^2\right)\xi_1-\frac{(1-\mu)}{(\xi_1-\mu)^2}-\frac{\mu}{(\xi_1-\mu+1)^2}+\frac{3\mu(2\sigma_1-\sigma_2)}{2(\xi_1-\mu+1)^4}=0. \quad (19)$$

As $\xi_1<\mu-1$, so let $\xi_1=\mu-1-\rho$ where ρ is a very small positive quantity.

From Equation (19)

$$\left(\frac{\alpha^2}{4}+\omega^2\right)(\mu-1-\rho)-\frac{(1-\mu)}{(-1-\rho)^2}-\frac{\mu}{\rho^2}+\frac{3\mu(2\sigma_1-\sigma_2)}{2\rho^4}=0, \tag{20}$$

$$\begin{aligned}&2\left(\frac{\alpha^2}{4}+\omega^2\right)(\mu-1-\rho)\rho^4(1+\rho)^2-2(1-\mu)\rho^4-2\mu(1+\rho)^2\rho^2\\&+3\mu(2\sigma_1-\sigma_2)(1+\rho)^2=0,\end{aligned} \tag{21}$$

$$\begin{aligned}&\left(\frac{\alpha^2}{4}+\omega^2\right)\rho^7+\left(\frac{\alpha^2}{4}+\omega^2\right)(3-\mu)\rho^6+\left(\frac{\alpha^2}{4}+\omega^2\right)(2-\mu)\rho^5\\&+\left\{\left(\frac{\alpha^2}{4}+\omega^2\right)(1-\mu)+2\right\}\rho^4+4\mu\rho^3-\mu\{3(2\sigma_1-\sigma_2)-2\}\rho^2\\&-6\mu(2\sigma_1-\sigma_2)\rho-3\mu(2\sigma_1-\sigma_2)=0.\end{aligned} \tag{22}$$

Equation (22) is seven degree polynomial equation in ρ, so there are seven values of ρ. If we put $\mu=0$ then from Equation (22), we get

$$\left\{2\left(\frac{\alpha^2}{4}+\omega^2\right)\rho^3+6\left(\frac{\alpha^2}{4}+\omega^2\right)\rho^2+4\left(\frac{\alpha^2}{4}+\omega^2\right)\rho+2\left(\frac{\alpha^2}{4}+\omega^2\right)+2\right\}\rho^4=0. \tag{23}$$

Here $\rho^4=0$ gives four roots of Equation (23) when $\mu=0$ but we know that $\mu\neq 0$ so $\rho^4\neq 0$, so there must be some order relation between ρ^4 and μ *i.e.*, ρ^4 can be expressed as the order of μ *i.e.*, $\rho=o\left(\mu^{\frac{1}{4}}\right)=o(\upsilon)$ where $\upsilon=\mu^{\frac{1}{4}}$.

Thus the Equation (20) reduces to

$$\begin{aligned}&\left(\frac{\alpha^2}{2}+2\omega^2\right)\rho^7+\left(\frac{\alpha^2}{2}+2\omega^2\right)(3-\upsilon^4)\rho^6+\left(\frac{\alpha^2}{2}+2\omega^2\right)(2-\upsilon^4)\rho^5\\&+\left\{\left(\frac{\alpha^2}{2}+2\omega^2\right)(1-\upsilon^4)+2\right\}\rho^4+4\upsilon^4\rho^3-\{3(2\sigma_1-\sigma_2)-2\}\upsilon^4\rho^2\\&-6(2\sigma_1-\sigma_2)\upsilon^4\rho-3(2\sigma_1-\sigma_2)\upsilon^4=0.\end{aligned} \tag{24}$$

As $\rho=o(\upsilon)$ so ρ can be expressed as

$$\rho=a_1\upsilon+a_2\upsilon^2+a_3\upsilon^3+a_4\upsilon^4+a_5\upsilon^5+a_6\upsilon^6+a_7\upsilon^7+\cdots$$

where $a_1,a_2,a_3,a_4,a_5,a_6,a_7,\cdots$ are small parameters [10], then

$$\begin{aligned}\rho^2&=a_1^2\upsilon^2+2a_1a_2\upsilon^3+\left(a_2^2+2a_1a_3\right)\upsilon^4+2\left(a_1a_4+a_2a_3\right)\upsilon^5\\&\quad+\left(a_3^2+2a_1a_5+2a_2a_4\right)\upsilon^6+2\left(a_2a_5+a_1a_6+a_3a_4\right)\upsilon^7+\cdots,\\\rho^3&=a_1^3\upsilon^3+3a_1^2a_2\upsilon^4+3\left(a_1a_2^2+a_1^2a_3\right)\upsilon^5+\left(a_2^3+3a_1^2a_4+6a_1a_2a_3\right)\upsilon^6\\&\quad+3\left(a_1a_3^2+a_2^2a_3+a_1^2a_5+2a_1a_2a_4\right)\upsilon^7+\cdots,\\\rho^4&=a_1^4\upsilon^4+4a_1^3a_2\upsilon^5+2\left(3a_1^2a_2^2+2a_1^3a_3\right)\upsilon^6+4\left(a_1a_2^3+a_1^3a_4+3a_1^2a_2a_3\right)\upsilon^7+\cdots,\\\rho^5&=a_1^5\upsilon^5+5a_1^4a_2\upsilon^6+5\left(2a_1^3a_2^2+a_1^4a_3\right)\upsilon^7+\cdots,\\\rho^6&=a_1^6\upsilon^6+6a_1^5a_2\upsilon^7+\cdots,\\\rho^7&=a_1^7\upsilon^7+\cdots.\end{aligned} \tag{25}$$

Using above quantities of Equation (25) and $\mu = \upsilon^4$ in Equation (24) and equating the coefficients of different powers of υ to zero, we get the values of small parameters as

$$a_1 = \left[\frac{3(2\sigma_1 - \sigma_2)}{2\left(\frac{\alpha^2}{4} + \omega^2 + 1\right)}\right]^{\frac{1}{4}}, \quad a_2 = Q\left[3(2\sigma_1 - \sigma_2) - 2\left(\frac{\alpha^2}{4} + \omega^2\right)a_1^4\right],$$

$$a_3 = -Q\left[3\left(\frac{\alpha^2}{4} + \omega^2\right)a_1^6 - 10\left(\frac{\alpha^2}{4} + \omega^2\right)a_1^5 a_2 + \left\{\left(\frac{\alpha^2}{4} + \omega^2\right) + 1\right\}a_1^2 a_2^2 + \left\{3(2\sigma_1 - \sigma_2) - 1\right\}a_1^2 - 3(2\sigma_1 - \sigma_2)a_2\right],$$

$$a_4 = Q\left[3(2\sigma_1 - \sigma_2)a_3 - \left(\frac{\alpha^2}{4} + \omega^2\right)a_1^7 - 3\left(\frac{\alpha^2}{4} + \omega^2\right)a_1^5 a_2 - 20\left(\frac{\alpha^2}{4} + \omega^2\right)\left(2a_1^3 a_2^2 + a_1^4 a_3\right) - 2a_1^3 + \left\{3(2\sigma_1 - \sigma_2) - 2\right\}a_1 a_2 - 4\left\{\left(\frac{\alpha^2}{4} + \omega^2\right) + 1\right\}\left(a_1 a_2^3 + 3a_1^2 a_2 a_3\right)\right], \tag{26}$$

$a_5, a_6, a_7, \cdots$ and so on,

where $Q = \dfrac{1}{4a_1^2\left[\left(\frac{\alpha^2}{4} + \omega^2\right) + 1\right]}$.

Therefore the first coordinate of the first libration point $L_1(\xi_1, 0, 0)$ is given by

$$\begin{aligned}\xi_1 &= \mu - 1 - \rho \\ &= \mu - 1 - \left(a_1\upsilon + a_2\upsilon^2 + a_3\upsilon^3 + a_4\upsilon^4 + a_5\upsilon^5 + a_6\upsilon^6 + \cdots\right) \\ &= \mu - 1 - \left\{a_1\sqrt{\mu} + a_2\left(\sqrt{\mu}\right)^2 + a_3\left(\sqrt{\mu}\right)^3 + a_4\left(\sqrt{\mu}\right)^4 + a_5\left(\sqrt{\mu}\right)^5 + a_6\left(\sqrt{\mu}\right)^6 + \cdots\right\},\end{aligned}$$

$$\xi_1 = \mu - 1 - \sum_{n=1}^{\infty} a_n\left(\sqrt{\mu}\right)^n. \tag{27}$$

Here ξ_1 depends upon the mass parameter μ of the primaries, the small parameters $a_1, a_2, a_3, \cdots$, mass variation parameter α, angular velocity ω and triaxiality parameters σ_1 and σ_2. It is to be noted that each small parameters a_n depends upon the preceeding small parameters $a_1, a_2, a_3, \cdots, a_{n-1}$ and other parameters like $\alpha, \omega, \sigma_1, \sigma_2$ etc. *i.e.*, $a_n = f_n\left(a_1, a_2, \cdots, a_{n-1}, \alpha, \omega, \sigma_1, \sigma_2\right)$.

Thus from Equation (27), it is clear that in the classical case the coordinate of libration point L_1 depends upon the mass parameter μ only but under perturbation it depends upon the parameters μ as well as $a_{i's}, \alpha, \omega, \sigma_1, \sigma_2$.

Let $L_2(\xi_2, 0, 0)$ be the second collinear libration point between the two primaries P_1 and P_2 then $\mu - 1 < \xi_2 < \mu$.

$$\Rightarrow \xi_2 - \mu + 1 > 0 \text{ and } \xi_2 - \mu < 0.$$

$$\Rightarrow \left|\xi_2 - \mu + 1\right| = \xi_2 - \mu + 1 \text{ and } \left|\xi_2 - \mu\right| = -\left(\xi_2 - \mu\right).$$

Thus from Equation (18), we have

$$\left(\frac{\alpha^2}{4}+\omega^2\right)\xi_2-\frac{1-\mu}{\left(\xi_2-\mu\right)^2}-\frac{\mu}{\left(\xi_2-\mu+1\right)^2}+\frac{3\mu\left(2\sigma_1-\sigma_2\right)}{2\left(\xi_2-\mu+1\right)^4}=0. \tag{28}$$

Since $\xi_2>\mu-1$ hence let $\xi_2=\mu-1+\rho$, thus $\xi_2-\mu=-1+\rho$, ρ is a very small quantity so it can be chosen as some order of μ.

In terms of ρ, the Equation (28) can be written as

$$\left(\frac{\alpha^2}{4}+\omega^2\right)\left(\mu-1+\rho\right)-\frac{1-\mu}{\left(\rho-1\right)^2}-\frac{\mu}{\rho^2}+\frac{3\mu\left(2\sigma_1-\sigma_2\right)}{2\rho^4}=0,$$

$$\begin{aligned}&2\left(\frac{\alpha^2}{4}+\omega^2\right)\left(\mu-1+\rho\right)\rho^4\left(\rho-1\right)^2-2\left(1-\mu\right)\rho^4-2\mu\rho^2\left(\rho-1\right)^2\\&+3\mu\left(2\sigma_1-\sigma_2\right)\left(\rho-1\right)^2=0,\end{aligned} \tag{29}$$

$$\begin{aligned}&2\left(\frac{\alpha^2}{4}+\omega^2\right)\rho^7-2\left(\frac{\alpha^2}{4}+\omega^2\right)\left(3-\mu\right)\rho^6+2\left(\frac{\alpha^2}{4}+\omega^2\right)\left(4-2\mu\right)\rho^5\\&-2\left\{1-\left(\frac{\alpha^2}{4}+\omega^2\right)\left(1-\mu\right)\right\}\rho^4+4\mu\rho^3+\mu\left\{3\mu\left(2\sigma_1-\sigma_2\right)-2\right\}\rho^2\\&-6\mu\left(2\sigma_1-\sigma_2\right)\rho+3\mu\left(2\sigma_1-\sigma_2\right)=0.\end{aligned} \tag{30}$$

The Equation (30) is a seven degree polynomial equation in ρ, so there are seven values of ρ in Equation (30).

If we put $\mu=0$ in Equation (30), we get

$$2\left(\frac{\alpha^2}{4}+\omega^2\right)\rho^7-6\left(\frac{\alpha^2}{4}+\omega^2\right)\rho^6+8\left(\frac{\alpha^2}{4}+\omega^2\right)\rho^5-2\left\{1-\left(\frac{\alpha^2}{4}+\omega^2\right)\right\}\rho^4=0. \tag{31}$$

Here also $\rho^4=0$ gives four roots of Equation (31) for $\mu=0$, so as earlier case let

$$\rho=b_1\upsilon+b_2\upsilon^2+b_3\upsilon^3+b_4\upsilon^4+b_5\upsilon^5+b_6\upsilon^6+b_7\upsilon^7+\cdots,$$

where $b_1,b_2,b_3,b_4,b_5,b_6,b_7,\cdots$ are small parameters.

Putting the values of $\rho^1,\rho^2,\rho^3,\rho^4$ and $\mu=\upsilon^4$ in Equation (29) and equating the coefficients of different powers of υ, we get

$$b_1=-\left[\frac{3\left(2\sigma_1-\sigma_2\right)}{2\left(\frac{\alpha^2}{4}+\omega^2\right)}\right]^{\frac{1}{4}},$$

$$b_2=S\left[6b_1\left(2\sigma_1-\sigma_2\right)-8b_1^5\left(\frac{\alpha^2}{4}+\omega^2\right)\right],$$

$$b_3=S\left[\left(\frac{\alpha^2}{4}+\omega^2\right)\left(6b_1^6-40b_1^4b_2-12b_1^2b_2^2\right)+12b_1^2b_2^2+6b_2\left(2\sigma_1-\sigma_2\right)\right],$$

$$b_4=S\left[\left(\frac{\alpha^2}{4}+\omega^2\right)\left\{36b_1^5b_2-2b_1^7-40\left(2b_1^3b_2^2+b_1^4b_3\right)-8b_1b_2^3-24b_1^2b_2b_3\right\}\right.$$

$$+8b_1b_2^3+24b_1^2b_2b_3+4b_1-4b_1b_2-6b_3\left(2\sigma_1-\sigma_2\right)\Big],$$

b_5, b_6, b_7 and so on,

where $S=\dfrac{1}{b_1^3\left[\left(\dfrac{\alpha^2}{4}+\omega^2\right)-1\right]}$.

Similar to Equation (27), the coordinates of the Second libration point is given by

$$\xi_2=\mu-1+b_1\upsilon+b_2\upsilon^2+b_3\upsilon^3+b_4\upsilon^4+b_5\upsilon^5+b_6\upsilon^6+b_7\upsilon^7+\cdots$$
$$=\mu-1+b_1\mu^{\frac{1}{4}}+b_2\mu^{\frac{1}{2}}+b_3\mu^{\frac{3}{4}}+b_4\mu^{1}+b_5\mu^{\frac{5}{4}}+b_6\mu^{\frac{3}{2}}+\cdots$$

$$\xi_2=\mu-1+\sum_{n=1}^{\infty}b_i\mu^{\frac{n}{4}}. \tag{32}$$

Let $L_3\left(\xi_3,0,0\right)$ be the third libration point right to the First primary, then

$$\xi_3>\xi_2=\mu-1-\rho \;\Rightarrow \xi_3>\mu-1+\rho$$

Let $\xi_3=\mu-1+2\rho$ then $\xi_3-\mu=2\rho-1$ and $\xi_3-\mu+1=2\rho$.

Thus from Equation (18), we have

$$\left(\frac{\alpha^2}{4}+\omega^2\right)\left(\mu-1+2\rho\right)-\frac{1-\mu}{\left(2\rho-1\right)^2}-\frac{\mu}{\left(2\rho\right)^2}+\frac{3\mu\left(2\sigma_1-\sigma_2\right)}{2\left(2\rho\right)^4}=0,$$

$$2\left(\frac{\alpha^2}{4}+\omega^2\right)\left(2\rho-1+\mu\right)\left(2\rho-1\right)^2\left(2\rho\right)^4-2\left(1-\mu\right)\left(2\rho\right)^4-8\mu\rho^2\left(2\rho-1\right)^2 \tag{33}$$
$$+3\mu\left(2\sigma_1-\sigma_2\right)\left(2\rho-1\right)^2=0.$$

when $\mu=0$, then Equation (33) reduced to

$$32\left(\frac{\alpha^2}{4}+\omega^2\right)\left(2\rho-1\right)^3\rho^4-32\rho^4=0.$$

As in Equation (33) let $\rho=c_1\upsilon+c_2\upsilon^2+c_3\upsilon^3+c_4\upsilon^4+\cdots$, whereas c_1, c_2, c_3 are small parameters. Thus Equation (30) reduced to

$$8\left(\alpha^2+4\omega^2\right)\left(2\rho-1+\upsilon^4\right)\left(2\rho-1\right)^2\rho^4-32\left(1-\upsilon^4\right)\rho^4-8\upsilon^4\rho^2\left(2\rho-1\right)^2$$
$$-3\upsilon^4\left(2\sigma_1-\sigma_2\right)\left(2\rho-1\right)^2=0.$$

By putting values of $\rho, \rho^2, \rho^3, \rho^4, \rho^5, \rho^6, \rho^7, \cdots$ and $\mu=\upsilon^4$ in Equation (33) and equating the coefficients of different powers of υ, we get

$$c_1=\left[\frac{3\left(2\sigma_1-\sigma_2\right)}{8\left(\alpha^2+4\omega^2+4\right)}\right]^{\frac{1}{4}},$$

$$c_2=T\left[12\left(2\sigma_1-\sigma_2\right)c_1-48\left(\alpha^2+4\omega^2\right)c_1^5\right],$$

$$c_3=T\Big[\left(\alpha^2+4\omega^2\right)\left(240c_1^4c_2-96c_1^6\right)-48\left(\alpha^2+4\omega^2+4\right)c_1^2c_2$$
$$-12\left(2\sigma_1-\sigma_2\right)\left(c_1^2-c_2\right)-8c_1^2\Big],$$

$$c_4 = T\Big[\left(\alpha^2+4\omega^2\right)\left\{64c_1^7 - 576c_1^5c_2 + 240\left(2c_1^3c_2^2 + c_1^4c_3\right)\right\}$$
$$-32\left(\alpha^2+4\omega^2+4\right)\left(c_1c_2^3 + 3c_1^2c_2c_3\right)$$
$$+32c_1^3 - 16c_1c_2 + 12\left(2\sigma_1-\sigma_2\right)\left(2c_1c_2-1\right)\Big],$$

and so on $\cdots$,

where $T = \dfrac{1}{32\left(\alpha^2+4\omega^2+4\right)c_1^3}$.

Similar to Equation (27), the coordinates of the third libration point is given by

$$\xi_3 = \mu - 1 + 2\sum_{n=1}^{\infty} c_n \upsilon^n = \mu - 1 + 2\sum_{n=1}^{\infty} c_n \mu^{\frac{n}{4}}. \tag{34}$$

5. Triangular Libration Points

For triangular libration points, $x \neq 0, y \neq 0$ and $z = 0$ then from the system (17) we have

$$\left(\frac{\alpha^2}{4}+\omega^2\right)x - \frac{(1-\mu)(x-\mu)}{\rho_1^3} - \frac{\mu(x-\mu+1)}{\rho_2^3} + \frac{3\mu\left(2\sigma_1-\sigma_2\right)(x-\mu+1)}{2\rho_2^5}$$
$$+\frac{15\mu(x-\mu+1)}{2\rho_2^7} = 0, \tag{35}$$

$$\left(\frac{\alpha^2}{4}+\omega^2\right) - \frac{(1-\mu)}{\rho_1^3} - \frac{\mu}{\rho_2^3} + \frac{3\mu\left(2\sigma_1-\sigma_2\right)}{2\rho_2^5} + \frac{15\mu\left(2\sigma_1-\sigma_2\right)y^2}{2\rho_2^7} = 0, \tag{36}$$

where from Equation (2)

$$\rho_1^2 = (x-\mu)^2 + y^2 \text{ and } \rho_2^2 = (x-\mu+1)^2 + y^2. \tag{37}$$

Now Equation (35) $-(x-\mu+1)\times$ Equation (36) gives

$$\frac{1}{\rho_1^3} = \frac{\alpha^2}{4} + \omega^2 \tag{38}$$

and Equation (35) $-(x-\mu)\times$ Equation (36) gives

$$\frac{1}{\rho_2^3} = \frac{\alpha^2}{4} + \omega^2 + \frac{3\left(2\sigma_1-\sigma_2\right)}{2\rho_2^5} + \frac{15\left(\sigma_1-\sigma_2\right)y^2}{2\rho_2^7}. \tag{39}$$

For the first approximation, suppose $\sigma_1 = \sigma_2 = 0$, then $\omega^2 = 1$ and from Equation (38) and Equation (39), we get

$$\frac{1}{\rho_1^3} = \frac{1}{\rho_2^3} = 1 + \frac{\alpha^2}{4}, \text{ i.e., } \rho_1 = \rho_2 = 1 - \frac{\alpha^2}{12} \quad (\alpha \ll 1).$$

For better approximation let $\sigma_1 \neq 0, \sigma_2 \neq 0$, then the above solutions can be written as

$$\rho_1 = 1 - \frac{\alpha^2}{12} + \alpha_1 \text{ and } \rho_2 = 1 - \frac{\alpha^2}{12} + \alpha_2$$

where $0 < \alpha_1, \alpha_2 \ll 1$.

From Equation (37) $\rho_2^2-\rho_1^2=2(x-\mu)+1$,

$$i.e.,\ x=\mu-\frac{1}{2}+\alpha_1-\alpha_1. \tag{40}$$

Also from the first equation of (37), we have

$$\rho_1^2=(x-\mu)^2+y^2,\quad \text{i.e. } y^2=\frac{3}{4}+\alpha_1+\alpha_2-\frac{\alpha^2}{6},$$

$$\text{and } y=\pm\frac{\sqrt{3}}{2}\left[1+\frac{2}{3}(\alpha_1+\alpha_2)-\frac{\alpha^2}{9}\right].$$

From Equation (37), we have

$$\frac{1}{\rho_1^3}=\frac{\alpha^2}{4}+\omega^2\Rightarrow\alpha_1=\frac{1-\omega^2}{3}.$$

So from Equation (38) and Equation (39), we get

$$\left(\frac{\alpha^2}{2}+2\omega^2\right)\rho_2^7-2\rho_2^4+3(2\sigma_1-\sigma_2)\rho_2^2+15(\sigma_1-\sigma_2)y^2=0,$$

$$\left(\frac{\alpha^2}{2}+2\omega^2\right)\rho_2^7-2\rho_2^4+3(2\sigma_1-\sigma_2)\rho_2^2+15(\sigma_1-\sigma_2)\left(\frac{3}{4}+\alpha_1+\alpha_2-\frac{\alpha^2}{6}\right)=0.$$

Neglecting higher order terms and coupling terms of α_1,α_2, we have

$$\alpha_1=-\frac{1}{3}(2\sigma_1-\sigma_2),$$

$$\alpha_2=\left(\frac{2-\frac{7}{3}\alpha^2-\frac{93}{4}\sigma_1+\frac{69}{4}\sigma_2}{\frac{7}{2}\alpha^2+6+69\sigma_1-42\sigma_2}\right).$$

Thus

$$L_{4,5}=\left[\mu-\frac{1}{2}+\frac{2-\frac{7}{3}\alpha^2-\frac{93}{4}\sigma_1+\frac{69}{4}\sigma_2}{\frac{7}{2}\alpha^2+6+69\sigma_1-42\sigma_2}+\frac{1}{2}(2\sigma_1-\sigma_2),\right.$$

$$\left.\pm\frac{\sqrt{3}}{2}\left\{1+\frac{2}{3}\left(\frac{2-\frac{7}{3}\alpha^2-\frac{93}{4}\sigma_1+\frac{69}{4}\sigma_2}{\frac{7}{2}\alpha^2+6+69\sigma_1-42\sigma_2}\right)-\frac{1}{2}(2\sigma_1-\sigma_2)\right\}\right]$$

are the triangular libration points.

6. Discussions and Conclusion

We have studied the existence of coplanar libration points in the restricted three-body problem with variable mass and smaller primary as a triaxial rigid body as shown in Figure 1. By taking the mass ratio $\mu=0.019$ and the mass variation parameter $\alpha=0.1$ as the fixed quantities, the variation of mass reduction factor γ of the infinitesimal body is taken into consideration and studied the effect of γ on the existence of coplanar libration points.

In Figure 2, the classical case has been discussed for $\alpha=0,\gamma=1,\sigma_1=0,\sigma_2=0$

in which all the five libration points exist. The triangular libration points L_4 and L_5 form equilateral triangle with the primaries. In Figure 3, taking perturbing parameters $\alpha = 0, \gamma = 1, \sigma_1 = 0.1, \sigma_2 = 0.01$, then only three collinear libration points L_1, L_2, L_3 exist and no triangular points exist. The libration points L_1 and L_2 are located at the extreme points of the loop of the lamniscate shaped oval and this oval is again enveloped by a bigger loop. This development of loops is due to the non-zero values of triaxiality parameters σ_1 and σ_2.

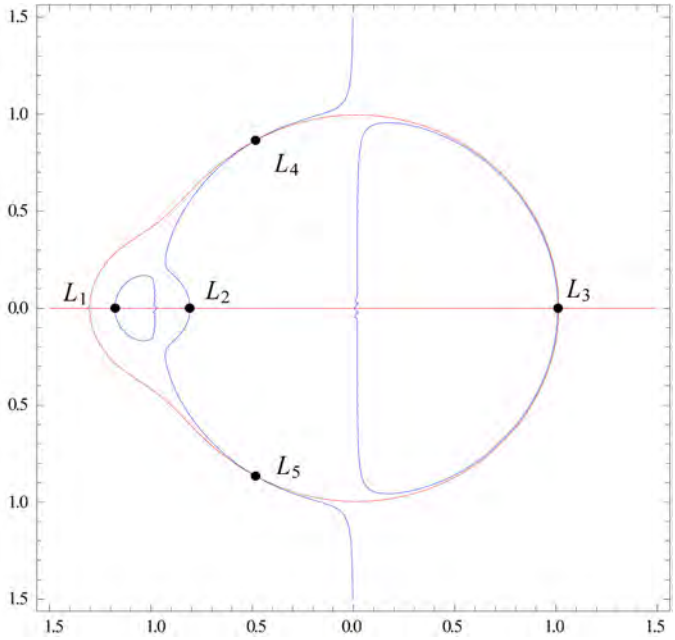

Figure 2. Locations of libration points for $\alpha = 0, \gamma = 1$ (classical case).

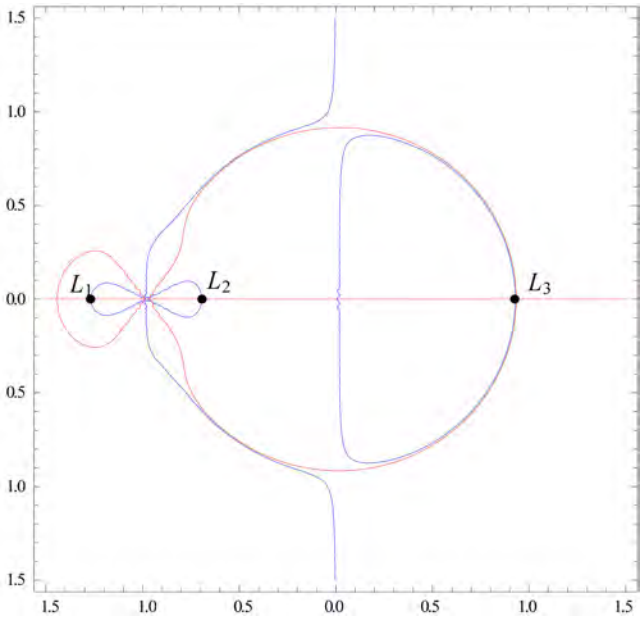

Figure 3. Locations of libration points for $\alpha = 0, \gamma = 1$ (perturbed case).

In **Figure 4**, two collinear libration points L_2 and L_3 exist when $\alpha = 0.1, \gamma = 0.98$ and $\sigma_1 = 0.01, \sigma_2 = 0.1$, which contradicts theoretical evolution of the existence of the five libration points. In **Figure 5**, four coplanar points L_2, L_3, L_4 and L_5 exist for $\alpha = 0.1, \gamma = 0.96, \sigma_1 = 0.1, \sigma_2 = 0.01$ where L_2 and L_3 are collinear and L_4 and L_5 are non-collinear which don't form the equilateral triangle with the primaries. The existence of L_4 and L_5 to the right of the origin is a contradiction to the theoretical evolution of the existence of libration points in the classical case of **Figure 2** (Theory of Orbits [11]).

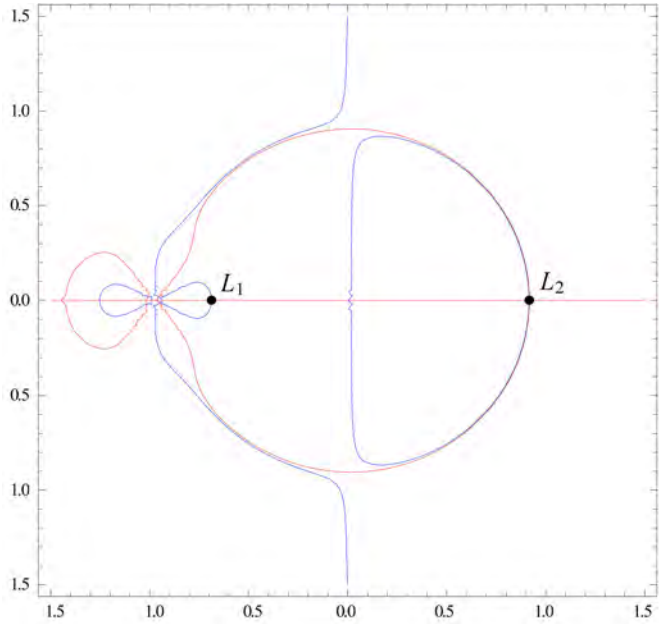

Figure 4. Locations of libration points for $\alpha = 0.1, \gamma = 0.98$ (perturbed case).

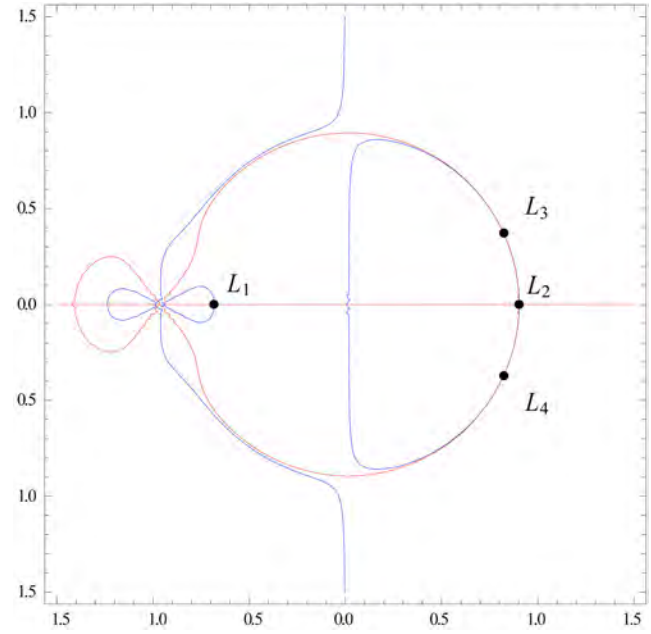

Figure 5. Locations of libration points for $\alpha = 0.1, \gamma = 0.96$ (perturbed case).

In Figure 6, when $\alpha = 0.1, \gamma = 0.94, \sigma_1 = 0.1, \sigma_2 = 0.01$, all the five libration points exist with a difference. In Figure 6, the angular displacement of L_4 and L_5 relative to L_3 is more than that in Figure 5. Further when $\gamma = 0.92$, angular displacement of L_4 and L_5 relative to L_3 is more in Figure 7 than that in Figure 6 and similar case is repeated in Figure 8 for $\gamma = 0.9$. Thus due to the variational parameters α, γ and triaxiality parameters σ_1 and σ_2, the location of triangular libration points L_4 and L_5 has been shifted from left to right and

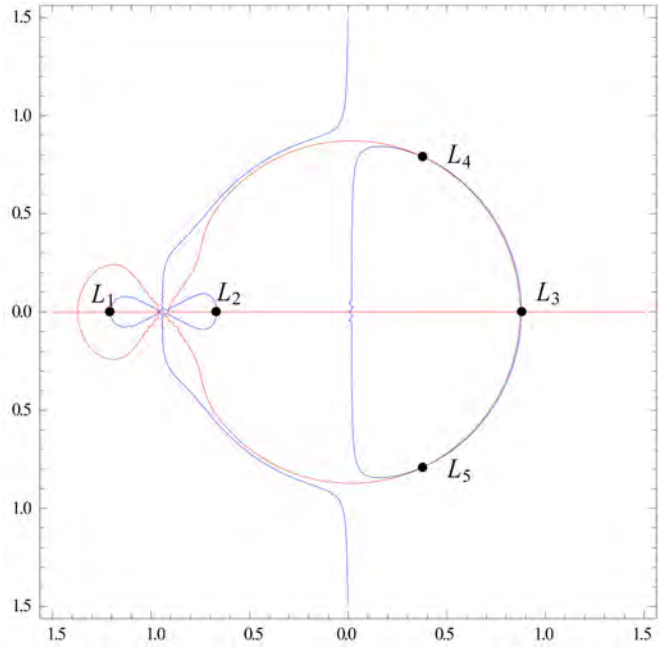

Figure 6. Locations of libration points for $\alpha = 0.1, \gamma = 0.94$ (perturbed case).

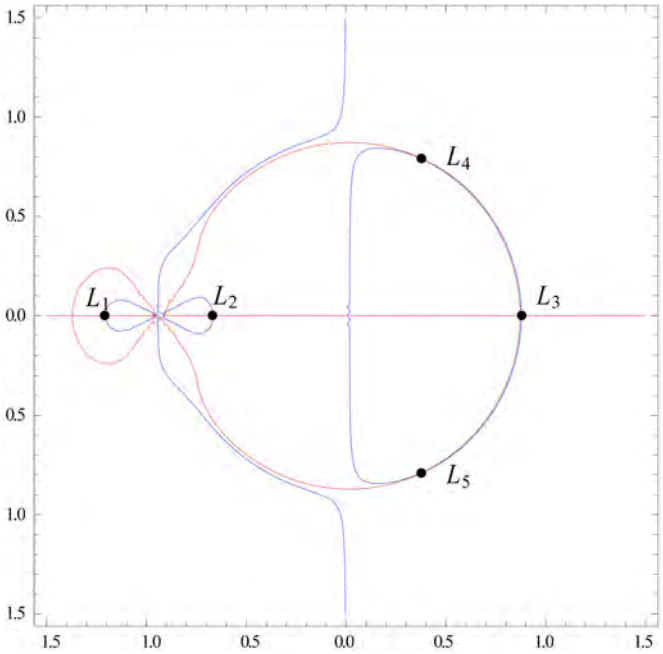

Figure 7. Locations of libration points for $\alpha = 0.1, \gamma = 0.92$ (perturbed case).

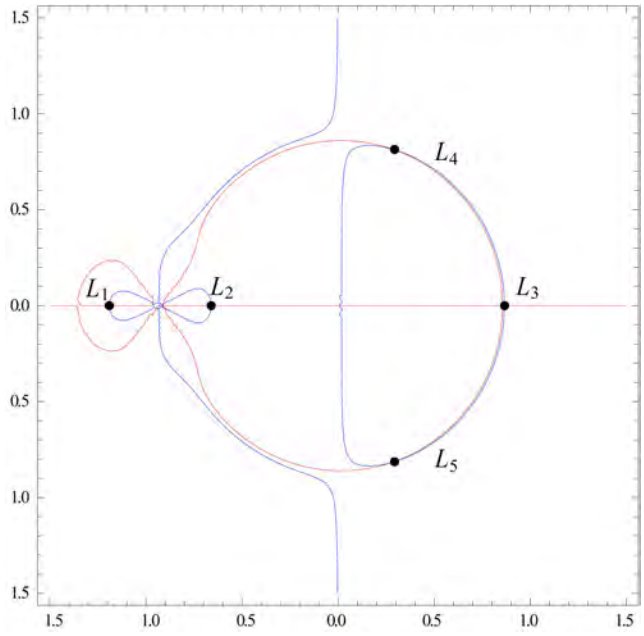

Figure 8. Locations of libration points for $\alpha = 0.1, \gamma = 0.9$ (perturbed case).

the angular distances of L_4 and L_5 relative to L_3 increase with the decrease of γ. From the above discussions, we conclude that for $\alpha = 0.1$ and for $0.94 \le \gamma \le 0.9$, all the five libration points exist with an increase in angular displacement of L_4 and L_5 relative to L_3 with the decrease of γ and shifting of L_4 and L_5 from positive to negative side of the *x*-axis.

Conflicts of Interest

The authors declare no conflicts of interest regarding the publication of this paper.

References

[1] Jeans, J.H. (1928) Astronomy & Cosmogomy. Cambridge University Press, Cambridge.

[2] Meshcherskii, L.V. (1949) Studies on the Mechanics of Bodies of Variable Mass. Gostekhizdat, Moscow.

[3] Shrivastava, A.K. and Ishwar, B. (1983) Equations of Motion of the Restricted Three-Body Problem with Variable Mass. *Celestial Mechanics and Dynamical Astronomy*, **30**, 323-328. https://doi.org/10.1007/BF01232197

[4] Singh, J. and Ishwar, B. (1985) Effect of Perturbations on the Stability of Triangular Points in the Restricted Three-Body Problem with Variable Mass. *Celestial Mechanics and Dynamical Astronomy*, **35**, 201-207. https://doi.org/10.1007/BF01227652

[5] Das, R.K., Shrivastav, A.K. and Ishwar, B. (1988) Equations of Motion of Elliptic Restricted Three-Body Problem with Variable Mass. *Celestial Mechanics and Dynamical Astronomy*, **45**, 387-393. https://doi.org/10.1007/BF01245759

[6] Lukyanov, L.G. (1990) The Stability of the Libration Points in the Restricted Three-Body Problem with Variable Mass. *Astronomical Journal*, **67**, 167-172.

[7] El-Shaboury, S.M. (1990) Equations of Motion of Elliptically-Restricted Problem of a Body with Variable Mass and Two Triaxial Bodies. *Astrophysics and Space Science*, **174**, 291-296. https://doi.org/10.1007/BF00642513

[8] Singh, J. (2008) Non-Linear Stability of Libration Points in the Restricted Three-Body Problem with Variable Mass. *Astrophysics and Space Science*, **314**, 281-289. https://doi.org/10.1007/s10509-008-9768-9

[9] Hassan, M.R., Kumari, S. and Hassan, M.A. (2017) Existence of Libration Points in the R3BP with Variable Mass when the Smaller Is an Oblate Spheroid. *International Journal of Astronomy and Astrophysics*, **7**, 45-61. https://doi.org/10.4236/ijaa.2017.72005

[10] Volosov, V.M. (1972) Introductory Mathematics for Engineers. Mir Publishers, Moscow.

[11] Szebehely, V. (1967) Theory of Orbits—The Restricted Problem of Three Bodies. Academic Press, New York and London.

International Journal of Astronomy and Astrophysics, 2019, 9, 39-50
http://www.scirp.org/journal/ijaa
ISSN Online: 2161-4725
ISSN Print: 2161-4717

Spitzer IRAC Colors of Nebulae Associated with Star-Forming Regions

Yoichi Itoh[1], Yumiko Oasa[2]

[1]Nishi-Harima Astronomical Observatory, Center for Astronomy, University of Hyogo, Sayo, Hyogo, Japan
[2]Faculty of Education, Saitama University, Saitama, Japan
Email: yitoh@nhao.jp

How to cite this paper: Itoh, Y. and Oasa, Y. (2019) *Spitzer* IRAC Colors of Nebulae Associated with Star-Forming Regions. *International Journal of Astronomy and Astrophysics*, **9**, 39-50.
https://doi.org/10.4236/ijaa.2019.91004

Received: January 27, 2019
Accepted: March 4, 2019
Published: March 7, 2019

Abstract

Star-forming regions are often associated with nebulosity. In this study, we investigated infrared diffuse emission in *Spitzer* IRAC images. The infrared nebula L1527 traces outflows emanating from a low-mass protostar. The nebular color is consistent with the color of a stellar photosphere with large extinction. Nebulae around the HII region W5-East are bright in the infrared. These colors are consistent with the model color of dust containing polycyclic aromatic hydrocarbon (PAH). The strength of ultraviolet irradiation of the nebulae and the small dust fraction were deduced from the infrared colors of the nebulae. We found that the edges of the nebulae are irradiated by strong ultraviolet radiation and have abundant small dust. Dust at the surface of the molecular cloud is thought to be destroyed by ultraviolet radiation from an early-type star.

Keywords

Interstellar Medium, Dust, Extinction, HII Regions

1. Introduction

Dust is one of the most fundamental solid materials in the universe. It is ubiquitous, but dust grains have diverse sizes. It is widely believed that small dust is abundant in the interstellar medium. Interstellar extinction increases with decreasing wavelength in the ultraviolet (UV) and optical wavelengths, with a characteristic bump at 2175 Å [1] claimed that this wavelength dependence of the extinction is well reproduced by graphite dust with a power law size distribution between 0.005 and 1 μm in diameter with an exponent of ~−3.5. On the other hand, an overabundance of large dust has been observed in dense regions. [2]

found that the Lupus 3 dark cloud shines in near-infrared wavelengths. They attributed the nebular emission to scattering of starlight by dust. The observed near-infrared color was reproduced by an interstellar dust model with a higher number density for a larger size regime. [3] conducted polarimetric imaging observations of a T Tauri star, UX Tau. With a spatial resolution of 0.1" (14 AU), they detected a strongly polarized circumstellar disk surrounding UX Tau A. It extends to 120 AU with a polarization degree ranging from 1.6% to 66%. The observed azimuthal profile of the polarization degree was not consistent with dust models using Rayleigh scattering or Mie scattering approximations. A thin disk model with nonspherical dust having a diameter of 60 μm reproduced the observed azimuthal profile.

Polycyclic aromatic hydrocarbon (PAH) is a major component of dust. PAH has many broad emission features in the near- and mid-infrared wavelengths. The strength of the PAH features depends on the number of molecules, degree of ionization, and strength of the UV radiation. [4] conducted *Spitzer* Infrared Spectrograph (IRS) observations of NGC 7023, a reflection nebula irradiated by a Herbig Be star, HD 200775. They observed a 72" × 54" region northwest of the exciting star in the slit-scan mode. This region contains a photodissociation region (PDR) and a molecular cloud. They detected PAH emission bands between 5 and 15 μm and fitted them by model spectra to determine the size, charge, composition, and hydrogen adjacency of the dust. The boundary between the PDR and the molecular cloud showed a distinct discontinuity in the PAH characteristics. In the molecular cloud, small, neutral PAHs account for the emission, whereas stable, large, symmetric, and compact PAH cations are abundant in the PDR. They also found enhancement of the 6.2 and 11.0 μm emission close to the exciting star, indicating PAH photodehydrogenation and fragmentation.

The fluxes and shapes of PAH features can be obtained using an infrared spectrograph. However, the two-dimensional distribution of PAHs cannot be obtained except by slit-scan observations or the use of a three-dimensional spectrograph. Instead, we investigate the spatial distribution of PAHs by imaging observations. [5] (hereafter DL07) synthesized the infrared emission spectra of dust heated by starlight. They considered mixtures of amorphous silicate and graphitic dust. Small carbonaceous dust has PAH-like properties. The PAH mass fraction, starlight intensity, and fraction of the dust heated by starlight were parameters in the calculation. The results indicated that small dust has high radiation efficiency at short wavelengths. They presented model emissivities for *Spitzer* Infrared Array Camera (IRAC) and Multiband Imaging Photometer (MIPS) photometry. [6] constructed the spectral energy distributions (SEDs) of 65 galaxies using *Spitzer* IRAC and MIPS photometry and James Clerk Maxwell Telescope Submillimetre Common-User Bolometer Array photometry. They fitted the dust model spectra of DL07 to the SEDs and found that small dust with PAH emission is abundant in galaxies with high metallicity.

We investigate the infrared colors of nebulae irradiated by a nearby star using archival *Spitzer* IRAC data. By comparison with the model colors, we consider the properties of dust in molecular clouds. In this paper, the phrase "small dust" is used for dust with less than 10^3 C atoms, which corresponds to a diameter of ~13 Å, as it is used in DL07.

2. Data

Infrared data were taken from the Spitzer Archive Center. We used the reduced data [post-basic calibrated data (PBCD)] of 3.6 μm images, 4.5 μm images, and 5.8 μm images (PI: Fazio Giovanni). The spatial resolution of the data is about 1.8 arc seconds. We measured the average and standard deviation of the sky region or the HII region adjacent to the nebula and then subtracted the average count from the image. Next, we made three types of mask images. The first mask image was designed to reject low signal-to-noise regions. We made it from the sky-subtracted image by replacing counts more than 10σ above the sky count with one and counts less than 10σ above the sky count to zero. The second mask image was designed for point source rejection. Point sources were identified on the sky-subtracted image by the DAOFIND task in the IRAF software, and the flux of each source was measured by aperture photometry. A mask was created for each source, as a large aperture mask was made for a bright object. The mask regions were set to zero, and the other regions were set to unity. We also made another point source mask image using Sextractor with the SEGMENTATION option in the CHECKIMAGE_TYPE parameter. These three types of mask images were multiplied by the sky-subtracted image so that only diffuse emission appears in the final image.

3. Results

3.1. L1527

We investigate the infrared color of a nebula without PAH emission. L1527 is a reflection nebula associated with the low-mass protostar IRAS 04368 + 2557 in the Taurus molecular cloud. It is seen in edge-on geometry with bipolar outflows toward the east and west. Strong UV radiation is not expected from the central star; thus, PAH is not expected to be excited. **Figure 1** shows the color-color diagram of L1527. We measured the nebular flux of 5 × 5 pixels (3.0" × 3.0") in each band. Error bars in the figure indicate the average values of standard deviations of the 5 × 5 pixel regions. The error may be overestimated because uniform color is assumed in each 5 × 5 pixel region. In the figure, the colors of dwarfs and giants are located around (0, 0) [7]. The nebular colors are plotted along the interstellar extinction vector [8] with the origin at (0, 0) and are around the colors of blackbodies. Those colors are consistent with the colors of Class I and Class II sources [9]. The PAH model (DL07) does not reproduce the color of L1527. We conclude that the nebula L1527 is a reflection nebula and does not contain strong PAH emission features. We also claim that the color-color

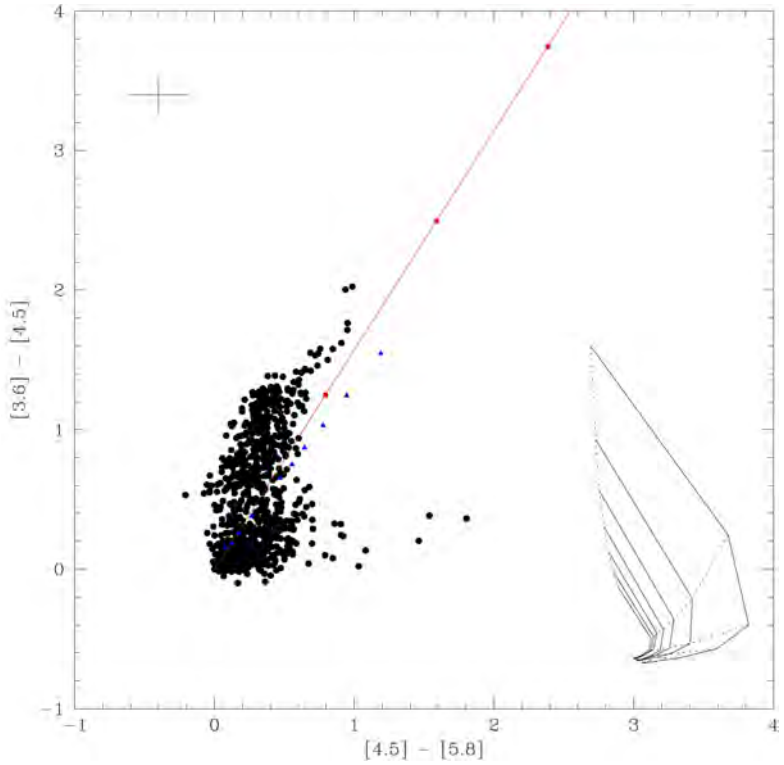

Figure 1. Infrared color of reflection nebula L1527 (filled circles). The nebular colors are measured for every 3.0"× 3.0" region. Stellar photospheres are located close to (0, 0) for any spectral type. A solid red line from the origin indicates the direction of interstellar extinction. Filled red squares correspond to A_V = 100, 200, and 300 mag, respectively. Filled blue triangles show colors of blackbodies with temperatures between 1000 and 500 K. The PAH colors predicted by the model are also shown at bottom right. The color of L1527 is consistent with the colors of Class I and Class II sources.

diagram distinguishes between a reflection nebula and an emission nebula containing PAH features.

From the figure, the amount of extinction is estimated. The photospheric color of the protostar IRAS 04368 + 2557 is assumed to be (0, 0), the same color as dwarfs and giants. We consider that the distance from the points of the nebular color to the line perpendicular to the extinction vector and through the origin corresponds to the extinction in the path from the central star through the nebula to us. Figure 2 shows the extinction map of the nebula L1527. The outflows sweep up the material in the envelope of the protostar, forming a cavity. The wall of the cavity or the residuals in the cavity reflects the light from the central star. Near the central star, the extinction is as large as 150 mag in the V band. The extinction of the eastern outflow is slightly less than that of the western outflow. This estimate is consistent with a near-infrared image showing that the eastern outflow is brighter than the western outflow [10].

3.2. W5-East

W5 is an intensively investigated HII region. It is located at a distance of 2.2 kpc in the Perseus arm and constitutes a chain of molecular clouds with W3 and W4.

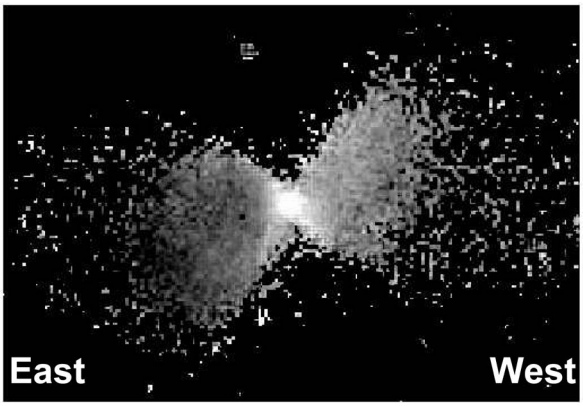

Figure 2. Extinction map of protostar in L1527. The field of view is 179" × 123". A protostar is located at the center of the image. A_V = 20 mag and A_V = 150 mag are shown in black and white, respectively. Near the protostar, the extinction is as large as 150 mag in the *V* band. Outflows are located to the east (left) and west (right) of the central star and sweep up the material in the envelope of the protostar. The extinction of the eastern outflow is slightly less than that of the western outflow. In near-infrared wavelengths, the eastern outflow is brighter than the western outflow.

[11] searched for point sources in this region using *Spitzer* IRAC and MIPS images. They identified 2064 young stellar objects on the basis of their infrared spectral energy distributions. The majority of young stellar objects with infrared excess belong to clusters with more than 10 members.

W5 consists of two circular H II regions, W5-East (W5-E) and W5-West. The ionizing star in W5-E is an O7V star, BD +59˚ 0578. We investigate the diffuse emission of the nebulae in the northeast region of W5-E. In this region, two bright rim clouds (BRCs) have been identified [12]. BRC 13 is classified as a Type B cloud, and BRC 14 is identified as a Type A cloud according to their morphology. It is believed that a BRC evolves from Type A through Type B and then Type C [13]. A cluster of massive young stars, AFGL 4029, is located in BRC 14. [14] revealed sequential formation of low-mass stars in this cluster. **Figure 3** is a pseudo-color map of the northeast region of W5-E. Nebulae facing the HII region are bright in the IRAC 3 bands. We selected several small regions to investigate the nebular color (**Figure 4**). **Figure 5** shows a color-color diagram of the selected regions of W5-E. The colors of the nebulae are not consistent with the color of the photosphere with extinction or with blackbody radiation. The [4.5] - [5.8] colors of the nebulae are redder than the colors of the photosphere and a blackbody.

DL07 calculated the IRAC colors of interstellar dust irradiated by starlight. They considered a mixture of amorphous silicate and graphitic dust. The size distribution of the silicate and graphitic dust follows the power law distributions presented by [15]. In this distribution, the volume ratio of silicate dust to graphite dust is 1.44. In addition, DL07 included two populations of small carbonaceous dust; both follow lognormal distributions with peaks at 4.0 and 20 Å. They constructed seven models of the Milky Way with various mass fraction of small dust ($0.47\% < q < 4.58\%$). Small carbonaceous dust has PAH-like properties.

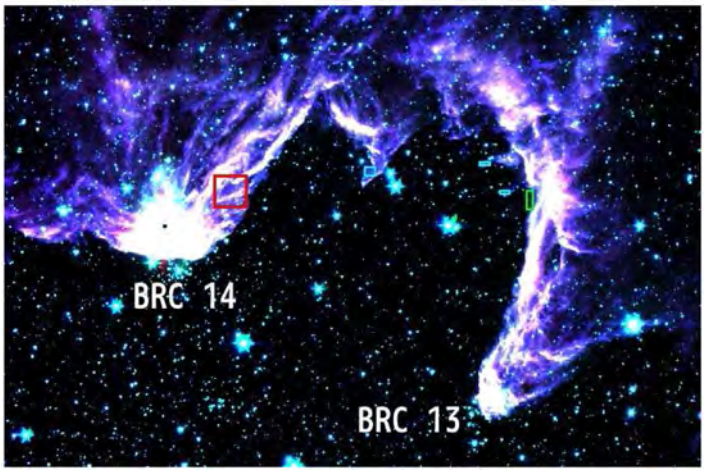

Figure 3. Pseudo-color image of northeast region of W5-E constructed from IRAC 3.6, 4.5, and 5.8 μm images. The field of view is 22.1' × 14.3'. The regions whose colors are discussed on the color-color diagram are indicated by boxes (red: BRC 14, green: bay-like region, blue: B- and C-like BRCs). The exciting star is located outside the frame below the bottom of the figure.

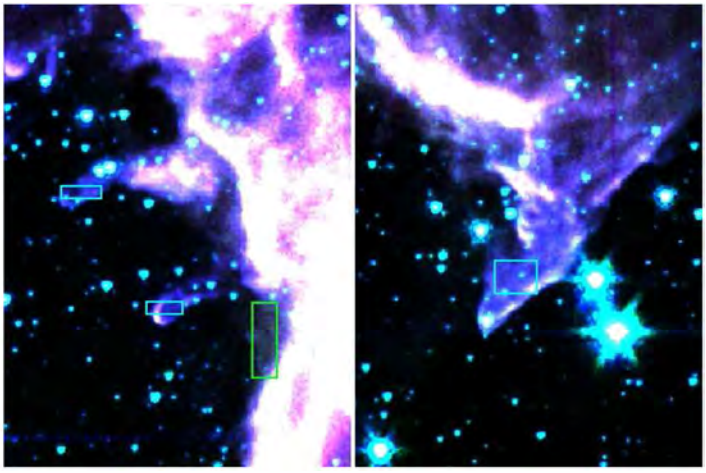

Figure 4. Close-up view of the marked regions in **Figure 3**. The field of view of both images is 2.7' × 3.6'. The bay-like region is indicated by a green box, and B- and C-like BRCs are indicated by blue boxes.

Heating of dust by starlight is considered. Its strength is parameterized by the factors of the interstellar radiation field (U_{ISRF}, [16]). They presented infrared spectra of dust with various mass fractions of small dust and starlight intensities. The vibration modes of PAH produce strong emission features at 3.3, 6.2, 7.6, 8.6, and 11.3 μm. The intensities of these features change with the temperature of the dust. A small dust grain is easily heated by absorption of a few UV photons or a single UV photon and then emits strong PAH features at short wavelengths. Thus, the ratio of the PAH emission feature and the color of specific photometric bands is a function of the fraction of small dust and the intensity of the UV radiation.

The observed colors of the nebulae are consistent with the model colors of

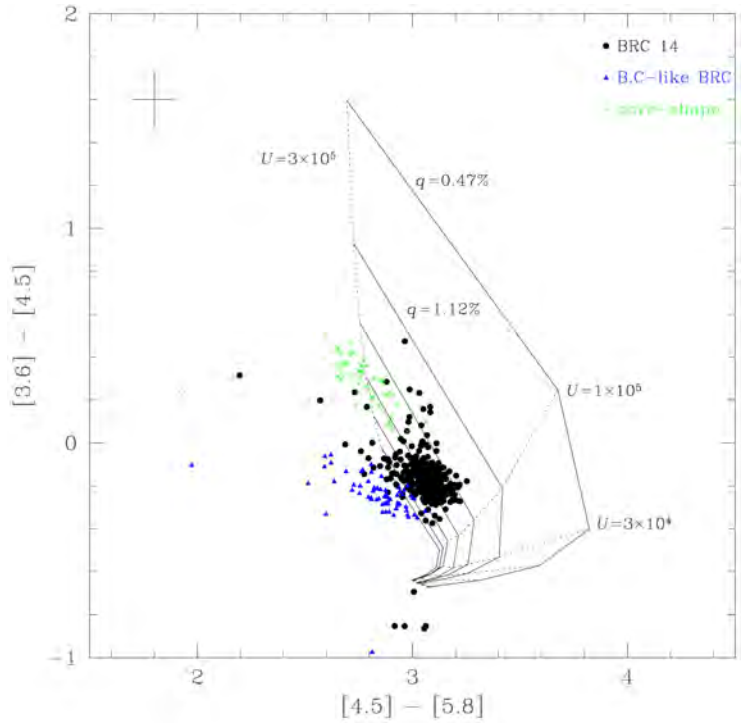

Figure 5. Infrared colors of the marked regions of the nebulae in W5-E. Colors of different nebulae are shown by different symbols. Over plotted are the model color of dust containing PAH. The solid lines show the model colors of various small dust fractions (q = 0.47%, 1.12%, 1.77%, 2.50%, 3.19%, 3.90%, and 4.58%). The nebula containing abundant small dust is bluer. The dotted lines indicate the model colors with various UV radiation levels between 10^2 times and 3×10^5 times the interstellar UV radiation in steps of 0.5 on a logarithmic scale. The nebulae are bright with PAH emission bands.

DL07 (Figure 5). The nebulae are emission nebulae. The colors at different positions in the nebulae are located at different loci in the diagram. The colors of the bay-like region are located at the top-left position representing a part of BRC 14 in the color-color diagram. This indicates that the small dust fraction is small and the UV radiation is strong in the bay-like region compared to those in BRC 14. The colors of the B- and C-like BRCs are located below and to the left of the color of BRC 14 in the diagram. This indicates that the B- and C-like BRCs have an abundant population of small dust irradiated by or a single UV photon and then emits strong PAH features at short wavelengths. Thus, the ratio of the PAH emission feature and the color of specific photometric bands is a function of the fraction of small dust and the intensity of the UV radiation.

The observed colors of the nebulae are consistent with the model colors of DL07 (Figure 5). The nebulae are emission nebulae. The colors at different positions in the nebulae are located at different loci in the diagram. The colors of the bay-like region are located at the top-left position representing a part of BRC 14 in the color-color diagram. This indicates that the small dust fraction is small and the UV radiation is strong in the bay-like region compared to those in BRC 14. The colors of the B- and C-like BRCs are located below and to the left of the color of BRC 14 in the diagram. This indicates that the B- and C-like BRCs have

an abundant population of small dust irradiated by strong UV radiation.

The strength of the UV radiation is estimated from the nebular color. We calculated the mean color of 5 × 5 pixel (3.0" × 3.0"). The observed colors of the nebulae are compared with the model color of DL07. The model-calculated PAH fluxes for single UV strengths are up to 3×10^5 times the interstellar value. We excluded a pixel if its observed color did not match the model color of DL07. We also ignored pixels near the bright stars, which are masked in the data reduction procedure. Figure 6 shows the spatial distribution of the UV strength. As expected, the edge of the nebulae facing the HII region show colors indicating strong UV radiation. At the inner part of the nebulae, the colors are consistent with the model color with weak UV radiation. Most of the UV photons from the exciting star are thought to be absorbed and scattered by dust in the molecular cloud. We also estimate the small dust fraction as described above. Figure 7 shows

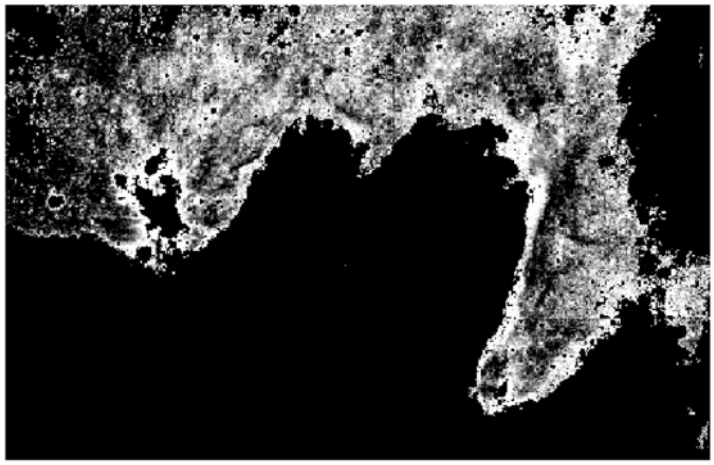

Figure 6. UV irradiation of the nebulae. $\log(U) = 5.15$ mag and $\log(U) = 5.30$ mag are depicted in black and white, respectively. The edge of the nebulae facing the HII region are irradiated by strong UV radiation.

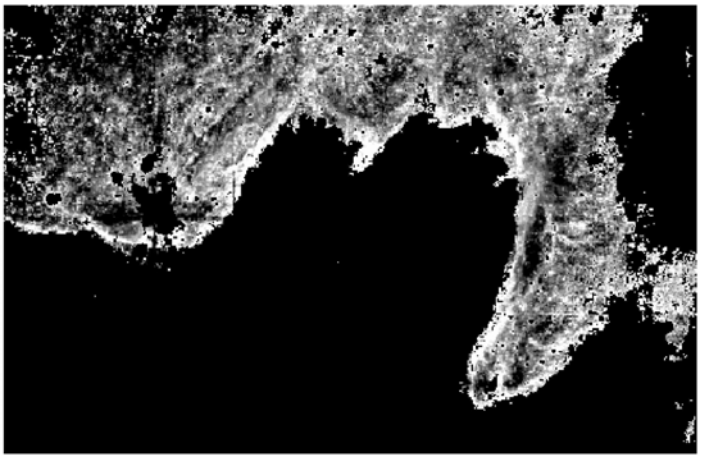

Figure 7. Spatial distribution of small dust fraction. $q = 1.5\%$ mag and $q = 3.0\%$ mag are depicted in black and white, respectively. The map indicates a large small dust fraction at the edge of the nebulae.

the spatial distribution of the small dust fraction in W5-E. The distribution is not uniform in the nebulae. At the inner part of the nebulae, the small dust fraction is small, and at the edge of the nebulae, it is large. This inhomogeneity is especially obvious for BRC 13, a Type B BRC.

The fact that small dust is more abundant at the edge of the nebulae than in the inner part of the nebulae indicates that large dust grains at the surface of the molecular clouds are reduced to small dust grains by UV radiation from the early-type star.

4. Discussion

Our claim that dust grains at the surface of the molecular cloud are destroyed by UV radiation emanating from an early-type star is deduced from the nebular color in the flux-calibrated images. To estimate the precise flux of the nebulae, we subtracted the flux of the HII region adjacent to the nebulae. We examined whether the uncertainty in the flux of the HII region challenges our claim. We added or subtracted a flux representing 5 times the standard deviation of the flux of the HII region and then estimated the strength of the UV radiation and fraction of small dust. Even after we added or subtracted the flux, the claim that small dust is abundant at the surface of the molecular cloud remained valid. Diffuse emission appears even in the HII region (see **Figure 1** of [11]). Even if the UV strength and dust population are estimated using the original PBCD images, the spatial distribution of the dust population does not change; *i.e.*, small dust is abundant at the surface of the molecular cloud.

The overabundance of small dust at the surface of the molecular cloud is deduced from the "blue" infrared colors at the edge of the nebula. Nebulae have different infrared colors not only with different small dust fractions and different UV radiation strengths but also with different amounts of extinction. The blue color at the edge of the nebula is naturally thought to be produced by the low extinction. At the edge of the nebulae, the small dust fraction is as high as 4%, whereas at the inner part of the nebulae, the fraction is as low as 2% and reaches 1.5% locally. The [4.5] - [5.8] color difference between the edge and the region with $q = 1.5\%$ is about 0.2 mag (**Figure 5**). These observations can be reproduced if the inner part of the nebulae has an extinction of 30 mag in the V band. [14] conducted a near-infrared imaging survey of the AFGL 4029 cluster in BRC 14. They detected 605 sources, most of which are classified as background stars. The visual extinction of a star can be estimated from the color difference between the observed color and the intrinsic color of a dwarf or a giant. The color-color diagram of the sources detected in [14] indicated that the largest visual extinction is ~20 mag. The average extinction of the sources in the AFGL 4029 cluster and between the cluster and the bright rim is 7.8 mag in the V band. Thus, the visual extinction does not produce the infrared color difference between the edge and the inner part of the nebula. Note that our line of sight and the incident direction of UV radiation from the early-type star to the molecular cloud are different. Nevertheless, there is no robust evidence that the observed

color difference of the infrared nebula is totally reproduced by the difference in the extinction. We think that the observed color difference is caused, at least partially, by the spatial inhomogeneity of the small dust fraction.

The process of dust destruction has been intensively investigated. [17] claimed that thermal evaporation of dust due to strong radiation from an exciting star is likely to be unimportant even in an HII region. Similar arguments were given in [18]. On the other hand, recent observational studies indicated spatial variation of the physical or chemical state of PAH. [19] observed the M17-Southwest photodissociation region with the *Infrared Space Observatory* Short Wavelength Spectrometer. They found that all the PAH features peak at the boundary of the HII region and the molecular cloud, indicating spatial variation of the PAH abundance. From the flux ratios of the PAH features, they concluded that most of the PAHs are ionized and almost fully hydrogenated in the HII region and at the boundary. [20] constructed a radiative transfer model of ionized hydrogen regions and fitted it to the infrared spectra of the HII region RCW 120. From the spatial variation of the PAH emission features, they concluded that PAHs are destroyed in the ionized region on a timescale of 30 Myr. Observational study of spatially resolved dust size distributions in molecular clouds under different UV environments will conclusively identify the dust destruction process.

5. Conclusions

We investigated the infrared colors of nebulae associated with star-forming regions using *Spitzer* IRAC images.

- The color of the diffuse emission of L1527 is consistent with a photospheric color with large extinction. The central source of the emission is a low-mass protostar, which does not emit strong UV radiation that excites PAHs.
- The nebulae in W5-E facing the HII region are bright in the infrared. Their color is not uniform. A comparison with the model color of small dust emission revealed that the nebulae are bright in PAH emission features. The nebular color indicated that the nebulae facing the HII region are irradiated by strong UV radiation and contain a large population of small dust. We claim that the dust grains at the surface of the molecular cloud are destroyed by UV radiation from an early-type star.

Acknowledgements

We thank the editor and the referee for their comments. This work is based on observations made with the Spitzer Space Telescope, which was operated by the Jet Propulsion Laboratory, California Institute of Technology under a contract with NASA. This work was supported by JSPS KAKENHI Grant Number JP24540231.

Conflicts of Interest

The authors declare no conflicts of interest regarding the publication of this paper.

References

[1] Mathis, J.S., Rumpl, W. and Nordsieck, K.H. (1977) The Size Distribution of Interstellar Grains. *Astrophysical Journal*, **217**, 425-433. https://doi.org/10.1086/155591

[2] Nakajima, Y., *et al.* (2003) Deep Imaging Observations of the Lupus 3 Cloud: Dark Cloud Revealed as Infrared Reflection Nebula. *Astrophysical Journal*, **125**, 1407-1417. https://doi.org/10.1086/367913

[3] Tanii, R., *et al.* (2012) High-Resolution Near-Infrared Polarimetry of a Circumstellar Disk around UX Tau A. *Publ. of Astronomical Society of Japan*, **64**, Article ID: 124. https://doi.org/10.1093/pasj/64.6.124

[4] Boersma, C., Bregman, J.D. and Allamandola, L.J. (2013) Properties of Polycyclic Aromatic Hydrocarbons in the Northwest Photon Dominated Region of NGC 7023. I. PAH Size, Charge, Composition, and Structure Distribution. *Astrophysical Journal*, **769**, Article ID: 117. https://doi.org/10.1088/0004-637X/769/2/117

[5] Draine, B.T. and Li, A. (2007) Infrared Emission from Interstellar Dust. IV. The Silicate-Graphite-PAH Model in the Post-Spitzer Era. *Astrophysical Journal*, **657**, 810-837. https://doi.org/10.1086/511055

[6] Draine, B.T., *et al.* (2007) Dust Masses, PAH Abundances, and Starlight Intensities in the SINGS Galaxy Sample. *Astrophysical Journal*, **663**, 866-894. https://doi.org/10.1086/518306

[7] Megeath, S.T. *et al.* (2004) Initial Results from the Spitzer Young Stellar Cluster Survey. *Astrophysical Journal*, **154**, 367-373. https://doi.org/10.1086/422823

[8] Chapman, N.L. and Mundy, L.G. (2009) Deep JHKs and Spitzer Imaging of Four Isolated Molecular Cloud Cores. *Astrophysical Journal*, **699**, 1866-1882. https://doi.org/10.1088/0004-637X/699/2/1866

[9] Hartmann, L., *et al.* (2005) IRAC Observations of Taurus Pre-Main-Sequence Stars. *Astrophysical Journal*, **629**, 881-896. https://doi.org/10.1086/431472

[10] Tamura, M., *et al.* (1996) Interferometric Observations of Outflows from Low-Mass Protostars in Taurus. *Astrophysical Journal*, **112**. 2076-2085. https://doi.org/10.1086/118164

[11] Koenig, X.P., *et al.* (2008) Clustered and Triggered Star Formation in W5: Observations with Spitzer. *Astrophysical Journal*, **688**, 1142-1158. https://doi.org/10.1086/592322

[12] Sugitani, K., *et al.* (1989) Star formation in Bright-Rimmed Globules—Evidence for Radiation-Driven Implosion. *Astrophysical Journal*, **342**, L87-L90. https://doi.org/10.1007/BFb0119459

[13] Miao, J., *et al.* (2009) An Investigation on the Morphological Evolution of Bright-Rimmed Clouds. *Astrophysical Journal*, **692**, 382-401. https://doi.org/10.1088/0004-637X/692/1/382

[14] Matsuyanagi, I., *et al.* (2006) Sequential Formation of Low-Mass Stars in the BRC 14 Region. *Publications of the Astronomical Society of Japan*, **58**, L29-L34. https://doi.org/10.1093/pasj/58.4.L29

[15] Weingartner, J.C. and Draine, B.T. (2001) Dust Grain-Size Distributions and Extinction in the Milky Way, Large Magellanic Cloud, and Small Magellanic Cloud. *Astrophysical Journal*, **548**, 296-309. https://doi.org/10.1086/318651

[16] Mathis, J.S., Mezger, P.G. and Panagia, N. (1983) Interstellar Radiation Field and Dust Temperatures in the Diffuse Interstellar Matter and in Giant Molecular Clouds. *Astronomy & Astrophysics*, **128**, 212-229.

[17] Salpeter, E.E. (1977) Formation and Destruction of Dust Grains. *Annual Review of Astronomy & Astrophysics*, **15**, 267-293. https://doi.org/10.1146/annurev.aa.15.090177.001411

[18] Draine, B.T. and Salpeter, E.E. (1979) Destruction Mechanisms for Interstellar Dust. *The Astrophysical Journal*, **231**, 438-455.

[19] Verstraete, L., *et al.* (1996) SWS Spectroscopy of Small Grain Features across the M17-Southwest Photo Dissociation Front. *Astronomy & Astrophysics*, **315**, L337-L340.

[20] Pavlyuchenkov, Y.N., Kirsanova, M.S. and Wiebe, D.S. (2013) Infrared Emission and the Destruction of Dust in HII Regions. *Astronomy Reports*, **57**, 573-585. https://doi.org/10.1134/S1063772913070056

International Journal of Astronomy and Astrophysics, 2019, 9, 51-62
http://www.scirp.org/journal/ijaa
ISSN Online: 2161-4725
ISSN Print: 2161-4717

A New Analytical Solution for the Distance Modulus in Flat Cosmology

Lorenzo Zaninetti

Physics Department, via P. Giuria 1, Turin, Italy
Email: zaninetti@ph.unito.it

How to cite this paper: Zaninetti, L. (2019) A New Analytical Solution for the Distance Modulus in Flat Cosmology. *International Journal of Astronomy and Astrophysics*, **9**, 51-62.
https://doi.org/10.4236/ijaa.2019.91005

Received: January 11, 2019
Accepted: March 11, 2019
Published: March 14, 2019

Abstract

A new analytical solution for the luminosity distance in flat ΛCDM cosmology is derived in terms of elliptical integrals of first kind with real argument. The consequent derivation of the distance modulus allows evaluating the Hubble constant, $H_0 = 69.77 \pm 0.33$, $\Omega_M = 0.295 \pm 0.008$ and the cosmological constant, $\Lambda = (1.194 \pm 0.017) \times 10^{-52} \frac{1}{m^2}$.

Keywords

Galaxy Groups, Clusters, and Superclusters, Large Scale Structure of the Universe, Cosmology

1. Introduction

The release of two catalogs for the distance modulus of Supernova (SN) of type Ia, namely, the Union 2.1 compilation, see [1], and the joint light-curve analysis (JLA), see [2], allows matching the observed distance modulus with the theoretical distance modulus of various cosmologies. In this fitting procedure, the cosmological parameters are derived in a scientific and reproducible way.

We now focus our attention on the flat Friedmann-Lemaître-Robertson-Walker (flat-FLRW) cosmology. A first fitting formula has been derived by [3] and an approximate solution in terms of Padé approximant has been introduced by [4]. The presence of the elliptical integrals of the first kind in the integral for the luminosity distance in flat-FLRW cosmology has been noted by [5] [6] [7]. As a practical example the luminosity distance can be expanded into a series of orthonormal functions and the two cosmological parameters turn out to be $H_0 = 70.43 \pm 0.33$ and $\Omega_M = 0.297 \pm 0.002$, see [8]. This paper first introduces in Section 2 a framework useful to build a new solution for the luminosity dis-

tance in flat-FLRW cosmology, which will be derived in Section 3.

2. Preliminaries

This section reviews the adopted statistical framework, the ΛCDM cosmology, and an existing solution for the luminosity distance in flat-FLRW cosmology.

2.1. The Adopted Statistics

In the case of the distance modulus, the merit function χ^2 is

$$\chi^2 = \sum_{i=1}^{N} \left[\frac{(m-M)_i - (m-M)(z_i)_{th}}{\sigma_i} \right]^2, \tag{1}$$

where N is the number of SNs, $(m-M)_i$ is the observed distance modulus evaluated at redshift z_i, σ_i is the error in the observed distance modulus evaluated at z_i, and $(m-M)(z_i)_{th}$ is the theoretical distance modulus evaluated at z_i, see formula (15.5.5) in [9]. The reduced merit function χ^2_{red} is

$$\chi^2_{red} = \chi^2 / NF, \tag{2}$$

where $NF = N - k$ is the number of degrees of freedom, N is the number of SNs, and k is the number of parameters. Another useful statistical parameter is the associated Q-value, which has to be understood as the maximum probability of obtaining a better fitting, see formula (15.2.12) in [9]:

$$Q = 1 - \mathrm{GAMMQ}\left(\frac{N-k}{2}, \frac{\chi^2}{2} \right), \tag{3}$$

where GAMMQ is a subroutine for the incomplete gamma function.

The goodness of the approximation in evaluating a physical variable p is evaluated by the percentage error δ

$$\delta = \frac{\left| p - p_{approx} \right|}{p} \times 100, \tag{4}$$

where p_{approx} is an approximation of p.

2.2. The Standard Cosmology

We follow [10], where the *Hubble distance* D_{H} is defined as

$$D_{\mathrm{H}} \equiv \frac{c}{H_0}. \tag{5}$$

The first parameter is Ω_{M}

$$\Omega_{\mathrm{M}} = \frac{8\pi G \rho_0}{3H_0^2}, \tag{6}$$

where G is the Newtonian gravitational constant and ρ_0 is the mass density at the present time. The second parameter is Ω_{Λ}

$$\Omega_{\Lambda} \equiv \frac{\Lambda c^2}{3H_0^2}, \tag{7}$$

where Λ is the cosmological constant, see [11]. These two parameters are connected with the curvature Ω_K by

$$\Omega_{\mathrm{M}} + \Omega_{\Lambda} + \Omega_K = 1. \tag{8}$$

The comoving distance, D_{C}, is

$$D_{\mathrm{C}} = D_{\mathrm{H}} \int_0^z \frac{\mathrm{d}z'}{E(z')} \tag{9}$$

where $E(z)$ is the "Hubble function"

$$E(z) = \sqrt{\Omega_{\mathrm{M}} (1+z)^3 + \Omega_K (1+z)^2 + \Omega_{\Lambda}}. \tag{10}$$

The above integral does not have an analytical solution but a solution in terms of Padé approximant has been found, see [12].

2.3. A First Formula for a Flat-FLRW Universe

The first model starts from Equation (2.1) in [4] for the luminosity distance, d_{L},

$$d_{\mathrm{L}}(z; c, H_0, \Omega_{\mathrm{M}}) = \frac{c}{H_0}(1+z) \int_{\frac{1}{1+z}}^1 \frac{\mathrm{d}a}{\sqrt{\Omega_{\mathrm{M}} a + (1-\Omega_{\mathrm{M}}) a^4}}, \tag{11}$$

where H_0 is the Hubble constant expressed in km·s^{-1}·Mpc^{-1}, c is the speed of light expressed in km·s^{-1}, z is the redshift and a is the scale-factor. The indefinite integral, $\Phi(a)$, is

$$\Phi(a, \Omega_{\mathrm{M}}) = \int \frac{\mathrm{d}a}{\sqrt{\Omega_{\mathrm{M}} a + (1-\Omega_{\mathrm{M}}) a^4}}. \tag{12}$$

The solution is in terms of F, the Legendre integral or incomplete elliptic integral of the first kind, and is given in [13].

The luminosity distance is

$$d_{\mathrm{L}}(z; c, H_0, \Omega_{\mathrm{M}}) = \Re\left(\frac{c}{H_0}(1+z) \left(\Phi(1) - \Phi\left(\frac{1}{1+z} \right) \right) \right), \tag{13}$$

where $\Re$ means the real part. The distance modulus is

$$(m-M) = 25 + 5\log_{10}\left(d_{\mathrm{L}}(z; c, H_0, \Omega_{\mathrm{M}}) \right). \tag{14}$$

3. A New Formula for a Flat-FLRW Universe

The second model for the flat cosmology starts from Equation (1) for the luminosity distance in [14]

$$d_{\mathrm{L}}(z; c, H_0, \Omega_{\mathrm{M}}) = \frac{c(1+z)}{H_0} \int_0^z \frac{1}{\sqrt{\Omega_{\mathrm{M}} (1+t)^3 + 1 - \Omega_{\mathrm{M}}}} \mathrm{d}t. \tag{15}$$

The above formula can be obtained from formula (9) for the comoving distance inserting $\Omega_K = 0$ and the variable of integration, t, denotes the redshift.

A first change in the parameter Ω_{M} introduces

$$s = \sqrt[3]{\frac{1-\Omega_{\mathrm{M}}}{\Omega_{\mathrm{M}}}} \tag{16}$$

and the luminosity distance becomes

$$d_{\mathrm{L}}\left(z;c,H_0,s\right)=\frac{1}{H_0}c\left(1+z\right)\int_0^z\frac{1}{\sqrt{\frac{\left(1+t\right)^3}{s^3+1}+1-\left(s^3+1\right)^{-1}}}\mathrm{d}t. \tag{17}$$

The following change of variable, $t=\frac{s-u}{u}$, is performed for the luminosity distance which becomes

$$d_{\mathrm{L}}\left(z;c,H_0,s\right)=-\frac{c}{H_0s^2}\left(1+z\right)\left(s^3+1\right)\int_s^{\frac{s}{1+z}}\frac{u}{u^3+1}\sqrt{\frac{s^3\left(u^3+1\right)}{u^3\left(s^3+1\right)}}\mathrm{d}u. \tag{18}$$

Up to now we have followed [14] which continues introducing a new function $T\left(x\right)$; conversely we work directly on the resulting integral for the luminosity distance: which is

$$\begin{aligned}&d_{\mathrm{L}}\left(z;c,H_0,s\right)\\&=-1/3\frac{c\left(1+z\right)3^{3/4}\sqrt{s^3+1}}{\sqrt{s}H_0}\times\left(F\left(2\frac{\sqrt{s\left(s+1+z\right)}\sqrt[4]{3}}{s\sqrt{3}+s+z+1},1/4\sqrt{2}\sqrt{3}+1/4\sqrt{2}\right)\right.\\&\left.-F\left(2\frac{\sqrt[4]{3}\sqrt{s\left(s+1\right)}}{s+1+s\sqrt{3}},1/4\sqrt{2}\sqrt{3}+1/4\sqrt{2}\right)\right),\end{aligned} \tag{19}$$

where s is given by Equation (16) and $F\left(\phi,k\right)$ is Legendre's incomplete elliptic integral of the first kind,

$$F\left(\phi,k\right)=\int_0^{\sin\phi}\frac{\mathrm{d}t}{\sqrt{1-t^2}\sqrt{1-k^2t^2}}, \tag{20}$$

see [15]. The distance modulus is

$$\left(m-M\right)=25+5\log_{10}\left(d_{\mathrm{L}}\left(z;c,H_0,s\right)\right), \tag{21}$$

and therefore

$$\left(m-M\right)=25+5\frac{1}{\ln\left(10\right)}\ln\left(-\frac{1}{3}\frac{c\left(1+z\right)3^{3/4}\left(F_1-F_2\right)\sqrt{s^3+1}}{\sqrt{s}H_0}\right), \tag{22}$$

where

$$F_1=F\left(2\frac{\sqrt{s\left(s+1+z\right)}\sqrt[4]{3}}{s\sqrt{3}+s+z+1},1/4\sqrt{2}\sqrt{3}+1/4\sqrt{2}\right) \tag{23}$$

and

$$F_2=F\left(2\frac{\sqrt[4]{3}\sqrt{s\left(s+1\right)}}{s+1+s\sqrt{3}},1/4\sqrt{2}\sqrt{3}+1/4\sqrt{2}\right), \tag{24}$$

with s as defined by Equation (16).

Data Analysis

In recent years, the extraction of the cosmological parameters from the distance

modulus of SNs has become a common practice, see among others [8] [16] [17]. The best fit to the distance modulus of SNs is here obtained by implementing the Levenberg-Marquardt method (subroutine MRQMIN in [9]). This method requires the fitting function, in our case Equation (22), as well the first derivative $\frac{\partial(m-M)}{\partial H_0}$, which has a simple expression, and the first derivative $\frac{\partial(m-M)}{\partial \Omega_M}$, which has a complicated expression. A simplification can be introduced by imposing a fiducial value for the Hubble constant, namely $H_0 = 70\ \mathrm{km}\cdot\mathrm{s}^{-1}\cdot\mathrm{Mpc}^{-1}$, see [2] [18]. We call this model "flat-FLRW-1", where the "1" stands for there being one parameter. Table 1 presents H_0 and Ω_M for the Union 2.1 compilation of SNs and Figure 1 displays the best fit. The reading of this table allows to evaluate the goodness of the approximation, see (4), in the derivation of the Hubble constant in going from the supposed true value ($H_0 = 70\ \mathrm{km}\cdot\mathrm{s}^{-1}\cdot\mathrm{Mpc}^{-1}$) to the deduced value ($H_0 = 69.77\ \mathrm{km}\cdot\mathrm{s}^{-1}\cdot\mathrm{Mpc}^{-1}$), which is $\delta = 99.67\%$. The

Table 1. Numerical values from the Union 2.1 compilation of χ^2, χ^2_{red} and Q, where k stands for the number of parameters.

Cosmology	SNs	k	parameters	χ^2	χ^2_{red}	Q
flat-FLRW	580	2	$H_0 = 69.77 \pm 0.33$; $\Omega_M = 0.295 \pm 0.008$	562.55	0.9732	0.66
flat-FLRW-1	580	1	$H_0 = 70$; $\Omega_M = 0.295 \pm 0.008$	563.52	0.9732	0.669
ΛCDM	580	3	$H_0 = 69.81$; $\Omega_M = 0.239$; $\Omega_\Lambda = 0.651$	562.61	0.975	0.658

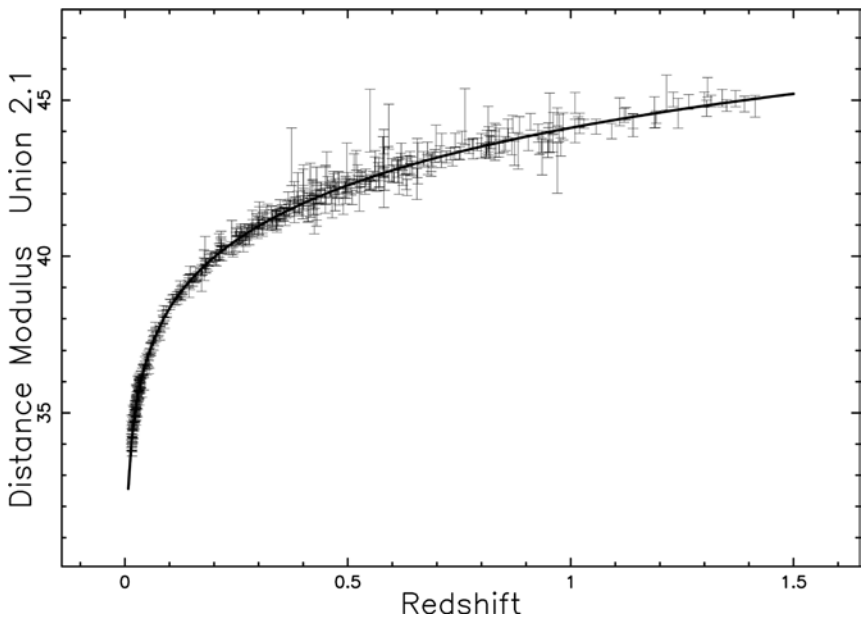

Figure 1. Hubble diagram for the Union 2.1 compilation. The solid line represents the best fit for the exact distance modulus in flat-FLRW cosmology as represented by Equation (22). Parameters as in first line of Table 1; Union 2.1 compilation.

JLA compilation is available at the Strasbourg Astronomical Data Centre (CDS), and consists of 740 type I-a SNs for which we have the heliocentric redshift, z, the apparent magnitude $m_B^\star$ in the B band, the error in $m_B^\star$, $\sigma_{m_B^\star}$, the parameter $X1$, the error in $X1$, σ_{X1}, the parameter C, the error in C, σ_C, and $\log_{10}(M_{stellar})$. The observed distance modulus is defined by Equation (4) in [2]:

$$m - M = -C\beta + X1\alpha - M_b + m_B^\star. \tag{25}$$

The adopted parameters are $\alpha = 0.141$, $\beta = 3.101$ and

$$M_b = \begin{cases} -19.05 & \text{if } M_{stellar} < 10^{10} M_\odot \\ -19.12 & \text{if } M_{stellar} \geq 10^{10} M_\odot \end{cases} \tag{26}$$

see line 1 in Table 10 of [2]. The uncertainty in the observed distance modulus, σ_{m-M}, is found by implementing the error propagation equation (often called the law of errors of Gauss) when the covariant terms are neglected, see Equation (3.14) in [19],

$$\sigma_{m-M} = \sqrt{\alpha^2 \sigma_{X1}^2 + \beta^2 \sigma_C^2 + \sigma_{m_B^\star}^2}. \tag{27}$$

The parameters as derived from the JLA compilation are presented in **Table 2** and the fit is presented in **Figure 2**.

Table 2. Numerical values from the JLA compilation of χ^2, χ^2_{red} and Q, where k stands for the number of parameters.

Cosmology	SNs	k	parameters	χ^2	χ^2_{red}	Q
flat-FLRW	740	2	$H_0 = 69.65 \pm 0.231$; $\Omega_M = 0.3 \pm 0.003$	627.91	0.85	0.998

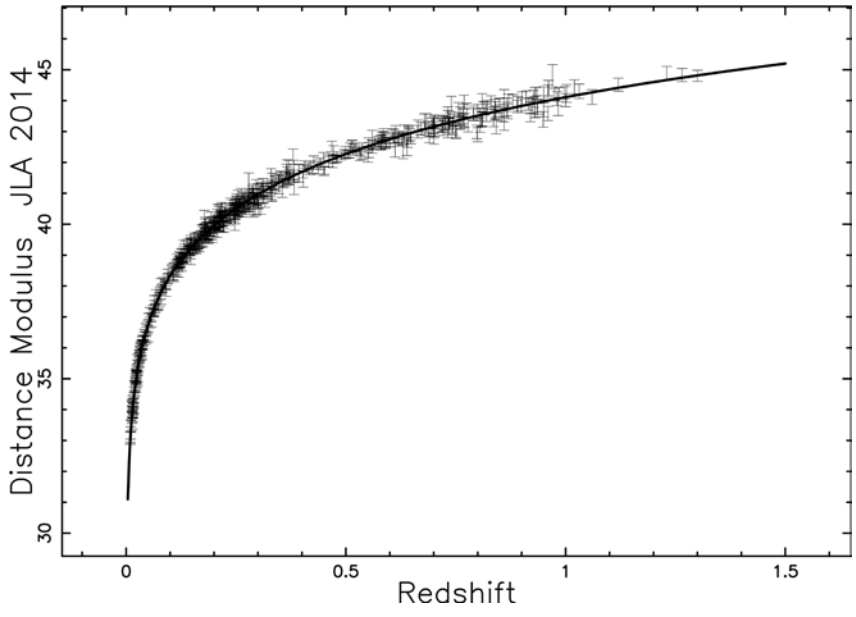

Figure 2. Hubble diagram for the JLA compilation. The solid line represents the best fit for the exact distance modulus in flat-FLRW cosmology as represented by Equation (22). Parameters as in first line of **Table 2**.

As an example the luminosity distance for the Union 2.1 compilation with data as in the first line of Table 1 is

$$d_{\mathrm{L}}(z)=8147.04(1.0+z) \times\left(-0.637664F\left(2.63214\frac{\sqrt{3.1188+1.33542z}}{4.64846+z},0.965925\right)+1.75322\right)\mathrm{Mpc} \tag{28}$$

when $0<z<1.5$

and the distance modulus is

$$m-M=25.0+2.17147\ln\left(8147.04(1.0+z) \times\left(-0.63766F\left(2.6321\frac{\sqrt{3.1188+1.3354z}}{4.6484+z},0.96592\right)+1.7532\right)\right). \tag{29}$$

when $0<z<1.5$

We now derive some approximate results without Legendre integral for the flat-FLRW case and Union 2.1 compilation with data as in Table 1, first line. A Taylor expansion of order 6 around $z=0$ of the luminosity distance as given by Equation (19) for the flat-FLRW case and Union 2.1 compilation gives

$$d_{\mathrm{L}}(z)=0.000423646+4296.57z+3344.13z^2-1186.94z^3+979.403z^4-42078.6z^5\ \mathrm{Mpc} \tag{30}$$

when $0<z<0.197$.

The upper limit in redshift, 0.197, is the value for which the percentage error, see Equation (4), is $\delta=1.16\%$. The asymptotic expansion of the luminosity distance with respect to the variable z to order 5 for the flat-FLRW case and Union 2.1 compilation gives

$$d_{\mathrm{L}}(z)\sim 14283.5z-15802\frac{1}{\sqrt{z^{-1}}}+14283.5-7901.01\sqrt{z^{-1}}+1975.25\left(z^{-1}\right)^{3/2}\ \mathrm{Mpc} \tag{31}$$

when $1.27<z<1.5$.

At the lower limit of $z=1.27$ the percentage error is $\delta=0.54\%$. The two above approximations at low and high redshift have a limited range of existence but does not contain the Legendre integral as solutions (28) and (29) which cover the overall range $0<z<1.5$.

A Taylor expansion of order 6 of the distance modulus as given by Equation (22) around $z=0.1$ for the flat-FLRW case and Union 2.1 compilation gives

$$(m-M)=36.0051+23.1777z-109.604(z-0.1)^2+724.464(z-0.1)^3-5429.06(z-0.1)^4+43429.8(z-0.1)^5 \tag{32}$$

when $0.1<z<0.197$.

The upper limit in redshift, 0.197, is the value at which the percentage error is $\delta=0.14\%$. Figure 3 reports both the numerical and the Taylor expansion of distance modulus in the above range.

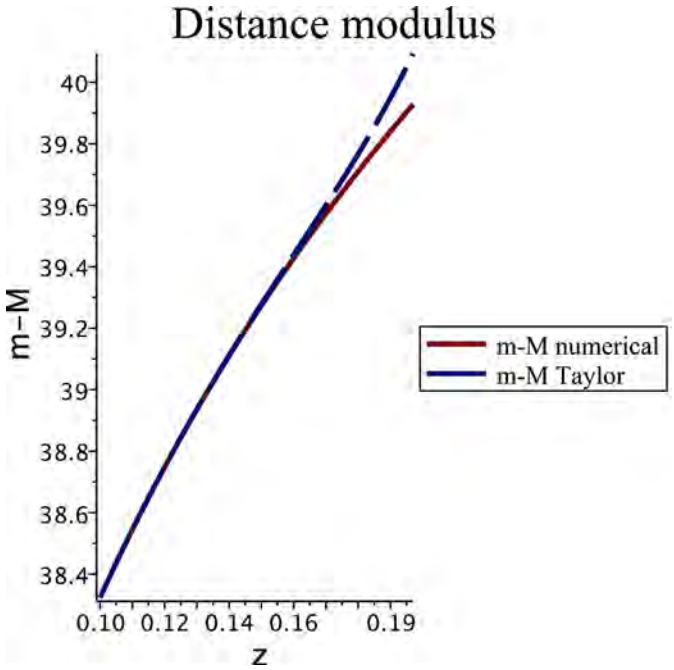

Figure 3. Distance modulus in flat-FLRW cosmology as represented by Equation (22) with parameters as in first line of **Table 1** (full red line) and Taylor solution (dash-dot-dash line) (blue line).

The asymptotic expansion of the distance modulus with respect to the variable z to order 5 for the flat-FLRW case and Union 2.1 compilation gives

$$\begin{aligned}(m-M) \sim & 45.7741+2.17147\ln(z)-2.40231\sqrt{z^{-1}}+0.842625z^{-1} \\ & +0.221081\left(z^{-1}\right)^{3/2}-0.570086z^{-2}-0.150471\left(z^{-1}\right)^{5/2} \\ & +0.357849z^{-3}+0.491842\left(z^{-1}\right)^{7/2}+0.179989z^{-4}\end{aligned} \tag{33}$$

when $1.27 < z < 1.5$.

The lower limit in redshift, 1.27, is the value at which the percentage error is $\delta = 0.54\%$. The ranges of existence in z for the analytical approximations here derived have the percentage error <2%, see Equation (4).

We now introduce the best minimax rational approximation, see [20] [21] [15], of degree (2, 1), for the distance modulus $m_{2,1}(z)$,

$$m_{2,1}(z) = \frac{a+bz+cz^2}{d+ez}. \tag{34}$$

In the case in which the distance modulus is represented by Equation (29) and given the interval $[0.001,1.5]$, the coefficients of the best minimax rational approximation are presented in **Table 3**; the maximum error for the fit is $\approx 2.2\times10^{-5}$. **Figure 4** displays the data and the fit.

4. Conclusions

We have presented an analytical approximation for the luminosity distance in terms of elliptical integrals with real argument. The fit of the distance modulus

Table 3. Maximum error and coefficients of the distance modulus for the best minimax rational approximation for the flat-FLRW case and Union 2.1 compilation. Interval of existence $[0.001,1.5]$.

Name	value
maximum error	$2.28881836 \times 10^{-5}$
a	0.981622279
b	19.6473351
c	1.08210218
d	0.0309164915
e	0.462291896

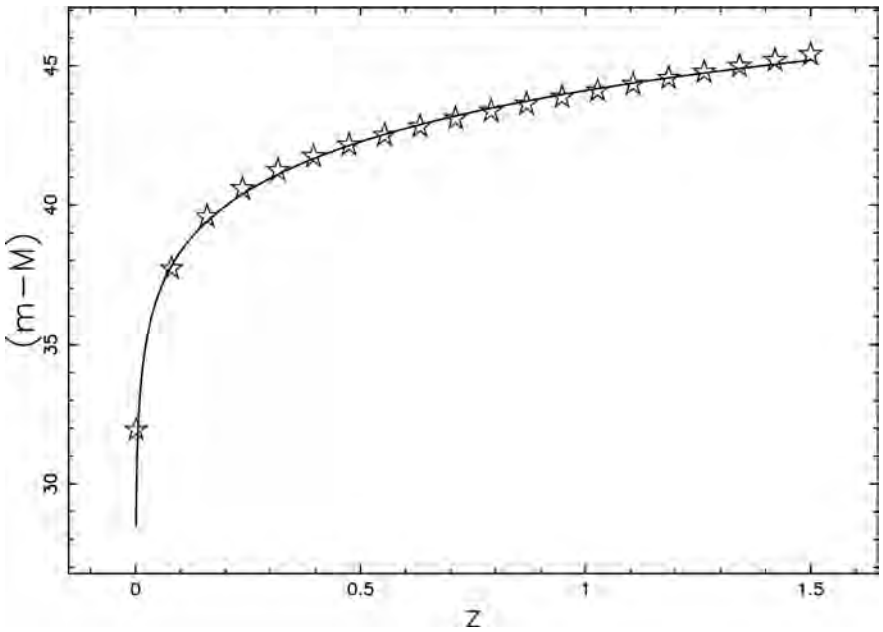

Figure 4. Distance modulus in flat-FLRW cosmology as represented by Equation (22) with parameters as in first line of **Table 1** (full line) and minimax rational approximation (empty stars); Union 2.1 compilation.

of SNs of type Ia allows finding the parameters H_0 and Ω_M for the two compilations in flat-FLRW cosmology

$$H_0 = (69.77 \pm 0.33)\,\mathrm{km \cdot s^{-1} \cdot Mpc^{-1}}, \quad \Omega_M = 0.295 \pm 0.008 \tag{35}$$

flat-FLRW-Union 2.1,

$$H_0 = (69.65 \pm 0.23)\,\mathrm{km \cdot s^{-1} \cdot Mpc^{-1}}, \quad \Omega_M = 0.3 \pm 0.003 \tag{36}$$

flat-FLRW-JLA,

A first comparison with [8] in the case of the Union 2.1 compilation gives a percentage error $p = 0.93\%$ for the derivation of H_0 and $p = 0.67\%$ for the derivation of Ω_M. A second comparison can be done with Equation (13) in [22]

$$H_0 = (67.27 \pm 0.60)\,\mathrm{km \cdot s^{-1} \cdot Mpc^{-1}}, \quad \Omega_M = 0.3166 \pm 0.0084 \tag{37}$$

Planck 2018.

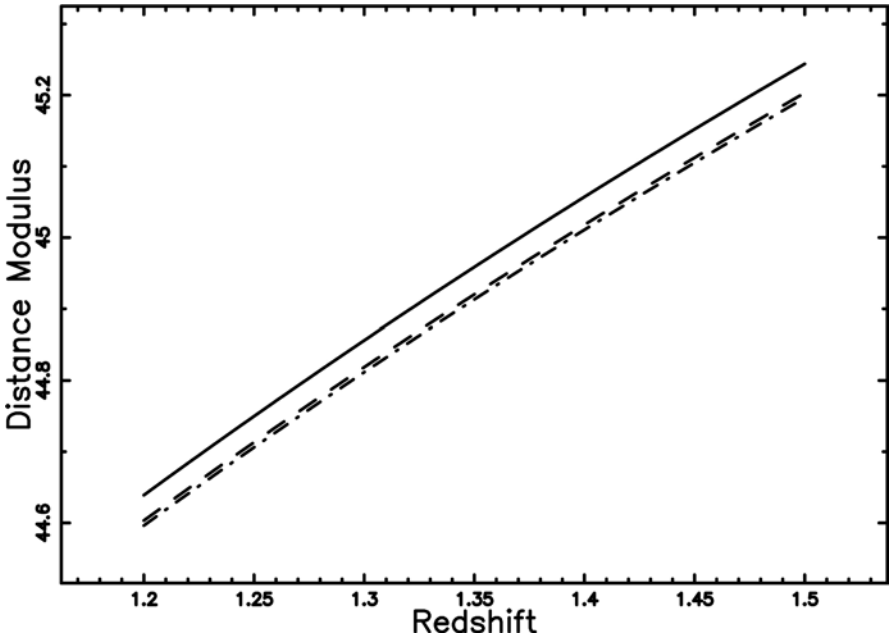

Figure 5. Distance modulus for ΛCDM cosmology (full line), flat-FLRW-1 (dot-dash-dot-dash line) and flat-FLRW cosmology (dashed line). Parameters as in **Table 1** and interval of existence $[1.2,1.5]$.

In the case of the Union 2.1 compilation, the percentage error $p=3.71\%$ for the derivation of H_0 and $p=6.82\%$ for Ω_{M}. A Taylor expansion at low redshift and an asymptotic expansion are presented both for the luminosity distance and the distance modulus. A simple version of the distance modulus is determined through the best minimax rational approximation. Adopting the cosmological parameters found here, the cosmological constant Λ turns out to be, for the Union 2.1 compilation,

$$\Lambda=(1.19457\pm 0.017)\times 10^{-52}\frac{1}{m^2} \tag{38}$$

flat-FLRW Union 2.1,

or introducing $c=1$ and the Planck time, t_p,

$$\Lambda=(3.12046\pm 0.0462942)\times 10^{-122}\frac{1}{t_p^2} \tag{39}$$

flat-FLRW Union 2.1.

The statistical parameters of the fits are given in Table 1 and Table 2 where the other two models are presented. The values of the χ^2 in the above table say that for the Union 2.1 compilation the flat cosmology produces a better fit than the ΛCDM does, but the situation is the reverse for the JLA compilation. As a concluding remark we point out that, thanks to the calibration on the distance modulus of SNs, the differences between the solutions here analyzed are minimum. Therefore a restricted range in redshift should be adopted in order to visualize the diverseness, see Figure 5.

Conflicts of Interest

The author declares no conflicts of interest regarding the publication of this paper.

References

[1] Suzuki, N., Rubin, D., Lidman, C., Aldering, G., Amanullah, R., Barbary, K. and Barrientos, L.F. (2012) The Hubble Space Telescope Cluster Supernova Survey. V. Improving the Dark-Energy Constraints above Z Greater than 1 and Building an Early-Type-Hosted Supernova Sample. *ApJ*, **746**, 85. https://doi.org/10.1088/0004-637X/746/1/85

[2] Betoule, M., Kessler, R., Guy, J. and Mosher, J. (2014) Improved Cosmological Constraints from a Joint Analysis of the SDSS-II and SNLS Supernova Samples. *A&A*, **568**, A22.

[3] Pen, U.L. (1999) Analytical Fit to the Luminosity Distance for Flat Cosmologies with a Cosmological Constant. *ApJS*, **120**, 49. https://doi.org/10.1086/313167

[4] Adachi, M. and Kasai, M. (2012) An Analytical Approximation of the Luminosity Distance in Flat Cosmologies with a Cosmological Constant. *Progress of Theoretical Physics*, **127**, 145. https://doi.org/10.1143/PTP.127.145

[5] Eisenstein, D.J. (1997) An Analytic Expression for the Growth Function in a Flat Universe with a Cosmological Constant. arXiv:astro-ph/9709054

[6] Liu, D.Z., Ma, C., Zhang, T.J. and Yang, Z. (2011) Numerical Strategies of Computing the Luminosity Distance. *MNRAS*, **412**, 2685. https://doi.org/10.1111/j.1365-2966.2010.18101.x

[7] Mészáros, A. and Řpa, J. (2013) A Curious Relation between the Flat Cosmological Model and the Elliptic Integral of the First Kind. *A&A*, **556**, A13 https://doi.org/10.1051/0004-6361/201322088

[8] Benitez-Herrera, S., Ishida, E.E.O., Maturi, M., Hillebrandt, W., Bartelmann, M. and Röpke, F. (2013) Cosmological Parameter Estimation from SN Ia Data: A Model-Independent Approach. *MNRAS*, **436**, 854. https://doi.org/10.1093/mnras/stt1620

[9] Press, W.H., Teukolsky, S.A., Vetterling, W.T. and Flannery, B.P. (1992) Numerical Recipes in FORTRAN. The Art of Scientific Computing. Cambridge University Press, Cambridge.

[10] Hogg, D.W. (1999) Distance Measures in Cosmology. arXiv:astro-ph/9905116

[11] Peebles, P.J.E. (1993) Principles of Physical Cosmology. Princeton University Press, Princeton, NJ.

[12] Zaninetti, L. (2016) Pade Approximant and Minimax Rational Approximation in Standard Cosmology. *Galaxies*, **4**, 4. https://doi.org/10.3390/galaxies4010004

[13] Zaninetti, L. (2016) An Analytical Solution in the Complex Plane for the Luminosity Distance in Flat Cosmology. *Journal of High Energy Physics, Gravitation and Cosmology*, **2**, 581. https://doi.org/10.4236/jhepgc.2016.24050

[14] Baes, M., Camps, P. and Van De Putte, D. (2017) Analytical Expressions and Numerical Evaluation of the Luminosity Distance in a Flat Cosmology. *MNRAS*, **468**, 927.

[15] Olver, F.W.J., Lozier, D.W., Boisvert, R.F. and Clark, C.W. (2010) NIST Handbook of Mathematical Functions. Cambridge University Press, Cambridge.

[16] Gupta, R. (2018) SNe Ia Redshift in a Nonadiabatic Universe. *Universe*, **4**, 104.

[17] Jones, D.O., Scolnic, D.M., Riess, A.G., Rest, A., Kirshner, R.P., Berger, E., Kessler, R., Pan, Y.C., Foley, R.J., Chornock, R., Ortega, C.A., Challis, P.J., Burgett, W.S., Chambers, K.C., Draper, P.W., Flewelling, H., Huber, M.E., Kaiser, N., Kudritzki, R.P., Metcalfe, N., Tonry, J., Wainscoat, R.J., Waters, C., Gall, E.E.E., Kotak, R., McCrum, M., Smartt, S.J. and Smith, K.W. (2018) Measuring Dark Energy Properties with Photometrically Classified Pan-STARRS Supernovae. II. Cosmological Parameters. *The Astrophysical Journal*, **857**, 51.

[18] Ben-Dayan, I., Gasperini, M., Marozzi, G., Nugier, F. and Veneziano, G. (2013) Average and Dispersion of the Luminosity-Redshift Relation in the Concordance Model. *Journal of Cosmology and Astroparticle Physics*, **6**, 2.

[19] Bevington, P.R. and Robinson, D.K. (2003) Data Reduction and Error Analysis for the Physical Sciences. McGraw-Hill, New York.

[20] Remez, E. (1934) Sur la détermination des polynômes d'approximation de degré donnée. *Communications of Kharkov Mathematical Society*, **10**, 41.

[21] Remez, E. (1957) General Computation Methods of Chebyshev Approximation. The Problems with Linear Real Parameters. Publishing House of the Academy of Science of the Ukrainian SSR, Kiev.

[22] Planck Collaboration, Aghanim, N., Akrami, Y., *et al.* (2018) Planck 2018 Results. VI. Cosmological Parameters.

International Journal of Astronomy and Astrophysics, 2019, 9, 63-70
http://www.scirp.org/journal/ijaa
ISSN Online: 2161-4725
ISSN Print: 2161-4717

A Phenomenological Extension of the Newtonian Gravity

Heinz Dehnen

Fachbereich Physik, Universität Konstanz, Konstanz, Germany
Email: heinz.dehnen@uni-konstanz.de

How to cite this paper: Dehnen, H. (2019) A Phenomenological Extension of the Newtonian Gravity. *International Journal of Astronomy and Astrophysics*, **9**, 63-70.
https://doi.org/10.4236/ijaa.2019.91006

Received: January 25, 2019
Accepted: March 16, 2019
Published: March 19, 2019

Abstract

Following the idea of our previous paper we distinguish also in the case of Newtonian gravity as in the electrodynamics between extensive and intensive field quantities. Between both, a "material" quantity produced e.g. by vacuum polarisations induced by the gravitational field strength itself is mediated. It acts in such a way that it amplifies the field strength in weak gravitational fields and reduces the field strength in strong gravitational fields following Lenz's rule. Newton's gravity is valid only in a very large intermediate range of middle field strength $\boldsymbol{F}$ ($|\boldsymbol{F}_0| \ll |\boldsymbol{F}| \ll |\boldsymbol{F}_1|$), $\boldsymbol{F}_0$ and $\boldsymbol{F}_1$ critical field strengths. In this way dark matter and black holes may be avoidable.

Keywords

Flat Rotation Curves, MOND, Tully-Fisher Law, Avoiding Singularities, Vacuum-Polarisations, Lenz's Rule

1. Introduction

In a previous paper [1] we have proposed in view of the dark matter problem a modification of the Newtonian gravity theory in such a way that the assumption of the existence of dark matter is not necessary. In detail we have given a theoretical explanation of MOND [2] following the structure of the electrodynamics assuming also in the case of Newtonian gravity a difference between intensive and extensive field quantities. The intensive field quantity described by F_i obeys the homogeneous field equation[1]

$$F_{i|j} - F_{j|i} = 0 \Rightarrow F_i = -\phi_{|i}, \tag{1}$$

where ϕ is the gravitational potential; simultaneously F_i determines the

[1]We use the tensor calculus including the sum convention and restrict ourselves to Cartesian coordinates for simplicity; $|i$ means the partial derivative $\frac{\partial}{\partial x_i}$.

gravitational force on a massive point particle (mass m) at the position $x_i(t)$ according to ($\cdot = \frac{\mathrm{d}}{\mathrm{d}t}$)

$$\ddot{x}_i = F_i \tag{2}$$

using the weak equivalence principle. Thus F_i is the field strength. In consequence of (1) and (2) energy conservation is guaranteed for $\phi_{|t} \equiv 0$. On the other hand there exists the extensive field quantity G_i determined by the mass density ρ of the matter distribution according to the inhomogeneous field equation

$$G_{i|i} = -4\pi G\rho \tag{3}$$

(G Newtonian gravitational constant). Accordingly G_i is the field excitation, because it is determined by the excitation Equation (3). Between both quantities the "material" equation is mediated:

$$F_i = \gamma G_i, \tag{4}$$

with the "material" quantity γ, which may depend on the field strength itself in consequence e.g. of induced vacuum polarisations. In our previous paper we have assumed

$$\gamma = \frac{|\boldsymbol{F}_0|}{|\boldsymbol{F}|} + 1, \tag{5}$$

where $|\boldsymbol{F}_0|$ is a critical field strength, under which the value of γ increases drastically, so that the field strength $|\boldsymbol{F}|$ increases compared with the Newtonian case ($\gamma = 1$), and the assumption of dark matter will be superfluous.

In the present paper we show that the ansatz (5) can be enlarged in a very simple way in such a direction that the field strength F_i can also not be larger than a critical field strength $|\boldsymbol{F}_1|$ also in consequence of vacuum polarisations so that singularities (e. g. black holes) may be avoided. Doing this we enlarge relation (5) to

$$\gamma = \frac{|\boldsymbol{F}_0|}{|\boldsymbol{F}|} + \sqrt{1 - \left(\frac{|\boldsymbol{F}|}{|\boldsymbol{F}_1|}\right)^2} \quad \text{with } |\boldsymbol{F}_1| \gg |\boldsymbol{F}_0|. \tag{6}$$

This procedure corresponds exactly to the idea of Born and Infeld in the electrodynamics [3] avoiding there electromagnetic field strengths larger than a critical value. Similar impressive influences of vacuum polarisations and fluctuations on the classical physics are e.g. the Casimir effect [4] and the Scharnhorst-Barton effect [5].

According to our proposal (6) we assume that the gravitational field strength will be weakened by increasing field-strength and enforced by decreasing field-strength in consequence e.g. of vacuum polarisations induced by the gravitational field-strength itself following Lenz's rule. Herewith Lenz's fundamental rule is implemented in the whole range of field strengths.[2] The Newtonian grav-

[1]Usually Lenz's rule is connected with time-variable electromagnetic fields. But it has a deeper meaning for all physical systems. If induced quantities, induced by time-variations or variable field strengths in space, would reinforce the original cause, the system would be unstable. Thus Lenz's rule is rather a general stability law.

ity is valid in the very large intermediate range $|\boldsymbol{F}_0| \ll |\boldsymbol{F}| \ll |\boldsymbol{F}_1|$ where $\gamma \simeq 1$ is valid and where also the Newtonian gravitational constant G is determined.[3] The value of $|\boldsymbol{F}_0|$ amounts to 2×10^{-8} cm/sec^2 in view of the flat rotation curves of the spiral galaxies (see discussions in [1] and footnote 5), whereas the value of $|\boldsymbol{F}_1|$ may be of the order of 10^{30} cm/sec^2, where the vacuum will be unstable e.g. with respect to spontaneous particle-antiparticle generations.[4] Of course an exact theoretical derivation of the ansatz (6) does not exist until now because a quantum theory of gravity is missing. In a quantum theory of gravity vacuum polarisation effects would be included, so that a relation like (6), comparable with the running coupling constant in the non-Abelian QCD, would be expectable in the classical limit. In the electromagnetic case Heisenberg and Euler could show that the Born-Infeld ansatz follows from the quantum electrodynamics [6]. In the same sense we consider also our proposal as a phenomenological extension of gravity taking into account expectable quantum effects on the classical level.

2. The Integration Procedure

For solving the equation of motion (2) for a point-like test particle the knowledge of the field strength $\boldsymbol{F}$ is necessary. For this we find from the field Equation (1) and Equation (3) with the use of (4) for the potential ϕ the differential equation:

$$\phi_{|i|i} - \frac{\gamma_{|i}}{\gamma}\phi_{|i} = 4\pi G\rho\gamma. \tag{7}$$

Herein γ is given by (see (6))

$$\gamma = \frac{|\boldsymbol{F}_0|}{\sqrt{\phi_{|j}\phi_{|j}}} + \sqrt{1 - \frac{\phi_{|j}\phi_{|j}}{|\boldsymbol{F}_1|^2}}. \tag{8}$$

Now we restrict ourselves for simplicity to the centrally symmetric case of a mass-sphere of mass M with constant density ρ and radius R and consider at first the area outside the sphere, *i.e.* $r > R$. Than the field Equation (7) reads ($' = \frac{\partial}{\partial r}$):

$$\phi'' + \frac{2}{r}\phi' = \frac{\gamma'}{\gamma}\phi' \tag{9}$$

with the first integral:

$$\phi' r^2 = A\gamma, \quad A = \text{const.} \tag{10}$$

(A integration constant). With

$$\gamma = \frac{|\boldsymbol{F}_0|}{\phi'} + \sqrt{1 - \frac{\phi'^2}{|\boldsymbol{F}_1|^2}} \tag{11}$$

according to (8) we obtain from (10) the following quadratic equation for ϕ'^2:

[3]General Relativity would be also valid only in this intermediate range.

[4]By this acceleration an electron reaches approximately a distance of a Compton wave length during a Compton time necessary for spontaneous electron-positron pair creation.

$$\left(\phi'^2 r^2 - |\boldsymbol{F}_0| A\right)^2 = A^2 \phi'^2 \left(1 - \frac{\phi'^2}{|\boldsymbol{F}_1|^2}\right) \tag{12}$$

with the solution:

$$\phi'^2 = \frac{1}{2}\frac{A^2 + 2|\boldsymbol{F}_0| A r^2}{r^4 + A^2/|\boldsymbol{F}_1|^2} + \sqrt{\frac{1}{4}\left(\frac{A^2 + 2|\boldsymbol{F}_0| A r^2}{r^4 + A^2/|\boldsymbol{F}_1|^2}\right)^2 - \frac{A^2 |\boldsymbol{F}_0|^2}{r^4 + A^2/|\boldsymbol{F}_1|^2}}. \tag{13}$$

For $r \to \infty$ we obtain

$$\phi' = \sqrt{A|\boldsymbol{F}_0|}\frac{1}{r}, \tag{14}$$

so that the flat rotation curves of the spiral galaxies are guaranteed with the constant orbital velocity $v(r \to \infty) = \left(A|\boldsymbol{F}_0|\right)^{1/4}$.[5] This is in accordance with our previous paper and confirms also the Tully-Fisher law [7]. The exact value of the constant A can be only determined by the connection of the solution (13) with the inner one for $r < R$, see Equation (28).

Thus we consider now the case $r < R$. With the abbreviation

$$C = 4\pi G\rho \tag{15}$$

we obtain from (7) the differential equation

$$\phi_{|i|i} - \frac{\gamma_{|i}}{\gamma}\phi_{|i} - C\gamma = 0, \tag{16}$$

which goes over in the centrally symmetric case into:

$$\left(\frac{\phi'}{\gamma}\right)' + \frac{2}{r}\frac{\phi'}{\gamma} = C. \tag{17}$$

We solve this inhomogeneous differential equation by the method of the variation of the constants. The solution of the homogeneous equation belonging to (17) is already known and given by (10) as

$$\phi' = \frac{\tilde{A}\gamma}{r^2}, \tag{18}$$

where $\tilde{A}$ is now the integration constant, which is to vary for solving (17). This gives the differential equation for $\tilde{A}$

$$\tilde{A}' = Cr^2 \tag{19}$$

with the solution

$$\tilde{A} = \frac{1}{3}Cr^3 + B \tag{20}$$

(B new integration constant), so that Equation (18) goes over into:

$$\phi' = \left(\frac{1}{3}Cr^3 + B\right)\frac{\gamma}{r^2}, \tag{21}$$

where γ is finally given by (11). Herewith we obtain once more a quadratic equation for ϕ'^2 with the solution:

[5]Herewith the value $|\boldsymbol{F}_0|$ can be estimated, c.f. (28) and [1].

$$\phi'^2 = \frac{1}{2}\frac{\left(\frac{1}{3}Cr^3+B\right)\left(2|\boldsymbol{F}_0|r^2+\frac{1}{3}Cr^3+B\right)}{r^4+\left(\frac{1}{3}Cr^3+B\right)^2\Big/|\boldsymbol{F}_1|^2} + \left[\frac{1}{4}\frac{\left(\frac{1}{3}Cr^3+B\right)^2\left(2|\boldsymbol{F}_0|r^2+\frac{1}{3}Cr^3+B\right)^2}{\left(r^4+\left(\frac{1}{3}Cr^3+B\right)^2\Big/|\boldsymbol{F}_1|^2\right)^2} - \frac{|\boldsymbol{F}_0|^2\left(\frac{1}{3}Cr^3+B\right)^2}{r^4+\left(\frac{1}{3}Cr^3+B\right)^2\Big/|\boldsymbol{F}_1|^2}\right]^{1/2}. \quad (22)$$

Setting $C=0$ we obtain the solution (13), where B plays the role of A. Accordingly B has the meaning of

$$B = M_0 G, \quad (23)$$

where M_0 is the mass value of an additional central point mass (see Equation (28)). For $r\to 0$ one gets for the case $B\neq 0$

$$\phi'^2(r\to 0) = \frac{1}{2}|\boldsymbol{F}_1|^2\left[1+\sqrt{1-4|\boldsymbol{F}_0|^2/|\boldsymbol{F}_1|^2}\right]. \quad (24)$$

Obviously this is the solution for an additional point mass at $r=0$, where the field-strength possesses no singularity but reaches its maximum possible value $|\boldsymbol{F}_1|$ for $|\boldsymbol{F}_0|/|\boldsymbol{F}_1|\ll 1$ independently of the mass value M_0. Therefore also the existence of black holes should be avoidable.

Avoiding in the following this central point mass we have to set $B=0$. Herewith it follows from (22):

$$\phi'^2 = \frac{1}{2}\frac{\frac{1}{3}Cr^3\left(2|\boldsymbol{F}_0|r^2+\frac{1}{3}Cr^3\right)}{r^4+\left(\frac{1}{3}Cr^3\right)^2\Big/|\boldsymbol{F}_1|^2} + \left[\frac{1}{4}\frac{\left(\frac{1}{3}Cr^3\right)^2\left(2|\boldsymbol{F}_0|r^2+\frac{1}{3}Cr^3\right)^2}{\left(r^4+\left(\frac{1}{3}Cr^3\right)^2\Big/|\boldsymbol{F}_1|^2\right)^2} - \frac{\left(\frac{1}{3}Cr^3|\boldsymbol{F}_0|\right)^2}{r^4+\left(\frac{1}{3}Cr^3\right)^2\Big/|\boldsymbol{F}_1|^2}\right]^{1/2}. \quad (25)$$

Now we obtain for $r\to 0$ after inserting of C according to (15) ($M=\frac{4\pi}{3}\rho R^3$)

$$\phi'(r\to 0) = \left(\frac{MG}{R^3}|\boldsymbol{F}_0|\right)^{1/2}\sqrt{r}, \quad (26)$$

which means that the orbital velocity v has the value

$$v(r\to 0) = \left(MG|\boldsymbol{F}_0|\right)^{1/4}\left(\frac{r}{R}\right)^{3/4}. \quad (27)$$

This is greater than the Newtonian one by the factor $\left(\frac{|\boldsymbol{F}_0|R^3}{MGr}\right)^{1/4}$. Therefore

the high star velocities near the center of the galaxy should be discussed newly avoiding the assumption of a black hole in the galaxy center.

Finally we have to determine the meaning of the integration constant A in the solution (13). It follows from the condition, that the solution (25) for $r < R$ goes steadily over into the solution (13) for $r > R$ at $r = R$. On this way one finds immediately

$$A = MG. \tag{28}$$

Now we can give the complete solution for the massive sphere of radius R and mass M. It is valid for $r \le R$ (see (25)):

$$\phi'^2 = \frac{1}{2}\frac{MG\frac{r}{R^3}\left(MG\frac{r}{R^3}+2|\boldsymbol{F}_0|\right)}{1+\left(MG\frac{r}{R^3}\Big/|\boldsymbol{F}_1|\right)^2} + \left[\frac{1}{4}\frac{\left(MG\frac{r}{R^3}\right)^2\left(MG\frac{r}{R^3}+2|\boldsymbol{F}_0|\right)^2}{\left(1+\left(MG\frac{r}{R^3}\Big/|\boldsymbol{F}_1|\right)^2\right)^2} - \frac{\left(MG\frac{r}{R^3}|\boldsymbol{F}_0|\right)^2}{1+\left(MG\frac{r}{R^3}\Big/|\boldsymbol{F}_1|\right)^2}\right]^{1/2}, \tag{29}$$

and for $r \ge R$ (see (13)):

$$\phi'^2 = \frac{1}{2}\frac{\frac{MG}{r^2}\left(\frac{MG}{r^2}+2|\boldsymbol{F}_0|\right)}{1+\left(\frac{MG}{r^2}\Big/|\boldsymbol{F}_1|\right)^2} + \left[\frac{1}{4}\left(\frac{\frac{MG}{r^2}\left(\frac{MG}{r^2}+2|\boldsymbol{F}_0|\right)}{1+\left(\frac{MG}{r^2}\Big/|\boldsymbol{F}_1|\right)^2}\right)^2 - \frac{\left(\frac{MG}{r^2}|\boldsymbol{F}_0|\right)^2}{1+\left(\frac{MG}{r^2}\Big/|\boldsymbol{F}_1|\right)^2}\right]^{1/2}. \tag{30}$$

The square root of (29) and (30) is given by (32) and (33). In the case of $R \to 0$ the solution (29) results in the finite value (compare (24))

$$\phi'^2 = |\boldsymbol{F}_1|^2 \quad \text{for } |\boldsymbol{F}_0|/|\boldsymbol{F}_1| \ll 1, \tag{31}$$

so that black holes may be avoided, although the field strength is very high. But for confirming this consequence finally a general relativistic investigation of the situation may be necessary.

3. Alternative Solution of the Centrally Symmetric Case

Considering the Equation (4) and Equation (6) one can solve these with respect to F_i in the centrally symmetric case, *i.e.* with respect to ϕ'. After that one can insert for $\boldsymbol{G}$ the Newtonian expression $|\boldsymbol{F}_N|$ according to (3). In the centrally symmetric case the condition (1) is fulfilled as one can test easily. In this way one finds:

$$\phi' = \sqrt{\frac{1}{2}}\left[\left\{\frac{1}{2}\frac{|\boldsymbol{F}_N|\left(|\boldsymbol{F}_N|+2|\boldsymbol{F}_0|\right)}{1+\left(|\boldsymbol{F}_N|/|\boldsymbol{F}_1|\right)^2}+\frac{|\boldsymbol{F}_N||\boldsymbol{F}_0|}{\sqrt{1+\left(|\boldsymbol{F}_N|/|\boldsymbol{F}_1|\right)^2}}\right\}^{1/2}\right.$$
$$\left.+\left\{\frac{1}{2}\frac{|\boldsymbol{F}_N|\left(|\boldsymbol{F}_N|+2|\boldsymbol{F}_0|\right)}{1+\left(|\boldsymbol{F}_N|/|\boldsymbol{F}_1|\right)^2}-\frac{|\boldsymbol{F}_N||\boldsymbol{F}_0|}{\sqrt{1+\left(|\boldsymbol{F}_N|/|\boldsymbol{F}_1|\right)^2}}\right\}^{1/2}\right]. \tag{32}$$

For the mass-sphere with constant mass density ρ and radius R one has to insert

$$\text{for } r<R: \quad |\boldsymbol{F}_N| = \frac{MG}{R^3}r \quad \text{and} \quad \text{for } r>R: \quad |\boldsymbol{F}_N| = \frac{MG}{r^2}. \tag{33}$$

Squaring of (32) results into (29) and (30).

We mention however explicitly that this procedure is in general only applicable in the centrally symmetric case because of the condition (1) and in the case, where the mass density distribution ρ is not determined by the gravitational field strength F_i itself. For the latter case, where ρ is determined e.g. by the Euler equation

$$\rho\left(v_{i|t}+v_{i|k}v_k\right) = \rho F_i - p_{|i} \tag{34}$$

($p(\rho)$ pressure of the substratum) as e.g. in stars and galaxies or polytropic gas spheres the procedure of chapt. 2 is to be used.

4. Conclusion

Considering induced vacuum polarisations we could show in the framework of Newtonian gravity, that the assumption of dark matter and the existence of gravitational field singularities can be avoided. However our proposal discussed in this paper should be translated finally into a general relativistic form. This is not possible in an immediate way, because in the general theory of relativity the distinction between extensive and intensive field quantities is impossible. Therefore the modification of the theory has to start from the very beginning by a modification of the Lagrangian in the form of a $f(R)$-theory [8] as it is done also in the Born-Infeld electrodynamics. This will be our further aim.

Conflicts of Interest

The author declares no conflicts of interest regarding the publication of this paper.

References

[1] Dehnen, H. (2018) Newtonian Gravity Reformulated. *IJTP,* **57**, 1404.

[2] Milgrom, M. (1994) Dynamics with a Nonstandard Inertia-Acceleration Relation: An Alternative to Dark Matter in Galactic Systems. *Annals of Physics,* **229**, 384-415. https://doi.org/10.1006/aphy.1994.1012
Bekenstein, J.D. (2006) The Modified Newtonian Dynamics—MOND and Its Implications for New Physics. *Contemporary Physics,* **47**, 387-483.

https://doi.org/10.1080/00107510701244055

[3] Born, M. and Infeld, L. (1934) Foundations of the New Field Theory. *Proceedings of the Royal Society A*, **144**, 425. https://doi.org/10.1098/rspa.1934.0059

[4] Casimir, H. (1948) On the Attraction between two Perfectly Conducting Plates. *Proceedings van de Koninklijke Nederlandse Akademie van Wetenschappen*, **B51**, 793.

[5] Scharnhorst, K. and Barton, G. (1993) QED between Parallel Mirrors: Light Signals Faster Than c, or Amplified by the Vacuum. *Journal of Physics A,* **26**, 2037. https://doi.org/10.1088/0305-4470/26/8/024

[6] Heisenberg, W. and Euler, H. (1936) Folgerungen aus der Diracschen Theorie des Positrons. *Zeitschrift für Physik,* **98**, 714-732. https://doi.org/10.1007/BF01343663

[7] Tully, R.B. and Fisher, J.R. (1977) A new Method of Determining Distances to Galaxies *Astronomy & Astrophysics*, **54**, 661.

[8] Buchdahl, H.A. (1970) Non-Linear Lagrangians and Cosmological Theory. *Monthly Notices of the Royal Astronomical Society,* **150**, 1-8. https://doi.org/10.1093/mnras/150.1.1

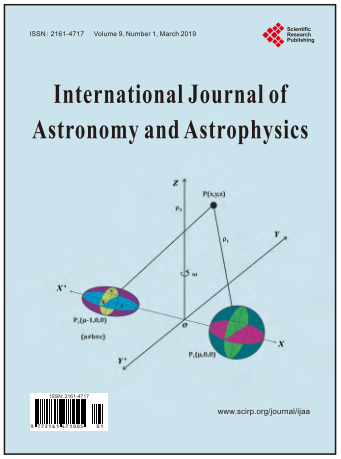

Call for Papers

International Journal of Astronomy and Astrophysics (IJAA)

ISSN 2161-4717 (Print) ISSN 2161-4725 (Online)
http://www.scirp.org/journal/ijaa

International Journal of Astronomy and Astrophysics **(IJAA)** is an international scientific journal dedicated to the publication and public discussion of high quality original research in all the fields of astrophysics and space sciences and related technology. All the manuscripts must be prepared in English, and are subject to a rigorous and fair peer-review process. Accepted papers will immediately appear online followed by printed hard copies.

Editor-in-Chief

Prof. Michael D. Smith University of Kent, UK

Editorial Board

Subject Coverage

The journal publishes original papers including but not limited to the following fields:

- Astrogeodynamics
- Astrophysics
- Cosmic Rays and Gamma Astronomy
- Dynamics of Celestial Bodies in the Solar System and Artificial Bodies
- Extrasolar Planets
- Formation and Evolution of Galaxies and Their Clusters
- Formation and Evolution of Stars
- Heliospheric Physics
- High-Energy and Cataclysmic Processes in Astrophysics
- Interstellar Matter
- Interstellar Medium: Star Formation Regions
- Kinematics and Structure of the Galaxy
- Large-Scale Structure of Universe Formation and Evolution of Galaxies
- Last Stages of Stellar Evolution and Chemical Evolution of the Galaxy
- Magnetospheric Physics
- Microquasars and High-Energy Astrophysics
- Neutron Astronomy
- New Astronomical Techniques and Methods
- Planets, Comets, Asteroids and Dust
- Pulsar Magnetospheres
- Solar and Stellar Physics
- Solar Magnetic Activity and Heliogeospace Environments
- Solar/Interstellar Terrestrial Relations
- Solar-Terrestrial Physics and Space Weather
- Space Observation and Exploration
- Supernovae and Evolution of the Universe

We are also interested in short papers (letters) that clearly address a specific problem, and short survey or position papers that sketch the results or problems on a specific topic. Authors of selected short papers would be invited to write a regular paper on the same topic for future issues of the IJAA.

Notes for Intending Authors

Submitted papers should not have been previously published nor be currently under consideration for publication elsewhere. Paper submission will be handled electronically through the website. All papers are refereed through a peer review process. For more details about the submissions, please access the website.

http://www.scirp.org/journal/ijaa **E-mail: ijaa@scirp.org**

What is SCIRP?

Scientific Research Publishing (SCIRP) is one of the largest Open Access journal publishers. It is currently publishing more than 200 open access, online, peer-reviewed journals covering a wide range of academic disciplines. SCIRP serves the worldwide academic communities and contributes to the progress and application of science with its publication.

What is Open Access?

All original research papers published by SCIRP are made freely and permanently accessible online immediately upon publication. To be able to provide open access journals, SCIRP defrays operation costs from authors and subscription charges only for its printed version. Open access publishing allows an immediate, worldwide, barrier-free, open access to the full text of research papers, which is in the best interests of the scientific community.

- High visibility for maximum global exposure with open access publishing model
- Rigorous peer review of research papers
- Prompt faster publication with less cost
- Guaranteed targeted, multidisciplinary audience

Scientific Research Publishing

Website: http://www.scirp.org

Subscription: sub@scirp.org

Advertisement: service@scirp.org